

1 A search for sparticles in zero lepton final states

2 Russell W. Smith

3 Submitted in partial fulfillment of the

4 requirements for the degree of

5 Doctor of Philosophy

6 in the Graduate School of Arts and Sciences

7 COLUMBIA UNIVERSITY

8 2016

9

© 2016

10

Russell W. Smith

11

All rights reserved

12

ABSTRACT

13

A search for sparticles in zero lepton final states

14

Russell W. Smith

15 TODO : Here's where your abstract will eventually go. The above text is all in the
16 center, but the abstract itself should be written as a regular paragraph on the page,
17 and it should not have indentation. Just replace this text.

Contents

19	Contents	i
20	1 Introduction	1
21	2 The Standard Model	5
22	2.1 Overview	5
23	2.2 Field Content	5
24	2.3 Deficiencies of the Standard Model	15
25	3 Supersymmetry	21
26	3.1 Supersymmetric theories : from space to superspace	21
27	3.2 Minimally Supersymmetric Standard Model	24
28	3.3 Phenomenology	30
29	3.4 How SUSY solves the problems with the SM	33
30	3.5 Conclusions	35
31	4 The Large Hadron Collider	37
32	4.1 Basics of Accelerator Physics	37
33	4.2 Accelerator Complex	39
34	4.3 Large Hadron Collider	41
35	4.4 Dataset Delivered by the LHC	43
36	5 The ATLAS detector	49

37	5.1	Magnets	50
38	5.2	Inner Detector	52
39	5.3	Calorimetry	56
40	5.4	Muon Spectrometer	61
41	5.5	Trigger System	66
42	6	Event Reconstruction	73
43	6.1	Primitive Object Reconstruction	73
44	6.2	Physics Object Reconstruction and Quality Identification	79
45	6.3	Maybe PFlow?	86
46	7	The Recursive Jigsaw Technique	87
47	7.1	Razor variables	87
48	7.2	SuperRazor variables	87
49	7.3	The Recursive Jigsaw Technique	87
50	7.4	Variables used in the search for zero lepton SUSY	87
51	8	Table of Contents Title	89
52	9	A search for supersymmetric particles in zero lepton final states with the Recursive Jigsaw Technique	91
54	9.1	Object reconstruction	91
55	9.2	Signal regions	92
56	9.3	Background estimation	92
57	10	Results	93
58	10.1	Statistical Analysis	93
59	10.2	Signal Region distributions	93
60	10.3	Pull Plots	93
61	10.4	Systematic Uncertainties	93

62	10.5 Exclusion plots	93
63	Conclusion	95
64	10.6 New Section	95
65	Bibliography	97
66	Quantum Field Theory and Symmetries	107
67	Quantum Field Theory	107
68	Symmetries	108
69	Local symmetries	110

Acknowledgements

Dedication

Introduction

74 Particle physics is a remarkably successful field of scientific inquiry. The ability to
 75 precisely predict the properties of a exceedingly wide range of physical phenomena,
 76 such as the description of the cosmic microwave background [1, 2], the understanding
 77 of the anomalous magnetic dipole moment of the electron [3, 4], and the measurement
 78 of the number of weakly-interacting neutrino flavors [5] is truly amazing.

79 The theory that has allowed this range of predictions is the *Standard Model*
 80 of particle physics (SM). The Standard Model combines the electroweak theory of
 81 Glashow, Weinberg, and Salam [6–8] with the theory of the strong interactions, as
 82 first envisioned by Gell-Mann and Zweig [9, 10]. This quantum field theory (QFT)
 83 contains a tiny number of particles, whose interactions describe phenomena up to at
 84 least the TeV scale. These particles are manifestations of the fields of the Standard
 85 Model, after application of the Higgs Mechanism. The particle content of the SM
 86 consists only of the six quarks, the six leptons, the four gauge bosons, and the scalar
 87 Higgs boson.

88 Despite its impressive range of described phenomena, the Standard Model has
 89 some theoretical and experimental deficiencies. The SM contains 26 free parameters
 90 ¹. It would be more theoretically pleasing to understand these free parameters in
 91 terms of a more fundamental theory. The major theoretical concern of the Standard
 92 Model, as it pertains to this thesis, is the *hierarchy problem*[11–15]. The light mass

¹This is the Standard Model corrected to include neutrino masses. These parameters are the fermion masses (6 leptons, 6 quarks), CKM and PMNS mixing angles (8 angles, 2 CP-violating phases), W/Z/Higgs masses (3), the Higgs field expectation value, and the couplings of the strong, weak, and electromagnetic forces (3 α_{force}).

of the Higgs boson (125 GeV) should be quadratically dependent on the scale of UV physics, due to the quantum corrections from high-energy physics processes. The most perplexing experimental issue is the existence of *dark matter*, as demonstrated by galactic rotation curves [16–22]. This data has shown that there exists additional matter which has not yet been seen interacting with the particles of the Standard Model. There is no particle in the SM which can act as a candidate for dark matter.

Both of these major issues, as well as numerous others, can be solved by the introduction of *supersymmetry* (SUSY) [15, 23–35]. In supersymmetric theories, each SM particles has a so-called *superpartner*, or sparticle partner, differing from given SM particle by 1/2 in spin. These theories solve the hierarchy problem, since the quantum corrections induced from the superpartners exactly cancel those induced by the SM particles. In addition, these theories are usually constructed assuming *R*–parity, which can be thought of as the “charge” of supersymmetry, with SM particles having $R = 1$ and sparticles having $R = -1$. In collider experiments, since the incoming SM particles have total $R = 1$, the resulting sparticles are produced in pairs. This produces a rich phenomenology, which is characterized by significant hadronic activity and large missing transverse energy (E_T^{miss}), which provide significant discrimination against SM backgrounds [36].

Despite the power of searches for supersymmetry where E_T^{miss} is a primary discriminating variable, there has been significant interest in the use of other variables to discriminate against SM backgrounds. These include searches employing variables such as αT , $M_{T,2}$, and the razor variables (M_R, R^2) [37–47]. In this thesis, we will present the first search for supersymmetry using the novel Recursive Jigsaw Reconstruction (RJR) technique. RJR can be considered the conceptual successor of the razor variables. We impose a particular final state “decay tree” on an events, which roughly corresponds to a simplified Feynmann diagram in decays containing weakly-interacting particles. We account for the missing degrees of freedom associated

120 to the weakly-interacting particles by a series of simplifying assumptions, which allow
121 us to calculate our variables of interest at each step in the decay tree. This allows an
122 unprecedented understanding of the internal structure of the decay and the ability to
123 construct additional variables to reject Standard Model backgrounds.

124 This thesis details a search for the superpartners of the gluon and quarks, the
125 gluino and squarks, in final states with zero leptons, with 13.3 fb^{-1} of data using the
126 ATLAS detector. We organize the thesis as follows. The theoretical foundations of
127 the Standard Model and supersymmetry are described in Chapters 2 and 3. The
128 Large Hadron Collider and the ATLAS detector are presented in Chapters 4 and 5.
129 Chapter 5 provides a detailed description of Recursive Jigsaw Reconstruction and a
130 description of the variables used for the particular search presented in this thesis.
131 Chapter 6 presents the details of the analysis, including details of the dataset, object
132 reconstruction, and selections used. In Chapter 7, the final results are presented;
133 since there is no evidence of a supersymmetric signal in the analysis, we present the
134 final exclusion curves in simplified supersymmetric models.

2.1 Overview

A Standard Model is another name for a theory of the internal symmetry group $SU(3)_C \otimes SU(2)_L \otimes U(1)_Y$, with its associated set of parameters. *The Standard Model* refers specifically to a Standard Model with the proper parameters to describe the universe. The SM is the culmination of years of work in both theoretical and experimental particle physics. In this thesis, we take the view that theorists cite

construct a model with the field content and symmetries as inputs, and write down the most general Lagrangian consistent with those symmetries. Assuming this model is compatible with nature (in particular, the predictions of the model are consistent with previous experiments), experimentalists are responsible measuring the parameters of this model. This will be applicable for this chapter and the following one.

Additional theoretical background is in 10.6. The philosophy and notations are inspired by [48, 49].

2.2 Field Content

The Standard Model field content is

$$\begin{aligned} \text{Fermions} &: Q_L(3, 2)_{+1/3}, U_R(3, 1)_{+4/3}, D_R(3, 1)_{-2/3}, L_L(1, 2)_{-1}, E_R(1, 1)_{-2} \\ \text{Scalar (Higgs)} &: \phi(1, 2)_{+1} \\ \text{Vector Fields} &: G^\mu(8, 1)_0, W^\mu(1, 3)_0, B^\mu(1, 1)_0 \end{aligned} \tag{2.1}$$

151 where the $(A, B)_Y$ notation represents the irreducible representation under $SU(3)$
152 and $SU(2)$, with Y being the electroweak hypercharge. Each of these fermion fields
153 has an additional index, representing the three generation of fermions.

154 We observed that Q_L, U_R , and D_R are triplets under $SU(3)_C$; these are the *quark*
155 fields. The *color* group, $SU(3)_C$ is mediated by the *gluon* field $G^\mu(8, 1)_0$, which has
156 8 degrees of freedom. The fermion fields $L_L(1, 2)_{-1}$ and $E_R(1, 1)_{-2}$ are singlets under
157 $SU(3)_C$; we call them the *lepton* fields.

158 Next, we note the “left-handed” (“right-handed”) fermion fields, denoted by L (R)
159 subscript, The left-handed fields form doublets under $SU(2)_L$. These are mediated
160 by the three degrees of freedom of the “W” fields $W^\mu(1, 3)_0$. These fields only act
161 on the left-handed particles of the Standard Model. This is the reflection of the
162 “chirality” of the Standard Model; the left-handed and right-handed particles are
163 treated differently by the electroweak forces. The right-handed fields, U_R, D_R , and
164 E_R , are singlets under $SU(2)_L$.

165 The $U(1)_Y$ symmetry is associated to the $B^\mu(1, 1)_0$ boson with one degree of
166 freedom. The charge Y is known as the electroweak hypercharge.

167 To better understand the phenomenology of the Standard Model, let us investigate
168 each of the *sectors* of the Standard Model separately.

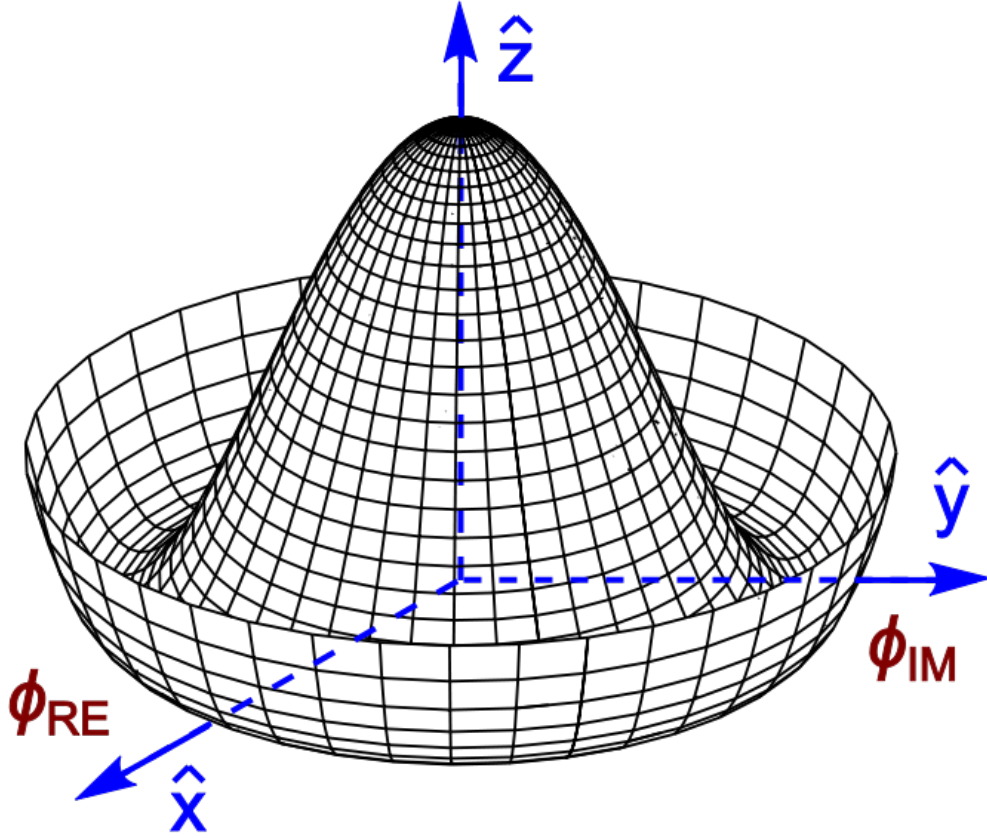
169 Electroweak sector

The electroweak sector refers to the $SU(2)_L \otimes U(1)_Y$ portion of the Standard
Model gauge group. Following our philosophy of writing all gauge-invariant and
renormalizable terms, the electroweak Lagrangian can be written as

$$\mathcal{L} = W_a^{\mu\nu} W_{\mu\nu}^a + B^{\mu\nu} B_{\mu\nu} + (D^\mu \phi)^\dagger D_\mu \phi - \mu^2 \phi^\dagger \phi - \lambda (\phi^\dagger \phi)^2. \quad (2.2)$$

where $W_a^{\mu\nu}$ are the three ($a = 1, 2, 3$) gauge bosons associated to the $SU(2)_L$ gauge
group, $B^{\mu\nu}$ is the one gauge boson of the $U(1)_Y$ gauge group, and ϕ is the complex

Figure 2.1: Sombrero potential



Higgs multiplet. The covariant derivative D^μ is given by

$$D^\mu = \partial^\mu + \frac{ig}{2} W_a^\mu \sigma_a + \frac{ig'}{2} B^\mu \quad (2.3)$$

where $i\sigma_a$ are the Pauli matrices times the imaginary constant, which are the generators for $SU(2)_L$, and g and g' are the $SU(2)_L$ and $U(1)_Y$ coupling constants, respectively. The field strength tensors $W_a^{\mu\nu}$ and $B^{\mu\nu}$ are given by the commutator of the covariant derivative associated to each field

$$B^{\mu\nu} = \partial^\mu B^\nu - \partial^\nu B^\mu \quad (2.4)$$

$$W_a^{\mu\nu} = \partial^\mu W_a^\nu - \partial^\nu W_a^\mu - g\epsilon_{abc} W_a^\mu W_b^\nu, \quad i = 1, 2, 3$$

171 The terms in the Lagrangian 2.2 proportional to μ^2 and λ make up the “Higgs
 172 potential” [50]. As normal (see Appendix 10.6), we restrict $\lambda > 0$ to guarantee our
 173 potential is bounded from below, and we also require $\mu^2 < 0$, which gives us the
 174 standard “sombrero” potential shown in 2.1.

This potential has infinitely many minima at $\langle \phi \rangle = \sqrt{2m/\lambda}$; the ground state is *spontaneously* broken by the choice of ground state, which induces a vacuum expectation value (VEV). Without loss of generality, we can choose the Higgs field ϕ to point in the real direction, and write the Higgs field ϕ in the following form :

$$\phi = \frac{1}{\sqrt{2}} \exp\left(\frac{i}{v} \sigma_a \theta_a\right) \begin{pmatrix} 0 \\ v + h(x) \end{pmatrix}. \quad (2.5)$$

We choose a gauge to rotate away the dependence on θ_a , such that we can write simply

$$\phi = \frac{1}{\sqrt{2}} \begin{pmatrix} 0 \\ v + h(x) \end{pmatrix}. \quad (2.6)$$

Now, we can see how the masses of the vector bosons are generated from the application of the Higgs mechanism. We plug Eq.2.6 back into the electroweak Lagrangian, and only showing the relevant mass terms in the vacuum state where $h(x) = 0$ see that (dropping the Lorentz indices) :

$$\begin{aligned} \mathcal{L}_M &= \frac{1}{8} \left| \begin{pmatrix} gW_3 + g'B & g(W_1 - iW_2) \\ g(W_1 + iW_2) & -gW_3 + g'B \end{pmatrix} \begin{pmatrix} 0 \\ v \end{pmatrix} \right|^2 \\ &= \frac{g^2 v^2}{8} \left[W_1^2 + W_2^2 + \left(\frac{g'}{g} B - W_3 \right)^2 \right] \end{aligned} \quad (2.7)$$

Defining the Weinberg angle $\tan(\theta_W) = g'/g$ and the following *physical* fields :

$$W^\pm = \frac{1}{\sqrt{2}} (W_1 \mp iW_2) \quad (2.8)$$

$$Z^0 = \cos \theta_W W_3 - \sin \theta_W B$$

$$A^0 = \sin \theta_W W_3 + \cos \theta_W B$$

we can write the piece of the Lagrangian associated to the vector boson masses as

$$\mathcal{L}_{MV} = \frac{1}{4}g^2 v^2 W^+ W^- + \frac{1}{8}(g^2 + g'^2)v^2 Z^0 Z^0. \quad (2.9)$$

and we have the following values of the masses for the vector bosons :

$$\begin{aligned} m_W^2 &= \frac{1}{4}v^2 g^2 \\ m_Z^2 &= \frac{1}{4}v^2(g^2 + g'^2) \\ m_A^2 &= 0 \end{aligned} \quad (2.10)$$

We thus see how the Higgs mechanism gives rise to the masses of the W^\pm and Z boson in the Standard Model; the mass of the photon is zero, as expected. The $SU(2)_L \otimes U(1)_Y$ symmetry of the initially massless $W_{1,2,3}$ and B fields is broken to the $U(1)_{EM}$. Of the four degrees of freedom in the complex Higgs doublet, three are “eaten” when we give mass to the W^\pm and Z_0 , while the other degree of freedom is the Higgs particle, as found in 2012 by the ATLAS and CMS collaborations [51, 52].

181 Quantum Chromodynamics

Quantum chromodynamics (or the theory of the *strong* force) characterizes the behavior of *colored* particles, collectively known as *partons*. The partons of the Standard Model are the (fermionic) quarks, and the (bosonic) gluons. The strong force is governed by $SU(3)_C$, an unbroken symmetry in the Standard Model, which implies the gluon remains massless. Defining the covariant derivative for QCD as

$$D^\mu = \partial^\mu + ig_s G_a^\mu L_a, a = 1, \dots, 8 \quad (2.11)$$

where L_a are the generators of $SU(3)_C$, and g_s is the coupling constant of the strong force. The QCD Lagrangian then is given by

$$\mathcal{L}_{QCD} = i\bar{\psi}_f D_\mu \gamma^\mu \psi_f - \frac{1}{4}G_{a,\mu\nu} G_a^{\mu\nu} \quad (2.12)$$

where the summation over f is for quarks *families*, and $G_a^{\mu\nu}$ is the gluon field strength tensor, given by

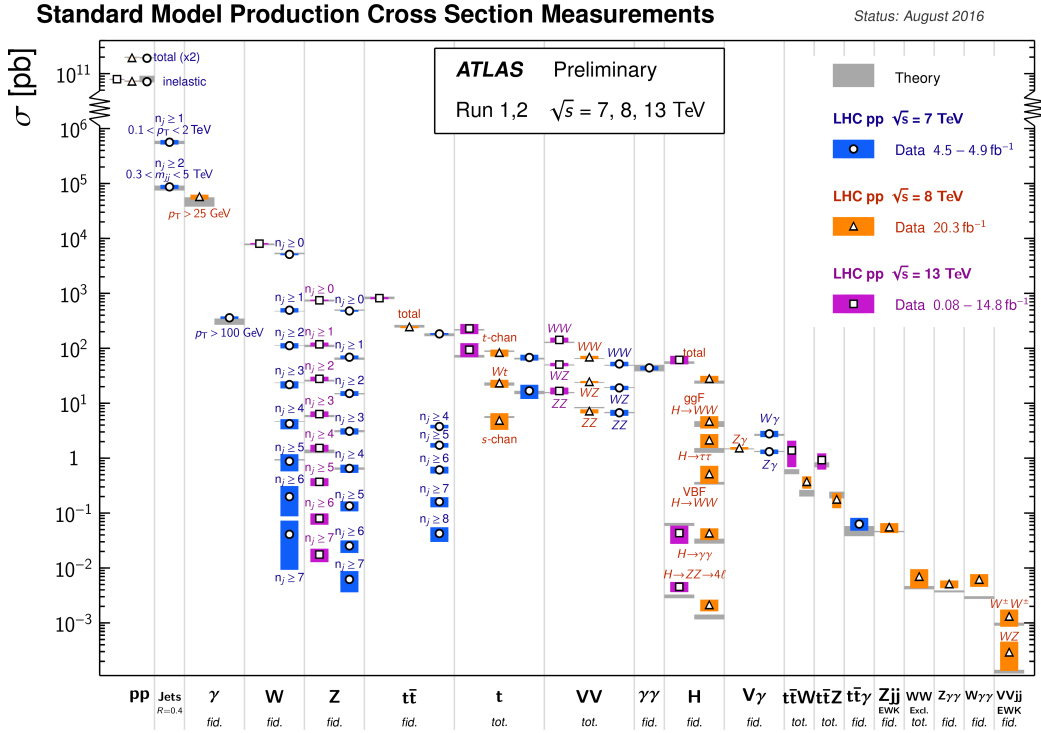
$$G_a^{\mu\nu} = \partial^\mu G_a^\nu - \partial^\nu G_a^\mu - g_s f^{abc} G_b^\mu G_c^\nu, a, b, c = 1, \dots, 8 \quad (2.13)$$

182 where f^{abc} are the structure constants of $SU(3)_C$, which are analogous to ϵ_{abc} for
 183 $SU(2)_L$. The kinetic term for the quarks is contained in the standard ∂_μ term, while
 184 the field strength term contains the interactions between the quarks and gluons, as
 185 well as the gluon self-interactions.

186 Written down in this simple form, the QCD Lagrangian does not seem much
 187 different from the QED Lagrangian, with the proper adjustments for the different
 188 group structures. The gluon is massless, like the photon, so one could naïvely expect
 189 an infinite range force, and it pays to understand why this is not the case. The
 190 reason for this fundamental difference is the gluon self-interactions arising in the
 191 field strength tensor term of the Lagrangian. This leads to the phenomena of *color*
 192 *confinement*, which describes how one only observes color-neutral particles alone in
 193 nature. In contrast to the electromagnetic force, particles which interact via the
 194 strong force experience a *greater* force as the distance between the particles increases.
 195 At long distances, the potential is given by $V(r) = -kr$. At some point, it is more
 196 energetically favorable to create additional partons out of the vacuum than continue
 197 pulling apart the existing partons, and the colored particles undergo *fragmentation*.
 198 This leads to *hadronization*. Bare quarks and gluons are actually observed as sprays
 199 of hadrons (primarily kaons and pions); these sprays are known as *jets*, which are
 200 what are observed by experiments.

201 It is important to recognize the importance of understanding these QCD inter-
 202 actions in high-energy hadron colliders such as the LHC. Since protons are hadrons,
 203 proton-proton collisions such as those produced by the LHC are primarily governed by
 204 the processes of QCD. In particular, by far the most frequent process observed in LHC
 205 experiments is dijet production from gluon-gluon interactions (see Fig.2.2). These

Figure 2.2: Cross-sections of various Standard Model processes



206 gluons that interact are part of the *sea* particles inside the proton; the simple $p = uud$
 207 model does not apply. The main *valence* uud quarks are constantly interacting via
 208 gluons, which can themselves radiate gluons or split into quarks, and so on. A more
 209 useful understanding is given by the colloquially-known *bag* model [53, 54], where the
 210 proton is seen as a “bag” of (in principle) infinitely many partons, each with energy
 211 $E < \sqrt{s} = 6.5$ TeV. One then collides this (proton) bag with another, and views the
 212 products of this very complicated collision, where calculations include many loops in
 213 nonperturbative QCD calculations.

214 Fortunately, we are generally saved by the QCD factorization theorems [55]. This
 215 allows one to understand the hard (i.e. short distance or high energy) $2 \rightarrow 2$ parton
 216 process using the tools of perturbative QCD, while making series of approximations
 217 known as a *parton shower* model to understand the additional corrections from
 218 nonperturbative QCD. We will discuss the reconstruction of jets by experiments in
 219 Ch.5.

220 **Fermions**

221 We will now look more closely at the fermions in the Standard Model [56].

222 As noted earlier in Sec.2.2, the fermions of the Standard Model can be first
 223 distinguished between those that interact via the strong force (quarks) and those
 224 which do not (leptons).

There are six leptons in the Standard Model, which can be placed into three
generations.

$$\begin{pmatrix} e \\ \nu_e \end{pmatrix}, \begin{pmatrix} \mu \\ \nu_\mu \end{pmatrix}, \begin{pmatrix} \tau \\ \nu_\tau \end{pmatrix} \quad (2.14)$$

225 There is the electron (e), muon (μ), and tau (τ), each of which has an associated
 226 neutrino (ν_e, ν_μ, ν_τ). Each of the so-called charged (“electron-like”) leptons has
 227 electromagnetic charge -1 , while the neutrinos all have $q_{EM} = 0$.

228 Often in an experimental context, lepton is used to denote the stable electron
 229 and metastable muon, due to their striking experimental signatures. Taus are often
 230 treated separately, due to their much shorter lifetime of $\tau_\tau \sim 10^{-13}s$; these decay
 231 through hadrons or the other leptons, so often physics analyses at the LHC treat
 232 them as jets or leptons, as will be done in this thesis.

233 As the neutrinos are electrically neutral, nearly massless, and only interact via the
 234 weak force, it is quite difficult to observe them directly. Since LHC experiments rely
 235 overwhelmingly on electromagnetic interactions to observe particles, the presence of
 236 neutrinos is not observed directly. Neutrinos are instead observed by the conservation
 237 of four-momentum in the plane transverse to the proton-proton collisions, known as
 238 *missing transverse energy*.

There are six quarks in the Standard Model : up, down, charm, strange, top, and
 bottom. Quarks are similar organized into three generations :

$$\begin{pmatrix} u \\ d \end{pmatrix}, \begin{pmatrix} c \\ s \end{pmatrix}, \begin{pmatrix} t \\ b \end{pmatrix} \quad (2.15)$$

239 where we speak of “up-like” quarks and “down-like” quarks.

240 Each up-like quark has charge $q_{up} = 2/3$, while the down-like quarks have $q_{down} =$
241 $-1/3$. At the high energies of the LHC, one often makes the distinction between
242 the light quarks (u, d, c, s), the bottom quark, and top quark. In general, due to
243 the hadronization process described above, the light quarks, with masses $m_q < \sim$
244 1.5GeV are indistinguishable by LHC experiments. Their hadronic decay products
245 generally have long lifetimes and they are reconstructed as jets.¹. The bottom quark
246 hadronizes primarily through the B -mesons, which generally travels a short distance
247 before decaying to other hadrons. This allows one to distinguish decays via b -quarks
248 from other jets; this procedure is known as *b-tagging* and will be discussed more in
249 Ch.5. Due to its large mass, the top quark decays before it can hadronize; there
250 are no bound states associated to the top quark. The top is of particular interest at
251 the LHC; it has a striking signature through its most common decay mode $t \rightarrow Wb$.
252 Decays via tops, especially $t\bar{t}$ are frequently an important signal decay mode, or an
253 important background process.

254 **Interactions in the Standard Model**

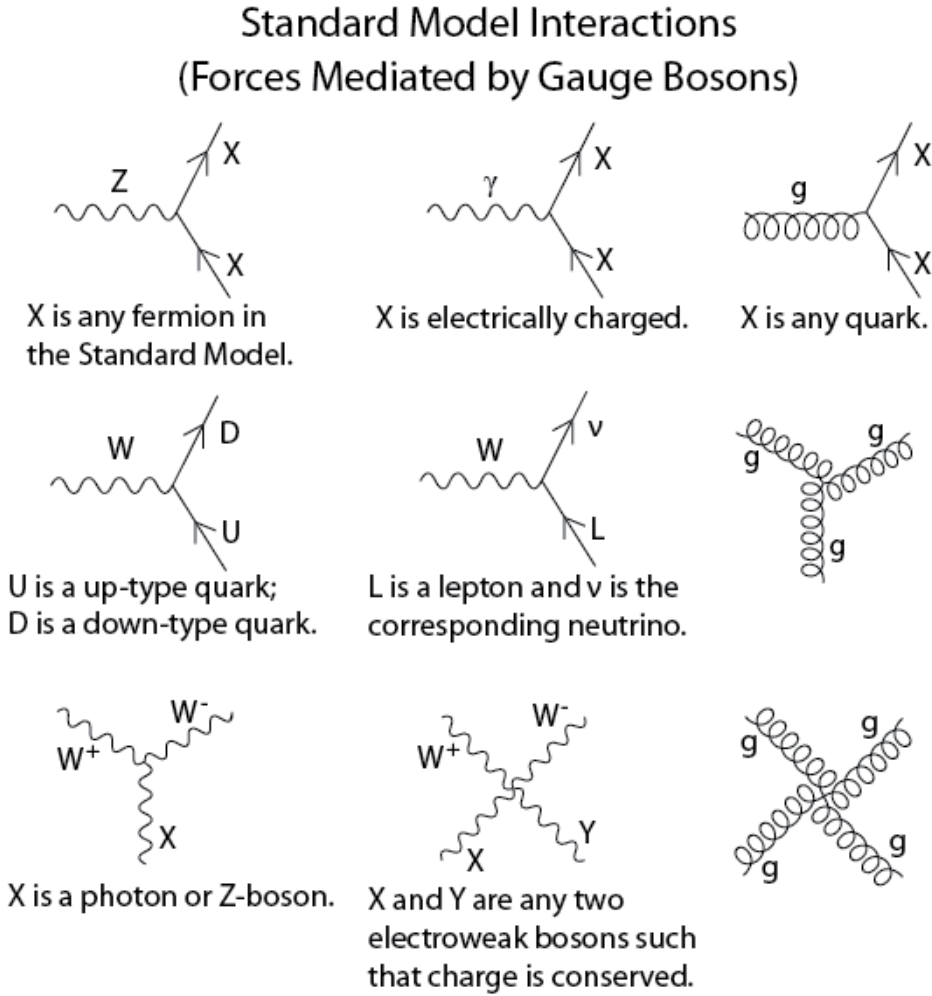
255 We briefly overview the entirety of the fundamental interactions of the Standard
256 Model; these can also be found in 2.3.

257 The electromagnetic force, mediated by the photon, interacts with via a three-
258 point coupling all charged particles in the Standard Model. The photon thus interacts
259 with all the quarks, the charged leptons, and the charged W^\pm bosons.

260 The weak force is mediated by three particles : the W^\pm and the Z^0 . The Z^0 can
261 interacts with all fermions via a three-point coupling. A real Z_0 can thus decay to
262 a fermion-antifermion pair of all SM fermions except the top quark, due to its large

¹In some contexts, charm quarks are also treated as a separate category, although it is quite difficult to distinguish charm quarks from the other light quarks.

Figure 2.3: The interactions of the Standard Model



mass. The W^\pm has two important three-point interactions with fermions. First, the W^\pm can interact with an up-like quark and a down-like quark; an important example in LHC experiments is $t \rightarrow W b$. The coupling constants for these interactions are encoded in the unitary matrix known as the Cabibbo–Kobayashi–Maskawa (CKM) matrix [57, 58], and are generally known as flavor-changing interactions. Secondly, the W^\pm interacts with a charged lepton and its corresponding neutrino. In this case, the unitary matrix that corresponds to CKM matrix for quarks is the identity matrix, which forbids (fundamental) vertices such as $\mu \rightarrow We$. For leptons, instead this is a two-step process : $\mu \rightarrow \nu_m u W \rightarrow \nu_m u \bar{\nu}_e e$. Finally, there are the self-interactions

272 of the weak gauge bosons. There is a three-point and four-point interaction; all
273 combinations are allowed which conserve electric charge.

274 The strong force is mediated by the gluon, which as discussed above also carries
275 the strong color charge. There is the fundamental three-point interaction, where a
276 quark radiates a gluon. Additionally, there are the three-point and four-point gluon-
277 only interactions.

278 2.3 Deficiencies of the Standard Model

279 At this point, it is quite easy to simply rest on our laurels. This relatively simple
280 theory is capable of explaining a very wide range of phenomena, which ultimately
281 break down only to combinations of nine diagrams shown in Fig.2.3. Unfortunately,
282 there are some unexplained problems with the Standard Model. We cannot go
283 through all of the potential issues in this thesis, but we will motivate the primary
284 issues which naturally lead one to *supersymmetry*, as we will see in Ch.3.

The Standard Model has many free parameters; see Table 2.1 In general, we prefer models with less free parameters. A great example of this fact, and the primary experimental evidence for EWSB, is the relationship between the couplings of the weak force and the masses of the gauge bosons of the weak force :

$$\rho \equiv \frac{m_W^2}{m_Z^2 \cos^2 \theta_W} \stackrel{?}{=} 1 \quad (2.16)$$

285 where ? indicates that this is a testable prediction of the Standard Model (in
286 particular, that the gauge bosons gain mass through EWSB). This relationship has
287 been measured within experimental and theoretical predictions. We would like to
288 produce additional such relationships, which would exist if the Standard Model is a
289 low-energy approximation of some other theory.

290 An additional issue is the lack of *gauge coupling unification*. The couplings of
291 any quantum field theory “run” as a function of the distance scales (or inversely,

Table 2.1: Parameters of the Standard Model. For values dependent on the renormalization scheme, we use a combination of the on-shell normalization scheme [59–62] and modified minimal subtraction scheme with $m_{\bar{MS}}$ as indicated in the table[63]

m_e	Electron mass	511 keV
m_μ	Muon mass	105.7 MeV
m_τ	Tau mass	1.78 GeV
m_u	Up quark mass	1.9 MeV ($m_{\bar{MS}} = 2\text{GeV}$)
m_d	Down quark mass	4.4 MeV ($m_{\bar{MS}} = 2\text{GeV}$)
m_s	Strange quark mass	87 MeV ($m_{\bar{MS}} = 2\text{GeV}$)
m_c	Charm quark mass	1.32 GeV ($m_{\bar{MS}} = m_c$)
m_b	Bottom quark mass	4.24 GeV ($m_{\bar{MS}} = m_b$)
m_t	Top quark mass	172.7 GeV (on-shell renormalization)
θ_{12} CKM	12-mixing angle	13.1°
θ_{23} CKM	23-mixing angle	2.4°
θ_{13} CKM	13-mixing angle	0.2°
δ CKM	CP-violating Phase	0.995
g'	U(1) gauge coupling	0.357 ($m_{\bar{MS}} = m_Z$)
g	SU(2) gauge coupling	0.652 ($m_{\bar{MS}} = m_Z$)
g_s	SU(3) gauge coupling	1.221 ($m_{\bar{MS}} = m_Z$)
θ_{QCD}	QCD vacuum angle	~0
VEV	Higgs vacuum expectation value	246 GeV
m_H	Higgs mass	125 GeV

292 energy scales) of the theory. The idea is closely related to the unification of the
 293 electromagnetic and weak forces at the so-called *electroweak scale* of $O(100 \text{ GeV})$.

294 One would hope this behavior was repeated between the electroweak forces and the
 295 strong force at some suitable energy scale. The Standard Model does automatically
 296 not exhibit this behavior, as we can see in Fig.2.4.

The most significant problem with the Standard Model is the *hierarchy problem*. In its most straightforward incarnation, the Higgs scalar field is subject to quantum corrections through loop diagrams, as shown in Fig.2.5. For demonstration, we use the contributions from the top quark, since the top quark has the largest Higgs Yukawa coupling due to its large mass. In general, we should expect these corrections to quadratically depend on the scale of the ultraviolet physics, Λ . Briefly assume there is no new physics before the Planck scale of gravity, $\Lambda_{\text{Planck}} = 10^{19} \text{ GeV}$. In this

Figure 2.4: The running of Standard Model gauge couplings. The Standard Model couplings do not unify at high energies, which indicates it cannot completely describe nature through the Planck scale.

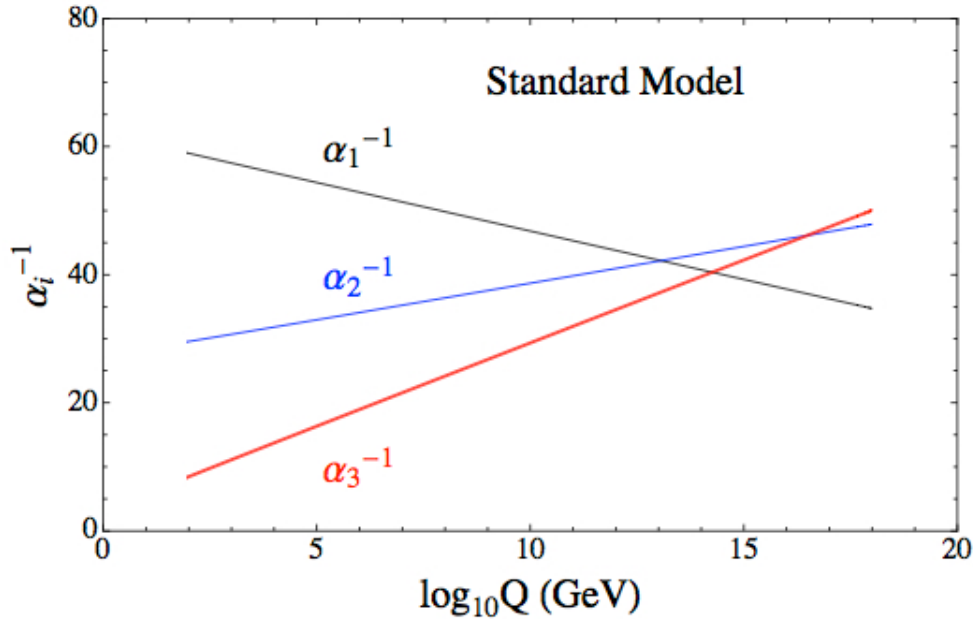
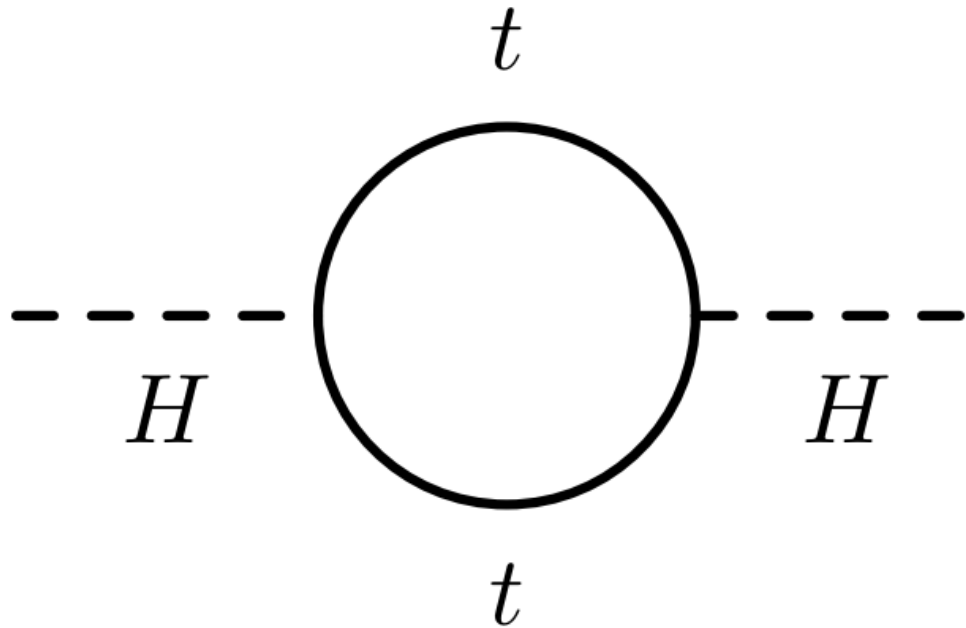


Figure 2.5: The dominant quantum loop correction to the Higgs mass in the Standard Model.



case, we expect the corrections to the Higgs mass like

$$\delta m_H^2 \approx \left(\frac{m_t}{8\pi^2 \langle \phi \rangle_{VEV}} \right)^2 \Lambda_{Planck}^2. \quad (2.17)$$

297 To achieve the miraculous cancellation required to get the observed Higgs mass of
298 125 GeV, one needs to then set the bare Higgs mass m_0 , our input to the Standard
299 Model Lagrangian, itself to a *precise* value $\sim 10^{19}$ GeV. This extraordinary level of
300 parameter finetuning is quite undesirable, and within the framework of the Standard
301 Model, there is little that can be done to alleviate this issue.

302 An additional concern, of a different nature, is the lack of a *dark matter* candidate
303 in the Standard Model. Dark matter was discovered by observing galactic rotation
304 curves, which showed that much of the matter that interacted gravitationally was
305 invisible to our (electromagnetic) telescopes [16–22]. The postulation of the existence
306 of dark matter, which interacts at least through gravity, allows one to understand
307 these galactic rotation curves. Unfortunately, no particle in the Standard Model could
308 possibly be the dark matter particle. The only candidate truly worth another look is
309 the neutrino, but it has been shown that the neutrino content of the universe is simply
310 too small to explain the galactic rotation curves [22, 64]. The experimental evidence
311 from the galactic rotations curves thus show there *must* be additional physics beyond
312 the Standard Model, which is yet to be understood.

313 In the next chapter, we will see how these problems can be alleviated by the theory
314 of supersymmetry.

Figure 2.6: Particles of the Standard Model

mass → $\approx 2.3 \text{ MeV}/c^2$ charge → $2/3$ spin → $1/2$	mass → $\approx 1.275 \text{ GeV}/c^2$ charge → $2/3$ spin → $1/2$	mass → $\approx 173.07 \text{ GeV}/c^2$ charge → $2/3$ spin → $1/2$	mass → 0 charge → 0 spin → 1	mass → $\approx 126 \text{ GeV}/c^2$ charge → 0 spin → 0
QUARKS u up	c charm	t top	g gluon	H Higgs boson
$\approx 4.8 \text{ MeV}/c^2$ $-1/3$ $1/2$ down	$\approx 95 \text{ MeV}/c^2$ $-1/3$ $1/2$ strange	$\approx 4.18 \text{ GeV}/c^2$ $-1/3$ $1/2$ bottom	γ	photon
LEPTONS e electron	μ muon	τ tau	Z Z boson	Gauge Bosons
$<2.2 \text{ eV}/c^2$ 0 $1/2$ electron neutrino	$<0.17 \text{ MeV}/c^2$ 0 $1/2$ muon neutrino	$<15.5 \text{ MeV}/c^2$ 0 $1/2$ tau neutrino	$80.4 \text{ GeV}/c^2$ ± 1 1 W boson	

Supersymmetry

317 This chapter will introduce supersymmetry (SUSY) [15, 23–35]. We will begin by
 318 introducing the concept of a *superspace*, and discuss some general ingredients of
 319 supersymmetric theories. This will include a discussion of how the problems with the
 320 Standard Model described in Ch.2 are naturally fixed by these theories.

321 The next step is to discuss the particle content of the *Minimally Supersymmetric*
 322 *Standard Model* (MSSM). As its name implies, this theory contains the minimal
 323 additional particle content to make Standard Model supersymmetric. We then discuss
 324 the important phenomenological consequences of this theory, especially as it would
 325 be observed in experiments at the LHC.

326 **3.1 Supersymmetric theories : from space to
 327 superspace**

328 **Coleman-Mandula “no-go” theorem**

329 We begin the theoretical motivation for supersymmetry by citing the “no-go” theorem
 330 of Coleman and Mandula [65]. This theorem forbids *spin-charge unification*; it
 331 states that all quantum field theories which contain nontrivial interactions must be
 332 a direct product of the Poincaré group of Lorentz symmetries, the internal product
 333 from of gauge symmetries, and the discrete symmetries of parity, charge conjugation,
 334 and time reversal. The assumptions which go into building the Coleman-Mandula

theorem are quite restrictive, but there is one unique way out, which has become known as *supersymmetry* [26, 66]. In particular, we must introduce a *spinorial* group generator Q . Alternatively, and equivalently, this can be viewed as the addition of anti-commuting coordinates; space plus these new anti-commuting coordinates is then called *superspace* [67]. We will not investiage this view in detail, but it is also a quite intuitive and beautiful way to construct supersymmetry[15].

341 Supersymmetry transformations

342 A *supersymmetric* transformation Q transforms a bosonic state into a fermionic state,
 343 and vice versa :

$$Q |\text{Fermion}\rangle = |\text{Boson}\rangle \quad (3.1)$$

$$Q |\text{Boson}\rangle = |\text{Fermion}\rangle \quad (3.2)$$

To ensure this relation holds, Q must be an anticommuting spinor. Additionally, since spinors are inherently complex, Q^\dagger must also be a generator of the supersymmetry transformation. Since Q and Q^\dagger are spinor objects (with $s = 1/2$), we can see that supersymmetry must be a spacetime symmetry. The Haag-Lopuszanski-Sohnius extension [66] of the Coleman-Mandula theorem [65] is quite restrictive about the forms of such a symmetry. Here, we simply write the (anti-) commutation relations [15] :

$$Q_\alpha, Q_{\dot{\alpha}}^\dagger = -2\sigma_{\alpha\dot{\alpha}\mu} P_\mu \quad (3.3)$$

$$Q_\alpha, Q_{\dot{\beta}} = Q_{\dot{\alpha}}^\dagger, Q_{\dot{\beta}}^\dagger = 0 \quad (3.4)$$

$$[P^\mu, Q_\alpha] = [P^\mu, Q_{\dot{\alpha}}^\dagger] = 0 \quad (3.5)$$

³⁴⁴ **Supermultiplets**

³⁴⁵ In a supersymmetric theory, we organize single-particle states into irreducible
³⁴⁶ representations of the supersymmetric algebra which are known as *supermultiplets*.
³⁴⁷ Each supermultiplet contains a fermion state $|F\rangle$ and a boson state $|B\rangle$; these two
³⁴⁸ states are the known as *superpartners*. These are related by some combination of
³⁴⁹ Q and Q^\dagger , up to a spacetime transformation. Q and Q^\dagger commute with the mass-
³⁵⁰ squared operator $-P^2$ and the operators corresponding to the gauge transformations
³⁵¹ [15]; in particular, the gauge interactions of the Standard Model. In an unbroken
³⁵² supersymmetric theory, this means the states $|F\rangle$ and $|B\rangle$ have exactly the same mass,
³⁵³ electromagnetic charge, electroweak isospin, and color charges. One can also prove
³⁵⁴ [15] that each supermultiplet contains the exact same number of bosonic (n_B) and
³⁵⁵ fermion (n_F) degrees of freedom. We now explore the possible types of supermultiples
³⁵⁶ one can find in a renormalizable supersymmetric theory.

³⁵⁷ Since each supermultiplet must contain a fermion state, the simplest type of
³⁵⁸ supermultiplet contains a single Weyl fermion state ($n_F = 2$) which is paired with
³⁵⁹ $n_B = 2$ scalar bosonic degrees of freedom. This is most conveniently constructed as
³⁶⁰ single complex scalar field. We call this construction a *scalar supermultiplet* or *chiral*
³⁶¹ *supermultiplet*. The second name is indicative; only chiral supermultiplets can contain
³⁶² fermions whose right-handed and left-handed components transform differently under
³⁶³ the gauge interactions (as of course happens in the Standard Model).

³⁶⁴ The second type of supermultiplet we construct is known as a *gauge* supermul-
³⁶⁵ tiplet. We take a spin-1 gauge boson (which must be massless due to the gauge
³⁶⁶ symmetry, so $n_B = 2$) and pair this with a single massless Weyl spinor¹. The gauge
³⁶⁷ bosons transform as the adjoint representation of the their respective gauge groups;
³⁶⁸ their fermionic partners, which are known as gauginos, must also. In particular,
³⁶⁹ the left-handed and right-handed components of the gaugino fermions have the same

¹Choosing an $s = 3/2$ massless fermion leads to nonrenormalizable interactions.

370 gauge transformation properties.

371 Excluding gravity, this is the entire list of supermultiplets which can participate
372 in renormalizable interactions in what is known as $N = 1$ supersymmetry. This
373 means there is only one copy of the supersymmetry generators Q and Q^\dagger . This is
374 essentially the only “easy” phenomenological choice, since it is the only choice in four
375 dimensions which allows for the chiral fermions and parity violations built into the
376 Standard Model, and we will not look further into $N > 1$ supersymmetry in this thesis.

377 The primary goal, after understanding the possible structures of the multiplets
378 above, is to fit the Standard Model particles into a multiplet, and therefore make
379 predictions about their supersymmetric partners. We explore this in the next section.

380 3.2 Minimally Supersymmetric Standard Model

381 To construct what is known as the MSSM [susyPrimer , 68–71], we need a few
382 ingredients and assumptions. First, we match the Standard Model particles with
383 their corresponding superpartners of the MSSM. We will also introduce the naming
384 of the superpartners (also known as *sparticles*). We discuss a very common additional
385 restraint imposed on the MSSM, known as R –parity. We also discuss the concept of
386 soft supersymmetry breaking and how it manifests itself in the MSSM.

387 Chiral supermultiplets

388 The first thing we deduce is directly from Sec.?? . The bosonic superpartners
389 associated to the quarks and leptons *must* be spin 0, since the quarks and leptons must
390 be arranged in a chiral supermultiplet. This is essentially the note above, since the
391 chiral supermultiplet is the only one which can distinguish between the left-handed
392 and right-handed components of the Standard Model particles. The superpartners of
393 the quarks and leptons are known as *squarks* and *sleptons*, or *sfermions* in aggregate.

394 (for ‘‘scalar quarks’’, ‘‘scalar leptons’’, and ‘‘scalar fermion’’²). The ‘‘s-’’ prefix
 395 can also be added to the individual quarks i.e. *selectron*, *sneutrino*, and *stop*. The
 396 notation is to add a \sim over the corresponding Standard Model particle i.e. \tilde{e} , the
 397 selectron is the superpartner of the electron. The two-component Weyl spinors of the
 398 Standard Model must each have their own (complex scalar) partner i.e. e_L, e_R have
 399 two distinct partners : \tilde{e}_L, \tilde{e}_R . As noted above, the gauge interactions of any of the
 400 sfermions are identical to those of their Standard Model partners.

Due to the scalar nature of the Higgs, it must obviously lie in a chiral supermultiplet. To avoid gauge anomalies and ensure the correct Yukawa couplings to the quarks and leptons[15], we must add additional Higgs bosons to any supersymmetric theory. In the MSSM, we have two chiral supermultiplets. The SM (SUSY) parts of the multiplets are denoted $H_u(\tilde{H}_u)$ and $H_d(\tilde{H}_d)$. Writing out H_u and H_d explicitly:

$$H_u = \begin{pmatrix} H_u^+ \\ H_u^0 \end{pmatrix} \quad (3.6)$$

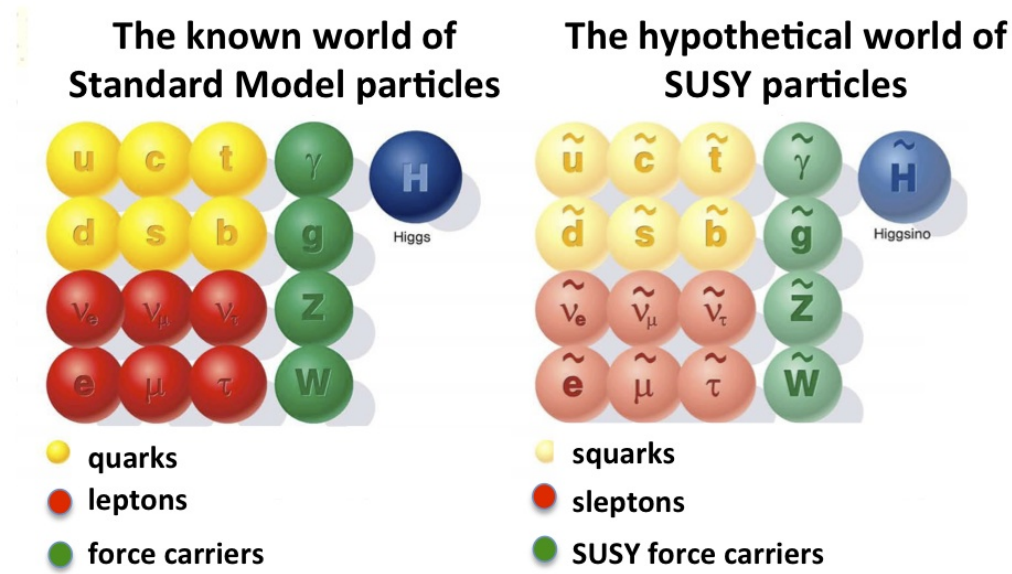
$$H_d = \begin{pmatrix} H_d^0 \\ H_d^- \end{pmatrix} \quad (3.7)$$

(3.8)

401 we see that H_u looks very similar to the SM Higgs with $Y = 1$, and H_d is symmetric
 402 to this with $+ \rightarrow -$, with $Y = -1$. The SM Higgs boson, h_0 , is a linear superposition
 403 of the neutral components of these two doublets. The SUSY parts of the Higgs
 404 multiplets, \tilde{H}_u and \tilde{H}_d , are each left-handed Weyl spinors. For generic spin-1/2
 405 sparticles, we add the ‘‘-ino’’ suffix. We then call the partners of the two Higgs
 406 collectively the *Higgsinos*.

²The last one should probably have bigger scare quotes.

Figure 3.1: Particles of the MSSM



407 Gauge supermultiplets

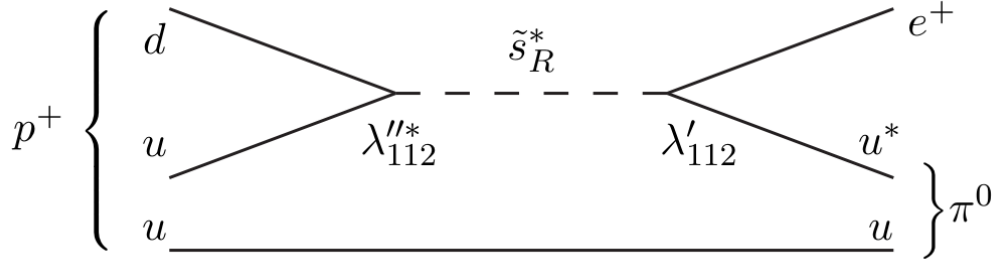
408 The superpartners of the gauge bosons must all be in gauge supermultiplets since
 409 they contain a spin-1 particle. Collectively, we refer to the superpartners of the
 410 gauge bosons as the gauginos.

411 The first gauge supermultiplet contains the gluon, and its superpartner, which is
 412 known as the *gluino*, denoted \tilde{g} . The gluon is of course the SM mediator of $SU(3)_C$;
 413 the gluino is also a colored particle, subject to $SU(3)_C$. From the SM before EWSB,
 414 we have the four gauge bosons of the electroweak symmetry group $SU(2)_L \otimes U(1)_Y$:
 415 $W^{1,2,3}$ and B^0 . The superpartners of these particles are thus the *winos* $W^{\tilde{1},\tilde{2},\tilde{3}}$ and
 416 *bino* \tilde{B}^0 , where each is placed in another gauge supermultiplet with its corresponding
 417 SM particle. After EWSB, without breaking supersymmetry, we would also have the
 418 zino \tilde{Z}^0 and photino $\tilde{\gamma}$.

419 The entire particle content of the MSSM can be seen in Fig.3.1.

420 At this point, it's important to take a step back. Where are these particles?
 421 As stated above, supersymmetric theories require that the masses and all quantum

Figure 3.2: This Feynmann diagram shows how proton decay is induced in the MSSM, if one does not impose R -parity.



422 numbers of the SM particle and its corresponding sparticle are the same. Of course,
 423 we have not observed a selectron, squark, or wino. The answer, as it often is, is that
 424 supersymmetry is *broken* by the vacuum state of nature [15].

425 **R -parity**

This section is a quick aside to the general story. R – parity refers to an additional discrete symmetry which is often imposed on supersymmetric models. For a given particle state, we define

$$R = (-1)^{3(B-L)+2s} \quad (3.9)$$

426 where B, L is the baryon (lepton) number and s is the spin. The imposition of
 427 this symmetry forbids certain terms from the MSSM Lagrangian that would violate
 428 baryon and/or lepton number. This is required in order to prevent proton decay, as
 429 shown in Fig.3.2³. .

430 In supersymmetric models, this is a \mathbb{Z}_2 symmetry, where SM particles have $R = 1$
 431 and sparticles have $R = -1$. We will take R – parity as part of the definition of
 432 the MSSM. We will discuss later the *drastic* consequences of this symmetry on SUSY
 433 phenomenology

³Proton decay can actually be prevented by allowing only one of the four potential R-parity violating terms to survive.

434 **Soft supersymmetry breaking**

The fundamental idea of *soft* supersymmetry breaking[15, 34, 35, 72, 73] is that we would like to break supersymmetry without reintroducing the quadratic divergences we discussed at the end of Chapter 2. We write the Lagrangian in a form :

$$\mathcal{L}_{\text{MSSM}} = \mathcal{L}_{\text{SUSY}} + \mathcal{L}_{\text{soft}} \quad (3.10)$$

435 In this sense, the symmetry breaking is “soft”, since we have separated out the
 436 completely symmetric terms from those soft terms which will not allow the quadratic
 437 divergences to the Higgs mass.

438 The explicitly allowed terms in the soft-breaking Lagrangian are [35].

- 439 • Mass terms for the scalar components of the chiral supermultipletss
 440 • Mass terms for the Weyl spinor components of the gauge supermultipletss
 441 • Trilinear couplings of scalar components of chiral supermultiplets

In particular, using the field content described above for the MSSM, the softly-broken portion of the MSSM Lagrangian can be written

$$\mathcal{L}_{\text{soft}} = -\frac{1}{2} \left(M_3 \tilde{g} \tilde{g} + M_2 \tilde{W} \tilde{W} + M_1 \tilde{B} \tilde{B} + c.c. \right) \quad (3.11)$$

$$- \left(\tilde{u} a_u \tilde{Q} H_u - \tilde{d} a_d \tilde{Q} H_d - \tilde{e} a_e \tilde{L} H_d + c.c. \right) \quad (3.12)$$

$$- \tilde{Q}^\dagger m_Q^2 \tilde{Q} - \tilde{L}^\dagger m_L^2 \tilde{L} - \tilde{u} m_u^2 \tilde{u}^\dagger - \tilde{d} m_d^2 \tilde{d}^\dagger - \tilde{e} m_e^2 \tilde{e}^\dagger \quad (3.13)$$

$$- m_{H_u}^2 H_u^* H_u - m_{H_d}^2 H_d^* H_d - (b H_u H_d + cc). \quad (3.14)$$

442 where we have introduced the following notations :

443 1. M_3, M_2, M_1 are the gluino, wino, and bino masses.

444 2. a_u, a_d, a_e are complex 3×3 matrices in family space.

445 3. $m_Q^2, m_u^2, m_d^2, m_L^2, m_e^2$ are hermitian 3×3 matrices in family space.

446 4. $m_{H_u}^2, m_{H_d}^2, b$ are the SUSY-breaking contributions to the Higgs potential.

447 We have written matrix terms without any sort of additional notational decoration
 448 to indicate their matrix nature, and we now show why. The first term 1 are
 449 straightforward; these are just the straightforward mass terms for these fields. There
 450 are strong constraints on the off-diagonal terms for the matrices of 2 [74, 75]; for
 451 simplicity, we will assume that each $a_i, i = u, d, e$ is proportional to the Yukawa
 452 coupling matrix : $a_i = A_{i0}y_i$. The matrices in ?? can be similarly constrained by
 453 experiments [68, 75–82] Finally, we assume that the elements 4 contributing to the
 454 Higgs potential as well as all of the 1 terms must be real, which limits the possible
 455 CP-violating interactions to those of the Standard Model. We thus only consider
 456 flavor-blind, CP-conserving interactions within the MSSM.

The important mixing for mass and gauge interaction eigenstates in the MSSM occurs within electroweak sector, in a process akin to EWSB in the Standard Model. The neutral portions of the Higgsinos doublets and the neutral gauginos ($\tilde{H}_u^0, \tilde{H}_d^0, \tilde{B}^0, \tilde{W}^0$) of the gauge interaction basis mix to form what are known as the *neutralinos* of mass basis :

$$M_{\tilde{\chi}} = \begin{pmatrix} M_1 & 0 & -c_\beta s_W m_Z & s_\beta s_W m_Z \\ 0 & M_2 & c_\beta c_W m_Z & -s_\beta c_W m_Z \\ -c_\beta s_W m_Z & c_\beta c_W m_Z & 0 & -\mu \\ s_\beta s_W m_Z & -s_\beta c_W m_Z & -\mu & 0 \end{pmatrix} \quad (3.15)$$

457 where $s(c)$ are the sine and cosine of angles related to EWSB, which introduced
 458 masses to the gauginos and higgsinos. Diagonalization of this matrix gives the four
 459 neutralino mass states, listed without loss of generality in order of increasing mass :
 460 $\tilde{\chi}_{1,2,3,4}^0$.

461 The neutralinos, especially the lightest neutralino $\tilde{\chi}_1^0$, are important ingredients
 462 in SUSY phenomenology.

463 The same process can be done for the electrically charged gauginos with
464 the charged portions of the Higgsino doublets along with the charged winos
465 $(\tilde{H}_u^+, \tilde{H}_d^+, \tilde{W}^+, \tilde{W}^-)$. This leads to the *charginos*, again in order of increasing mass
466 : $\tilde{\chi}_{1,2}^\pm$.

467

3.3 Phenomenology

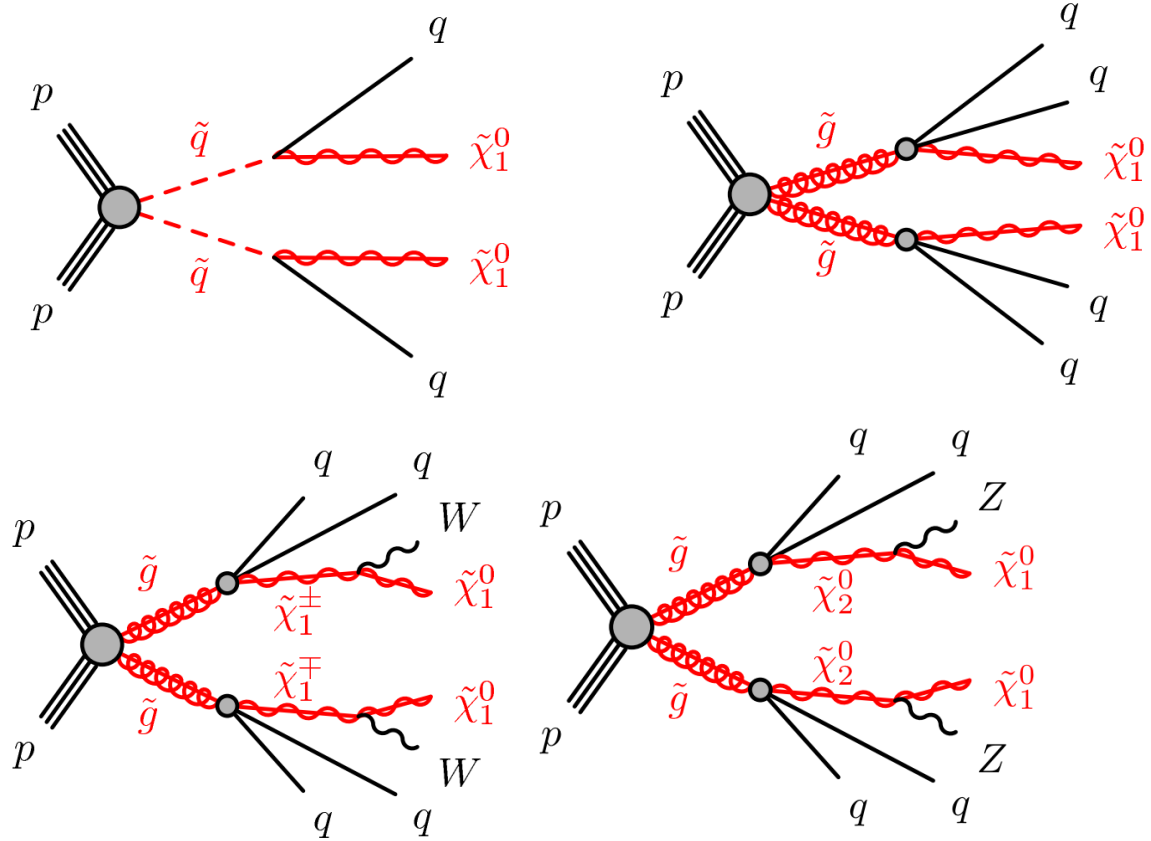
468 We are finally at the point where we can discuss the phenomenology of the MSSM,
469 in particular as it manifests itself at the energy scales of the LHC.

470 As noted above in Sec.3.2, the assumption of *R*–parity has important conse-
471 quences for MSSM phenomenology. The SM particles have $R = 1$, while the sparticles
472 all have $R = -1$. Simply, this is the “charge” of supersymmetry. Since the particles of
473 LHC collisions (pp) have total incoming $R = 1$, we must expect that all sparticles will
474 be produced in *pairs*. An additional consequence of this symmetry is the fact that the
475 lightest supersymmetric particle (LSP) is *stable*. Off each branch of the Feynmann
476 diagram shown in Fig., we have $R = -1$, and this can only decay to another sparticle
477 and a SM particle. Once we reach the lightest sparticle in the decay, it is absolutely
478 stable. This leads to the common signature E_T^{miss} for a generic SUSY signal.

479 For this thesis, we will be presenting an inclusive search for squarks and gluinos
480 with zero leptons in the final state. This is a very interesting decay channel⁴, due
481 to the high cross-sections of $\tilde{g}\tilde{g}$ and $\tilde{q}\tilde{q}$ decays, as can be seen in Fig.?? [83]. This
482 is a direct consequence of the fact that these are the colored particles of the MSSM.
483 Since the sparticles interact with the gauge groups of the SM in the same way as their
484 SM partners, the colored sparticles, the squarks and gluinos, are produced and decay
485 as governed by the color group $SU(3)_C$ with the strong coupling g_S . The digluino
486 production is particularly copious, due to color factor corresponding to the color octet

⁴Prior to Run1, probably the most *most* interesting SUSY decay channel.

Figure 3.3: SUSY signals considered in this thesis



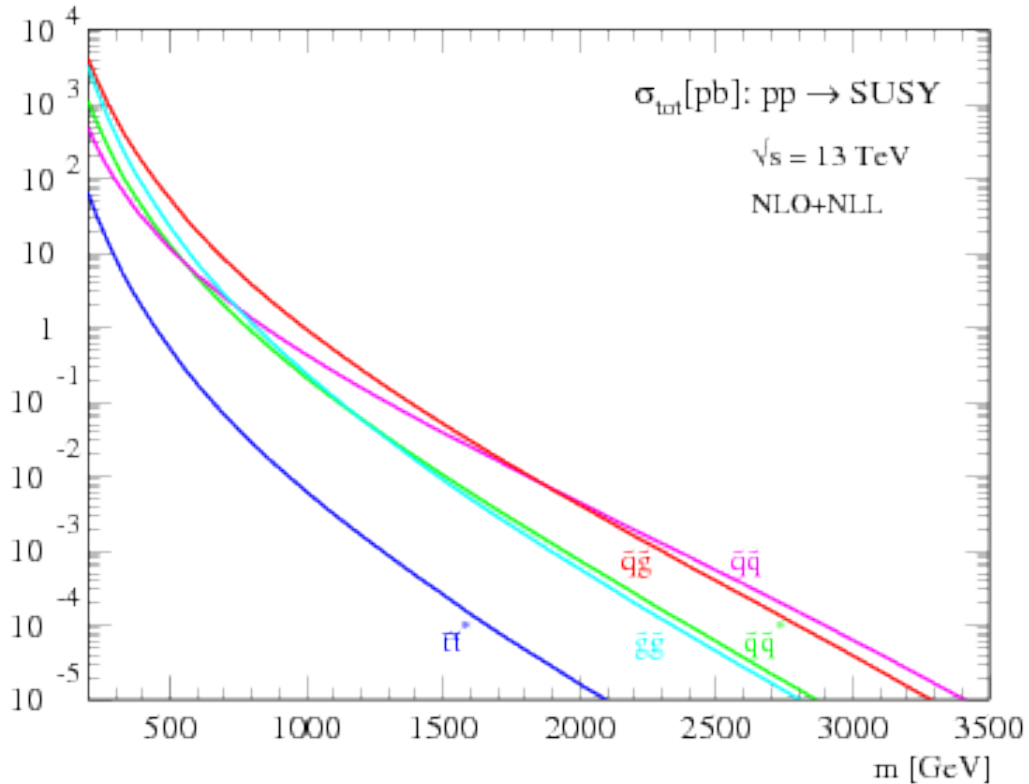
487 of $SU(3)C$.

488 In the case of disquark production, the most common decay mode of the squark in
 489 the MSSM is a decay directly to the LSP plus a single SM quark [15]. This means the
 490 basic search strategy of disquark production is two jets from the final state quarks,
 491 plus missing transverse energy for the LSPs. There are also cascade decays, the most
 492 common of which, and the only one considered in this thesis, is $\tilde{q} \rightarrow q\tilde{\chi}_1^\pm \rightarrow qW^\pm\chi_1^0$.

493 For digluino production, the most common decay is $\tilde{g} \rightarrow g\tilde{q}$, due to the large
 494 g_S coupling. The squark then decays as listed above. In this case, we generically
 495 search for four jets and missing transverse energy from the LSPs. We can also have
 496 the squark decay in association with a W^\pm or Z^0 ; in this thesis, we are interested in
 497 those cases where this vector boson goes hadronically.

498 In the context of experimental searches for SUSY, we often consider *simplified*

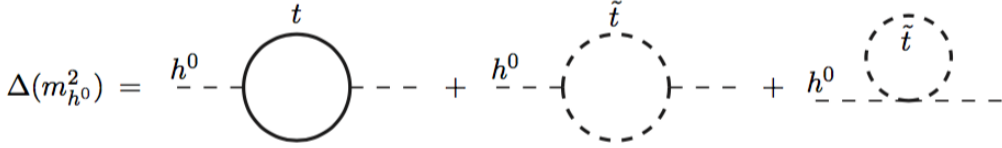
Figure 3.4: SUSY production cross-sections as a function of sparticle mass at $\sqrt{s} = 13$ TeV.



499 *models*. These models make certain assumptions which allow easy comparisons of
 500 results by theorists and rival experimentalists. In the context of this thesis, the
 501 simplified models will make assumptions about the branching ratios described in the
 502 preceding paragraphs. In particular, we will often choose a model where the decay of
 503 interest occurs with 100% branching ratio. This is entirely for ease of interpretation
 504 by other physicists⁵, but it is important to recognize that these are more a useful
 505 comparison tool, especially with limits, than a strict statement about the potential
 506 masses of sought-after beyond the Standard Model particle.

⁵In the author's opinion, this often leads to more confusion than comprehension. We will revisit the shortcomings of simplified models in the Conclusion to this thesis.

Figure 3.5: Loop diagrams correct the Higgs mass in the MSSM



507 3.4 How SUSY solves the problems with the SM

508 We now return to the issues with the Standard Model as described in Ch.2 to see
 509 how these issues are solved by supersymmetry.

510 Quadratic divergences to the Higgs mass

The quadratic divergences induced by the loop corrections to the Higgs mass, for example from the top Yukawa coupling, goes as

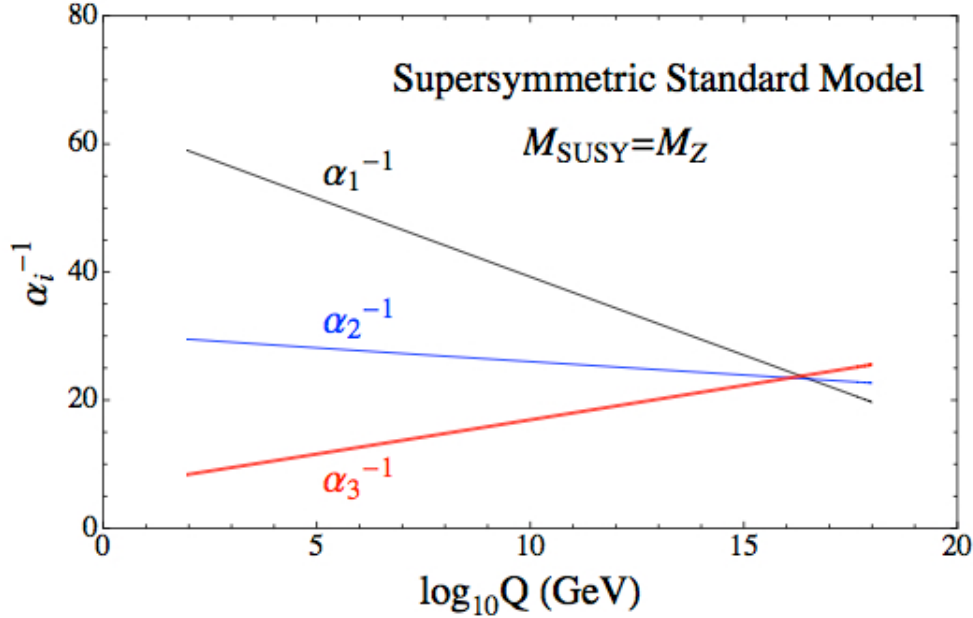
$$\delta m_H^2 \approx \left(\frac{m_t}{8\pi^2 \langle \phi \rangle_{VEV}} \right)^2 \Lambda_{Planck}^2. \quad (3.16)$$

511 The miraculous thing about SUSY is each of these terms *automatically* comes
 512 with a term which exactly cancels this contribution[15]. The fermions and bosons
 513 have opposite signs in this loop diagram to all orders in perturbation theory, which
 514 completely solves the hierarchy problem. This is the most well-motivated reason for
 515 supersymmetry.

516 Gauge coupling unification

517 An additional motivation for supersymmetry is seen by the gauge coupling unification
 518 high scales. In the Standard Model, as we saw the gauge couplings fail to unify at
 519 high energies. In the MSSM and many other forms of supersymmetry, the gauge
 520 couplings unify at high energy, as can be seen in Fig.???. This provides additional
 521 aesthetic motivation for supersymmetric theories.

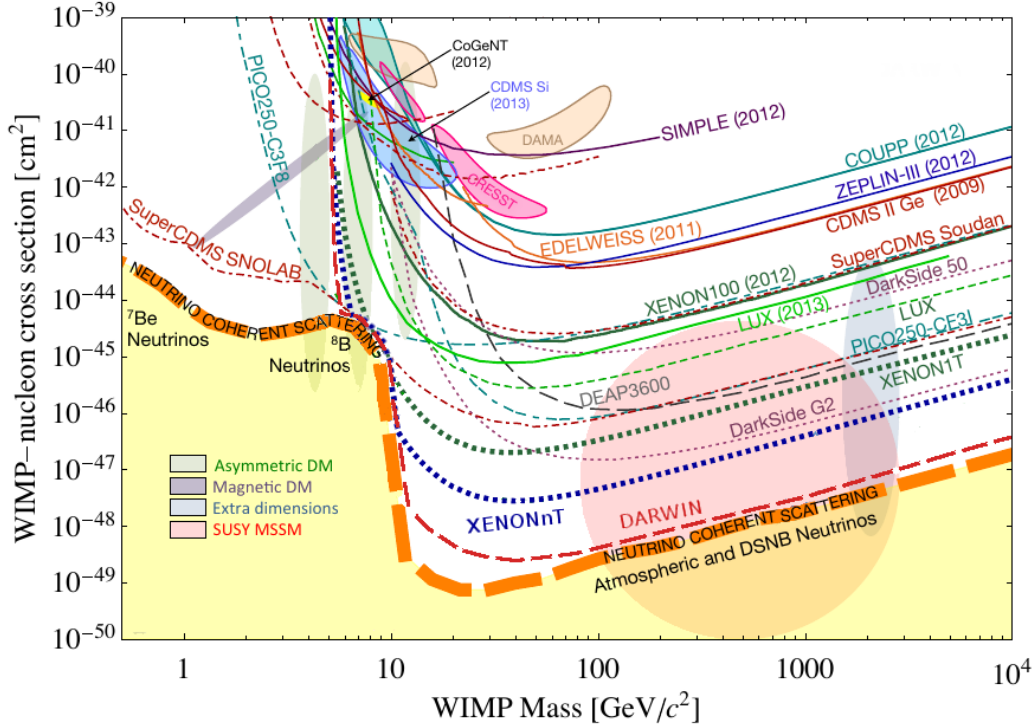
Figure 3.6: The running of Standard Model gauge couplings; compare to Fig.2.4. The MSSM gauge couplings nearly intersect at high energies.



522 Dark matter

523 As we discussed previously, the lack of any dark matter candidate in the Standard
 524 Model naturally leads to beyond the Standard Model theories. In the Standard Model,
 525 there is a natural dark matter candidate in the lightest supersymmetric particle[15]
 526 The LSP would in dark matter experiments be called a *weakly-interacting massive*
 527 *particle* (WIMP), which is a type of cold dark matter [22, 84]. These WIMPS would
 528 only interact through the weak force and gravity, which is exactly as a model like the
 529 MSSM predicts for the neutralino. In Fig.3.7, we can see the current WIMP exclusions
 530 for a given mass. The range of allowed masses which have not been excluded for LSPs
 531 and WIMPs have significant overlap. This provides additional motivation outside of
 532 the context of theoretical details.

Figure 3.7: WIMP exclusions from direct dark matter detection experiments.



3.5 Conclusions

Supersymmetry is the most well-motivated theory for physics beyond the Standard Model. It provides a solution to the hierarchy problem, leads to gauge coupling unification, and provides a dark matter candidate consistent with galactic rotation curves. As noted in this chapter, due to the LSPs in the final state, most SUSY searches require a significant amount of missing transverse energy in combination with jets of high transverse momentum. However, there is some opportunity to do better than this, especially in final states where one has two weakly-interacting LSPs on opposite sides of some potentially complicated decay tree. We will see how this is done in Ch.??.

The Large Hadron Collider

545 The Large Hadron Collider (LHC) produces high-energy protons which are collided
 546 at the center of multiple large experiments at CERN on the outskirts of Geneva,
 547 Switzerland [85]. The LHC produces the highest energy collisions in the world,
 548 with design center-of-mass energy of $\sqrt{s} = 14$ TeV, which allows the experiments
 549 to investigate physics far beyond the reach of previous colliders. This chapter will
 550 summarize the basics of accelerator physics, especially with regards to discovering
 551 physics beyond the Standard Model. We will describe the CERN accelerator complex
 552 and the LHC.

553 **4.1 Basics of Accelerator Physics**

554 This section follows closely the presentation of [86].

Simple particle accelerators simply rely on the acceleration of charged particles in a static electric field. Given a field of strength E , charge q , and mass m , this is simply

$$a = \frac{qE}{m}. \quad (4.1)$$

555 For a given particle with a given mass and charge, this is limited by the static electric
 556 field which can be produced, which in turn is limited by electrical breakdown at high
 557 voltages.

558 There are two complementary solutions to this issue. First, we use the *radio*
 559 *frequency acceleration* technique. We call the devices used for this *RF cavities*. The

560 cavities produce a time-varied electric field, which oscillate such that the charged
561 particles passing through it are accelerated towards the design energy of the RF
562 cavity. This oscillation also induces the particles into *bunches*, since particles which
563 are slightly off in energy from that induced by the RF cavity are accelerated towards
564 the design energy.

Second, one bends the particles in a magnetic field, which allows them to pass through the same RF cavity over and over. This second process is often limited by *synchrotron radiation*, which describes the radiation produced when a charged particle is accelerated. The power radiated is

$$P \sim \frac{1}{r^2} \left(E/m \right)^4 \quad (4.2)$$

565 where r is the radius of curvature and E, m is the energy (mass) of the charged
566 particle. Given an energy which can be produced by a given set of RF cavities (which
567 is *not* limited by the mass of the particle), one then has two options to increase the
568 actual collision energy : increase the radius of curvature or use a heavier particle.
569 Practically speaking, the easiest options for particles in a collider are protons and
570 electrons, since they are (obviously) copious in nature and do not decay¹. Given the
571 dependence on mass, we can see why protons are used to reach the highest energies.
572 The tradeoff for this is that protons are not point particles, and we thus we don't
573 know the exact incoming four-vectors of the protons, as discussed in Ch.2.

The particle *beam* refers to the bunches all together. An important property of a beam of a particular energy E , moving in uniform magnetic field B , containing particles of momentum p is the *beam rigidity* :

$$R \equiv rB = p/c. \quad (4.3)$$

574 The linear relation between r and p , or alternatively B and p have important
575 consequences for LHC physics. For hadron colliders, this is the limiting factor on

¹Muon colliders are a really cool option at high energies, since the relativistic γ factor gives them a relatively long lifetime in the lab frame.

576 going to higher energy scales; one needs a proportionally larger magnetic field to
577 keep the beam accelerating in a circle.

578 Besides the rigidity of the beam, the most important quantities to characterize
579 a beam are known as the (normalized) *emittance* ϵ_N and the *betatron function* β .
580 These quantities determine the transverse size σ of a relativistic beam $v \gtrsim c$ beam :
581 $\sigma^2 = \beta^* \epsilon_N / \gamma_{\text{rel}}$, where β^* is the value of the betatron function at the collision point
582 and γ_{rel} is the Lorentz factor.

These quantities determine the *instantaneous luminosity* L of a collider, which combined with the cross-section σ of a particular physics process, give the rate of this physics process :

$$R = L\sigma. \quad (4.4)$$

The instantaneous luminosity L is given by :

$$L = \frac{f_{\text{rev}} N_b^2 F}{4\pi\sigma^2} = \frac{f_{\text{rev}} n N_b^2 \gamma_{\text{rel}} F}{4\pi\beta^* \epsilon_N}. \quad (4.5)$$

583 Here we have introduced the frequency of revolutions f_{rev} , the number of bunches n ,
584 the number of protons per bunch N_b^2 , and a geometric factor F related to the crossing
585 angle of the beams.

The *integrated luminosity* $\int L$ gives the total number of a particular physics process P , with cross-section σ_P .

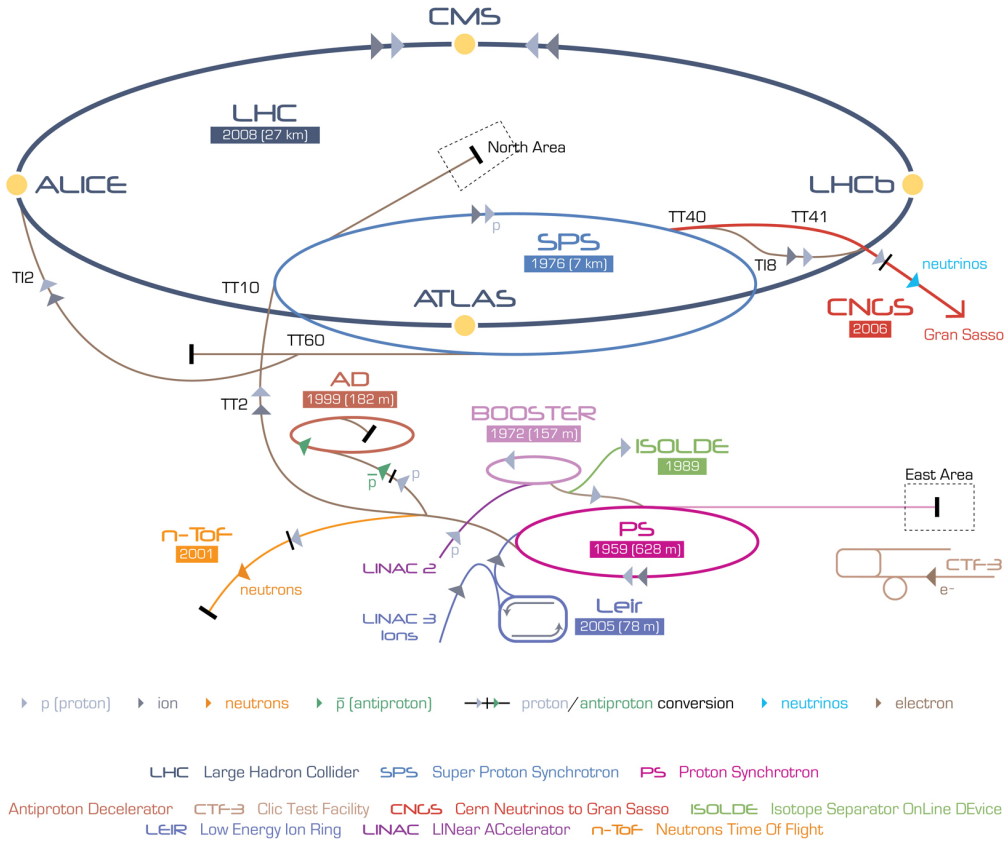
$$N_P = \sigma_P \int L. \quad (4.6)$$

586 Due to this simple relation, one can also quantify the “amount of data delivered” by
587 a collider simply by $\int L$.

588 4.2 Accelerator Complex

589 The Large Hadron Collider is the last accelerator in a chain of accelerators which
590 together form the CERN accelerator complex, which can be seen in 4.1. The protons

Figure 4.1: The CERN accelerator complex.



begin their journey to annihilation in a hydrogen source, where they are subsequently ionized. The first acceleration occurs in the Linac 2, a linear accelerator composed of RF cavities. The protons leave the Linac 2 at an energy of 50 MeV and enter the Proton Synchrotron Booster (PSB). The PSB contains four superimposed rings, which accelerate the protons to 1.4 GeV. The protons are then injected into the Proton Synchrotron (PS). This synchrotron increases the energy up to 25 GeV. After leaving the PS, the protons enter the Super Proton Synchrotron (SPS). This is the last step before entering the LHC ring, and the protons are accelerated to 450 GeV. From the SPS, the protons are injected into the beam pipes of the LHC. The process to fill the LHC rings with proton bunches from start to finish typically takes about four minutes.

602 **4.3 Large Hadron Collider**

The Large Hadron Collider is the final step in the CERN accelerator complex, and produces the collisions analyzed in this thesis. From the point of view of experimentalists on the general-purpose ATLAS and CMS experiments, the main goal of the LHC is to deliver collisions at the highest possible energy, with the highest possible instantaneous luminosity. The LHC was installed in the existing 27 km tunnel used by the Large Electron Positron (LEP) collider [87]. This allowed the existing accelerator complex at CERN, described in the previous section, to be used as the injection system to prepare the protons up to 450 GeV. Many aspects of the LHC design were decided by this very fact, and specified the options allowed to increase the energy or luminosity. In particular, the radius of the tunnel was already specified; from Eq.4.3, this implies the momentum (or energy) of the beam is entirely determined by the magnetic field. Given the 27 km circumference of the LEP tunnel, one can calculate the required magnetic field to reach the 7 TeV per proton design energy of the LHC :

$$r = C/2\pi = 4.3 \text{ km} \quad (4.7)$$

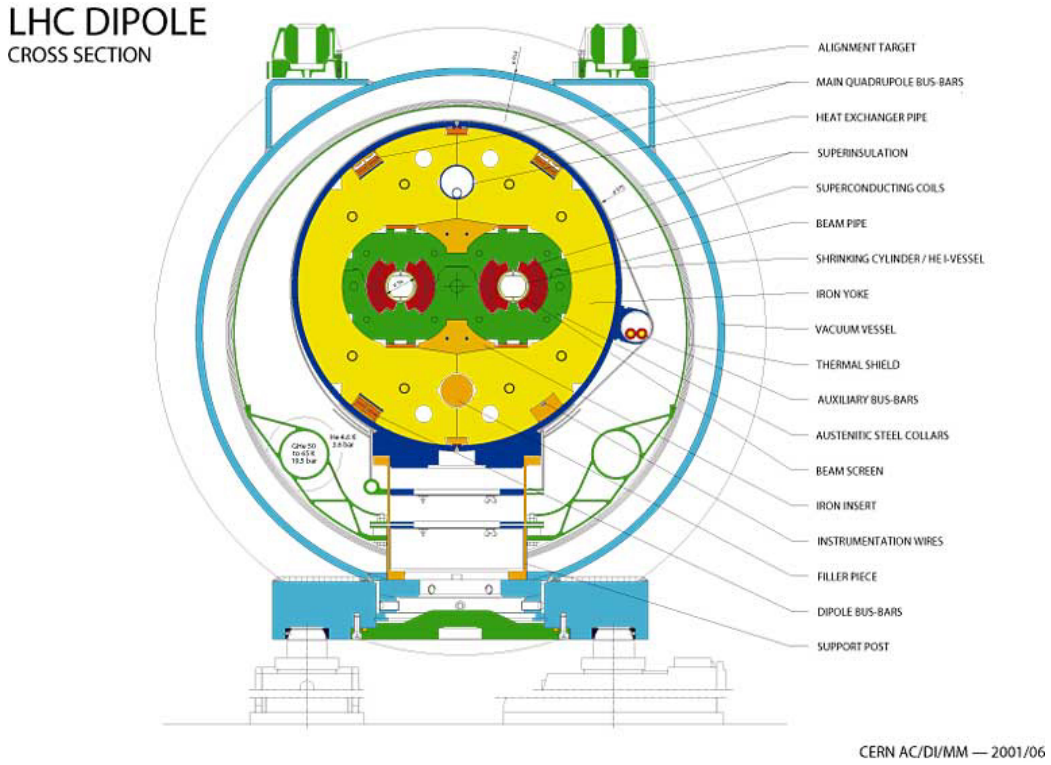
$$\rightarrow B = \frac{p}{rc} = 5 \text{ T} \quad (4.8)$$

603 In fact, the LHC consists of 8 528 m straight portions consisting of RF cavities, used
604 to accelerate the particles, and 8 circular portions which bend the protons around the
605 LHC ring. These circular portions actually have a slightly smaller radius of curvature
606 $r = 2804 \text{ m}$, and we require $B = 8.33 \text{ T}$. To produce this large field, we need to use
607 superconducting magnets, as discussed in the next section.

608 **Magnets**

609 There are many magnets used by the LHC machine, but the most important are the
610 1232 dipole magnets; a schematic is shown in Fig.4.2 and a photograph is shown in

Figure 4.2: Schematic of an LHC dipole magnet.



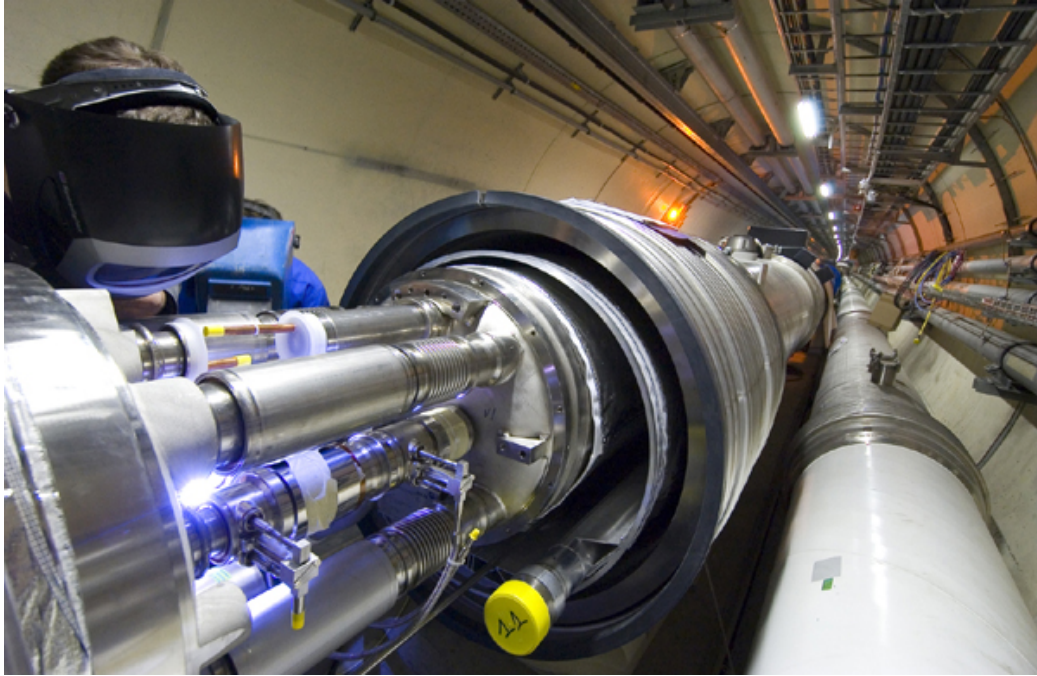
611 Fig.4.3.

612 The magnets are made of Niobium and Titanium. The maximum field strength is
 613 10 T when cooled to 1.9 Kelvin. The magnets are cooled by superfluid helium, which
 614 is supplied by a large cryogenic system. Due to heating between the eight helium
 615 refrigerators and the beampipe, the helium is cooled in the refrigerators to 1.8 K.

616 A failure in the cooling system can cause what is known as a *quench*. If the
 617 temperature goes above the critical superconducting temperature, the metal loses its
 618 superconducting properties, which leads to a large resistance in the metal. This leads
 619 to rapid temperature increases, and can cause extensive damages if not controlled.

620 The dipole magnets are 16.5 meters long with a diameter of 0.57 meters. There
 621 are two individual beam pipes inside each magnet, which allows the dipoles to house
 622 the beams travelling in both directions around the LHC ring. They curve slightly,
 623 at an angle of 5.1 mrad, which carefully matches the curvature of the ring. The

Figure 4.3: Photograph of a technician connecting an LHC dipole magnet.



624 beampipes inside of the magnets are held in high vacuum, to avoid stray particles
625 interacting with the beam.

626 **4.4 Dataset Delivered by the LHC**

627 In this thesis, we analyze the data delivered by the LHC to ATLAS in the 2015 and
628 2016 datasets. The beam parameters relevant to this dataset are available in Table
629 [4.1](#).

630 The peak instantaneous luminosity delivered in 2015 (2016) was $L =$
631 $5.2(11) \text{ cm}^{-2}\text{s}^{-1} \times 10^{33}$. One can note that the instantaneous luminosity delivered in
632 the 2016 dataset exceeds the design luminosity of the LHC. The total integrated
633 luminosity delivered was 13.3 fb^{-1} . In Figure [4.4](#), we display the integrated luminosity
634 as a function of day for 2015 and 2016.

Figure 4.4: Integrated Luminosity delivered by the LHC and collected by ATLAS in the 2015 and 2016 datasets.

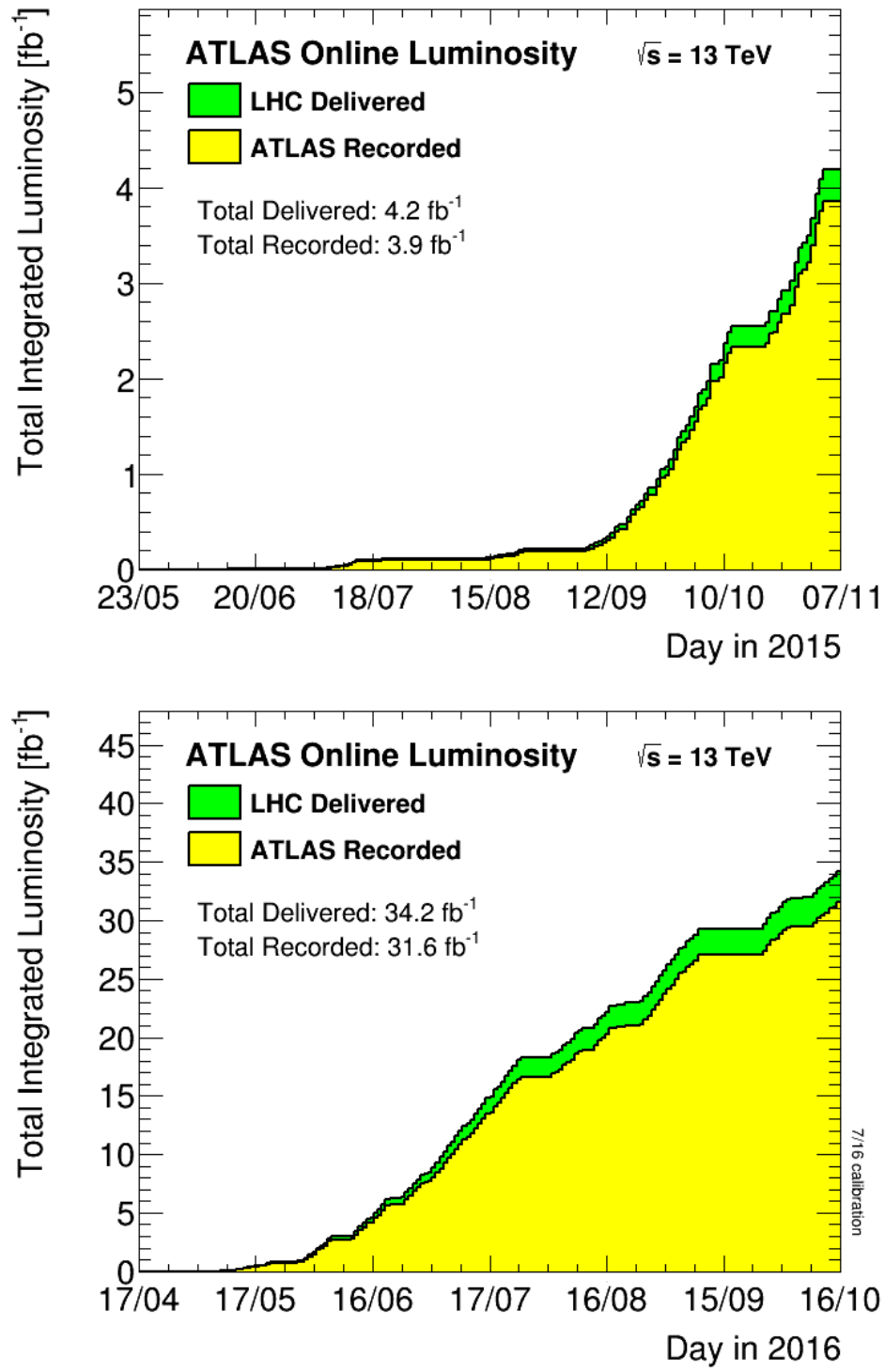
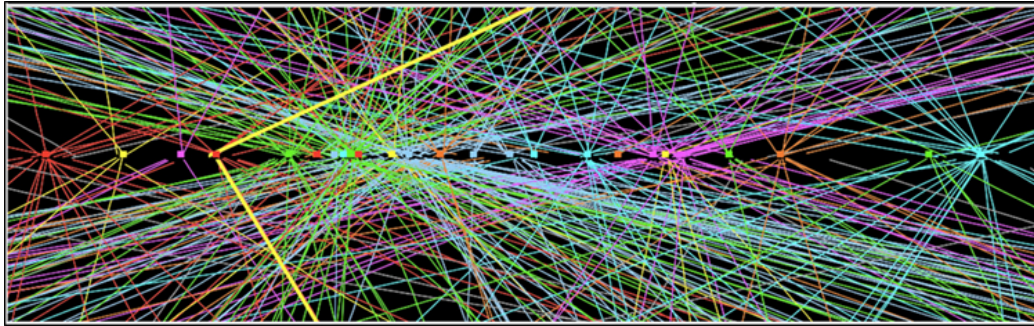


Table 4.1: Beam parameters of the Large Hadron Collider.

Parameter	Injection	Extraction
Energy (GeV)	450	7000
Rigidity (T-m)	3.8	23353
Bunch spacing (ns)	25	25
Design Luminosity ($\text{cm}^{-2}\text{s}^{-1} \times 10^{34}$)	-	1.0
Bunches per proton beam	2808	2808
Protons per bunch	1.15 e11	1.15 e11
Beam lifetime (hr)	-	10
Normalized Emittance ϵ_N (mm μrad)	3.3	3.75
Betatron function at collision point β^* (cm)	-	55

Figure 4.5: Simulated event with many pileup vertices.



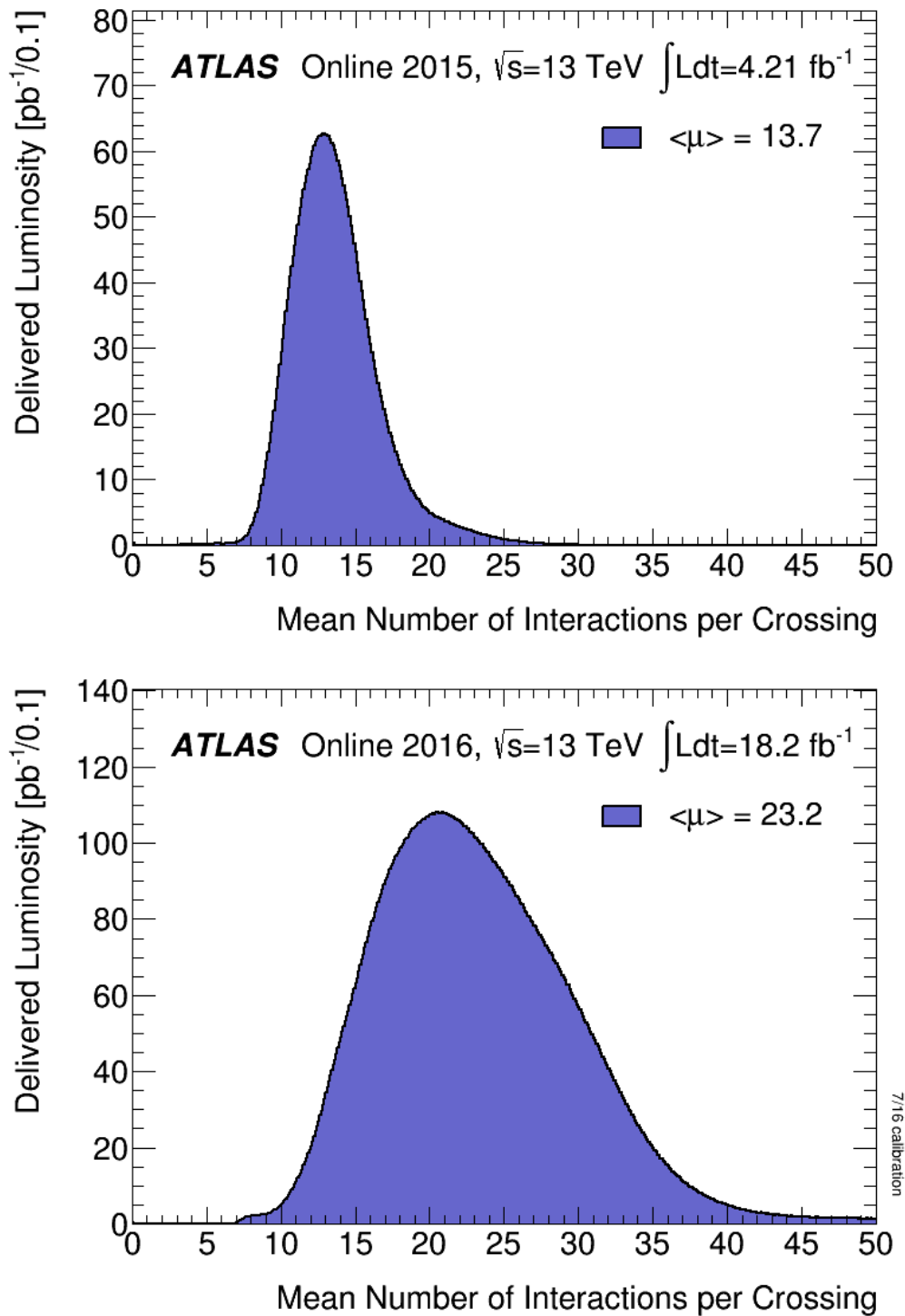
635 Pileup

636 *Pileup* is the term for the additional proton-proton interactions which occur during
 637 each bunch crossing of the LHC. At the beginning of the LHC physics program, there
 638 had not been a collider which averaged more than a single interaction per bunch
 639 crossing. In the LHC, each bunch crossing (or *event*) generally contains multiple
 640 proton-proton interactions. An simulated event with many *vertices* can be seen in
 641 Fig.4.5. The so-called *primary vertex* (or *hard scatter vertex*) refers to the vertex
 642 which has the highest Σp_T^2 ; this summation occurs over the *tracks* in the detector,
 643 which we will describe later[**ATL-INDET-PUB-2009-001**]. We then distinguish
 644 between *in-time* pileup and *out-of-time* pileup. In-time pileup refers to the additional
 645 proton-proton interactions which occur in the event. Out-of-time pileup refers to
 646 effects related to proton-proton interactions previous bunch crossings.

647 We quantify in-time pileup by the number of “primary”² vertices in a particular
648 event. To quantify the out-of-time pileup, we use the average number of interactions
649 per bunch crossing $\langle \mu \rangle$ over some human-scale time. In Figure 4.6, we show the
650 distribution of μ for the dataset used in this thesis.

²The primary vertex is as defined above, but we unfortunately use the same name here.

Figure 4.6: Mean number of interactions per bunch crossing in the 2015 and 2016 datasets.



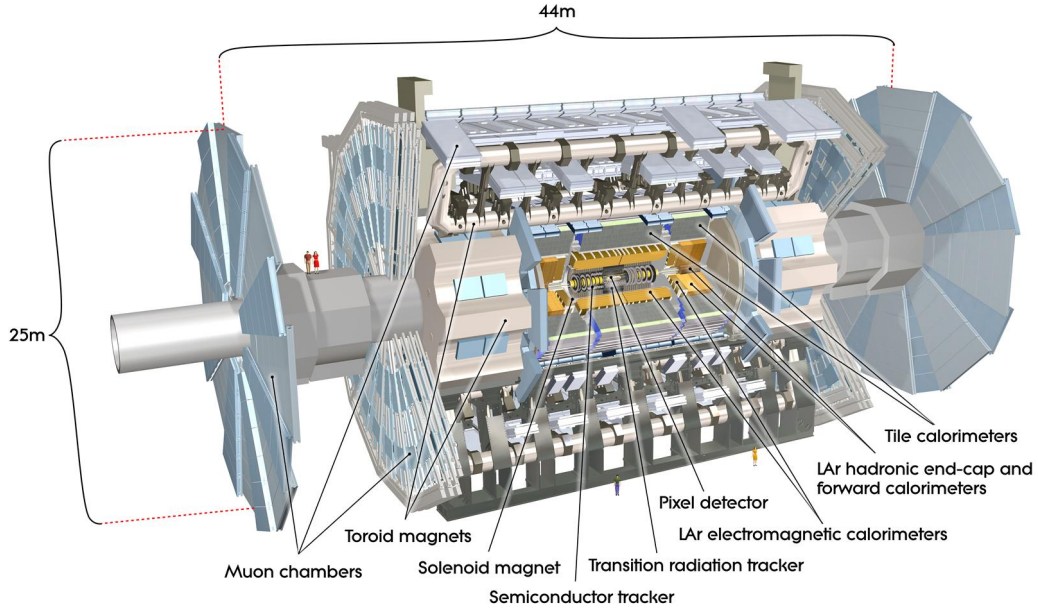
The ATLAS detector

653 The dataset analyzed in this thesis was taken by the ATLAS detector [88], which is
 654 located at the “Point 1” cavern of the LHC beampipe, just across the street from
 655 the main CERN campus. The much-maligned acronym stands for *A Toroidal LHC*
 656 *ApparatuS*. ATLAS is a massive cylindrical detector, with a radius of 12.5 m and a
 657 length of 44 m, with nearly hermitic coverage around the collision point. It consists
 658 of multiple subdetectors; each plays a role in ATLAS’s ultimate purpose of measuring
 659 the energy, momentum, and type of the particles produced in collisions delivered by
 660 the LHC. These subdetectors are immersed in a hybrid solenoid-toroid magnet system
 661 whichs forces charged particles to curve, which allows for precise measurements of
 662 their momenta. These magnetic fields are maximized in the central solenoid magnet,
 663 which contains a magnetic field of 2 T. A schematic of the detector can be seen in
 664 [5.1](#).

665 The *inner detector* (ID) lies closest to the collision point, and contains three
 666 separate subdetectors. It provides pseudorapidity¹coverage of $|\eta| < 2.5$ for charged
 667 particles to interact with the tracking material. The tracks reconstructed from the
 668 inner detector hits are used to reconstruct the primary vertices, as noted in Ch.??,

¹ATLAS uses a right-handed Cartesian coordinate system; the origin is defined by the nominal beam interaction point. The positive- z direction is defined by the incoming beam travelling counterclockwise around the LHC. The positive- x direction points towards the center of the LHC ring from the origin, and the positive- y direction points upwards towards the sky. For particles of transverse (in the $x - y$ plane) momentum $p_T = \sqrt{p_x^2 + p_y^2}$ and energy E , it is generally most convenient fully describe this particle’s kinematics as measured by the detector in the (p_T, ϕ, η, E) basis. The angle $\phi = \arctan(p_y/p_x)$ is the standard azimuthal angle, and $\eta = \ln \tan(\theta/2)$ is known as the pseudorapidity, and defined based on the standard polar angle $\theta = \arccos(p_z/p_T)$. For locations of i.e. detector elements, both (r, ϕ, η) and (z, ϕ, η) can be useful.

Figure 5.1: The ATLAS detector

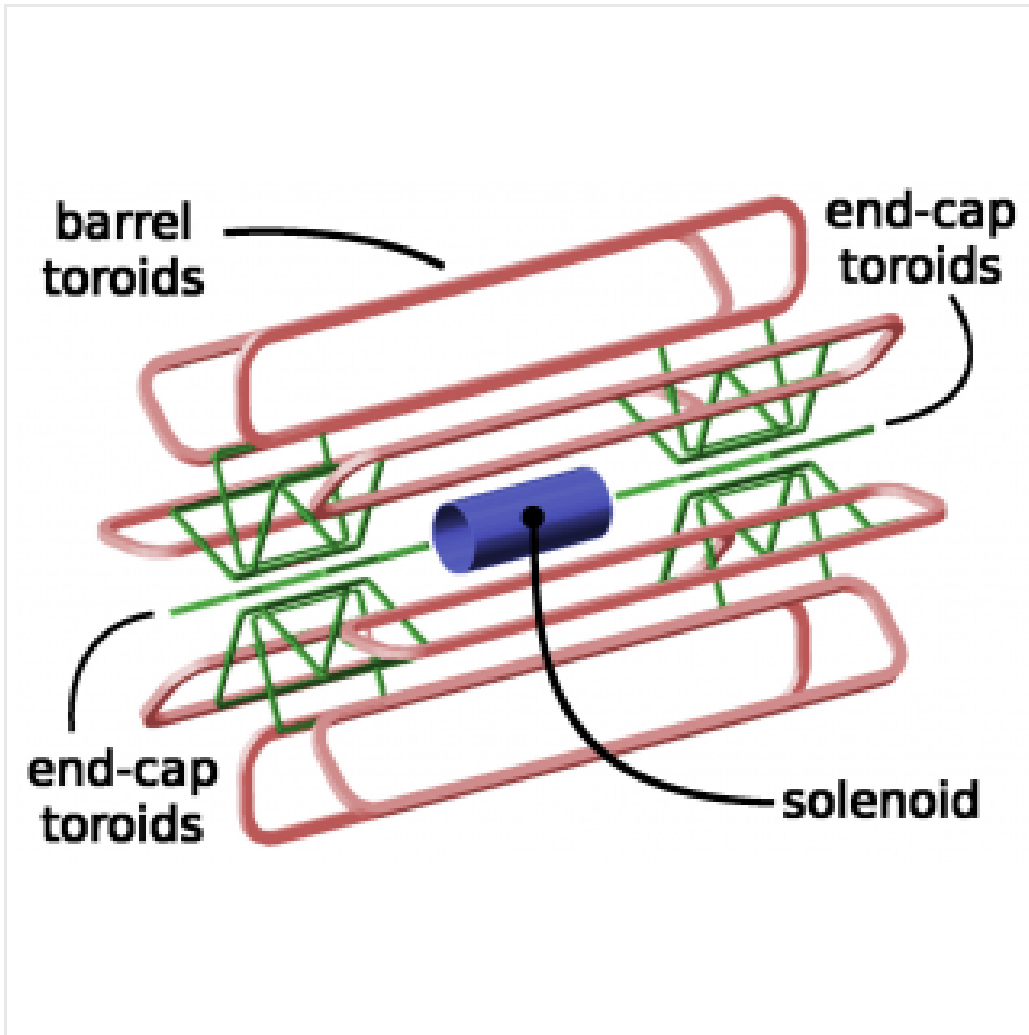


and to determine the momenta of charged particles. The ATLAS *calorimeter* consists of two subdetectors, known as the *electromagnetic* and *hadronic* calorimeters. These detectors stop particles in their detector material, and measure the energy deposition inside, which measures the energy of the particles deposited. The calorimeters provide coverage out to pseudorapidity of $|\eta| < 4.9$. The muon spectrometer is aptly named; it is specifically used for muons, which are the only particles which generally reach the outer portions of the detector. In this region, we have the large tracking systems of the muon spectrometer, which provide precise measurements of muon momenta. The muon spectrometer has pseudorapidity coverage of $|\eta| < 2.7$.

5.1 Magnets

ATLAS contains multiple magnetic systems; primarily, we are concerned with the solenoid, used by the inner detector, and the toroids located outside of the ATLAS calorimeter. A schematic is shown in Fig.5.2. These magnetic fields are used to bend

Figure 5.2: The ATLAS magnet system

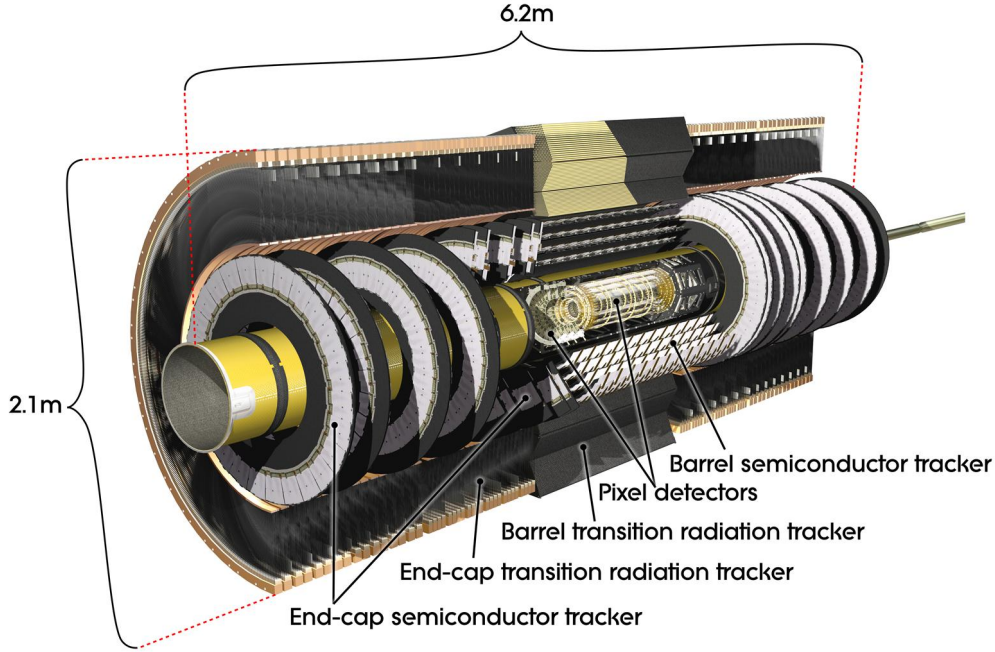


682 charged particles under the Lorentz force, which subsequently allows one to measure
683 their momentum.

684 The ATLAS central solenoid is a 2.3 m diameter, 5.3 m long solenoid at the center
685 of the ATLAS detector. It produces a uniform magnetic field of 2 T; this strong field
686 is necessary to accurately measure the charged particles in this field. An important
687 design constraint for the central solenoid was the decision to place it in between the
688 inner detector and the calorimeters. To avoid excessive impacts on measurements in
689 the calorimetry, the central solenoid must be as transparent as possible².

²This is also one of the biggest functional differences between ATLAS and CMS; in CMS, the

Figure 5.3: The ATLAS inner detector



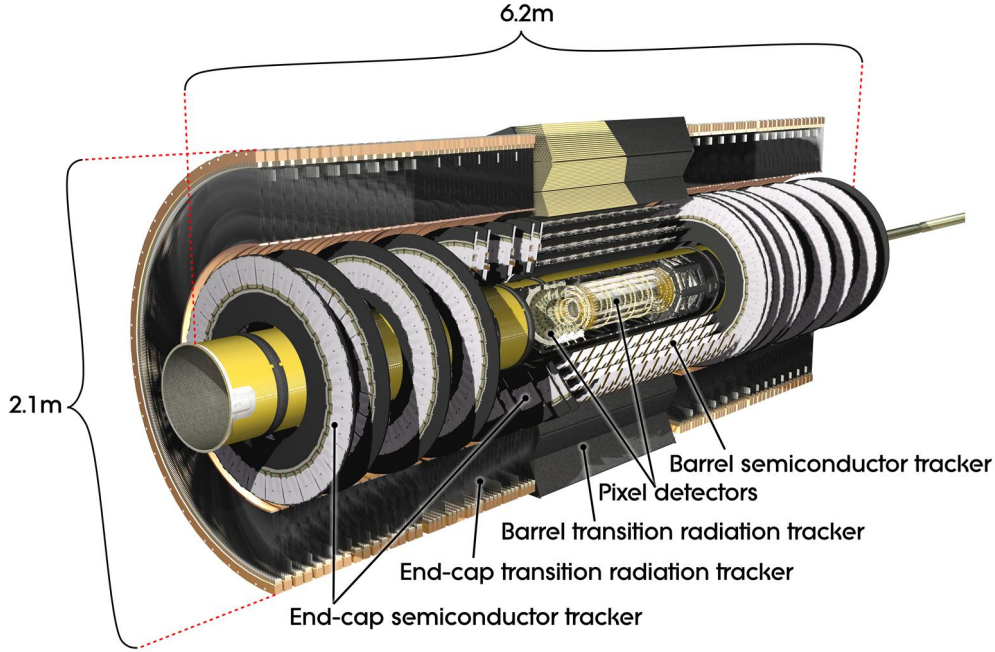
690 The toroid system consists of eight air-core superconducting barrel loops; these
691 give ATLAS its distinctive shape. There are also two endcap air-core magnets. These
692 produce a magnetic field in a region of approximately 26 m in length and 10 m of
693 radius. The magnetic field in this region is non-uniform, due to the prohibitive costs
694 of a solenoid magnet of that size.

695 **5.2 Inner Detector**

696 The ATLAS inner detector consists of three separate tracking detectors, which are
697 known as, in order of increasing distance from the interaction point, the Pixel
698 Detector, Semiconductor Tracker (SCT), and the Transition Radiation Tracker
699 (TRT). When charged particles pass through these tracking layers, they produce
700 *hits*, which using the known 2 T magnetic field, allows the reconstruction of *tracks*.
701 Tracks are used as inputs for reconstruction of many higher-level physics objects,

solenoid is outside of the calorimeters.

Figure 5.4: The ATLAS pixel detector



such as electrons, muons, photons, and E_T^{miss} . Accurate track reconstruction is thus crucial for precise measurements of charged particles.

Pixel Detector

The ATLAS pixel detector consists four layers of silicon “pixels”. This refers to the segmentation of the active medium into the pixels; compare to the succeeding silicon detectors, which will use silicon “strips”. This provides precise 3D hit locations. The layers are known as the “Insertable”³B-Layer (IBL), the B-Layer (or Layer-0), Layer-1, and Layer-2, in order of increasing distance from the interaction point. These layers are very close to the interaction point, and therefore experience a large amount of radiation.

Layer-1, Layer-2, and Layer-3 were installed with the initial construction of ATLAS. They contain front-end integrated electronics (FEI3s) bump-bonded to 1744

³Very often, the IBL is mistakenly called the Inner B-Layer, which would have been a much more sensible name.

714 silicon modules; each module is $250\ \mu\text{m}$ in thickness and contains 47232 pixels. These
715 pixels have planar sizes of $50 \times 400\ \mu\text{m}^2$ or $50 \times 600\ \mu\text{m}^2$, to provide highly accurate
716 location information. The FEI3s are mounted on long rectangular structures known
717 as staves, which encircle the beam pipe. A small tilt to each stave allows full coverage
718 in ϕ even with readout systems which are installed. These layers are at radia of 50.5
719 mm, 88.5 mm, and 122.5 mm from the interaction point.

720 The IBL was added to ATLAS after Run1 in 2012 at a radius of 33 mm from the
721 interaction point. The entire pixel detector was removed from the center of ATLAS
722 to allow an additional pixel layer to be installed. The IBL was required to preserve
723 the integrity of the pixel detector as radiation damage leads to inoperative pixels in
724 the other layers. The IBL consists of 448 FEI4 chips, arranged onto 14 staves. Each
725 FEI4 has 26880 pixels, of planar size $50 \times 250\ \mu\text{m}$. This smaller granularity was
726 required due to the smaller distance to the interaction point.

727 In total, a charged particle passing through the inner detector would expect to
728 leave four hits in the pixel detector.

729 Semiconductor Tracker

730 The SCT is directly beyond Layer-2 of the pixel detector. This is a silicon strip
731 detector, which do not provide the full 3D information of the pixel detector. The
732 dual-sensors of the SCT contain 2×768 individual strips; each strip has area $6.4\ \text{cm}^2$.
733 The SCT dual-sensor is then double-layered, at a relative angle of 40 mrad;
734 together these layers provide the necessary 3D information for track reconstruction.
735 There are four of these double-layers, at radia of 284 mm, 355 mm, 427 mm, and 498
736 mm. These double-layers provide hits comparable to those of the pixel detector, and
737 we have four additional hits to reconstruct tracks for each charged particle.

Figure 5.5: A ring of the Semiconductor Tracker

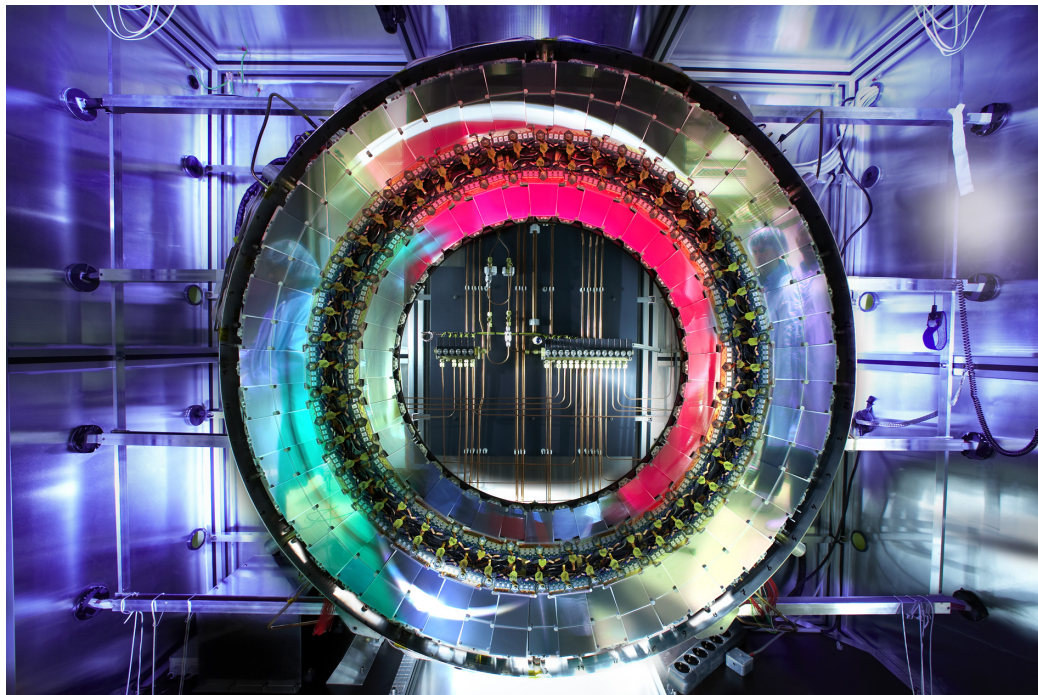
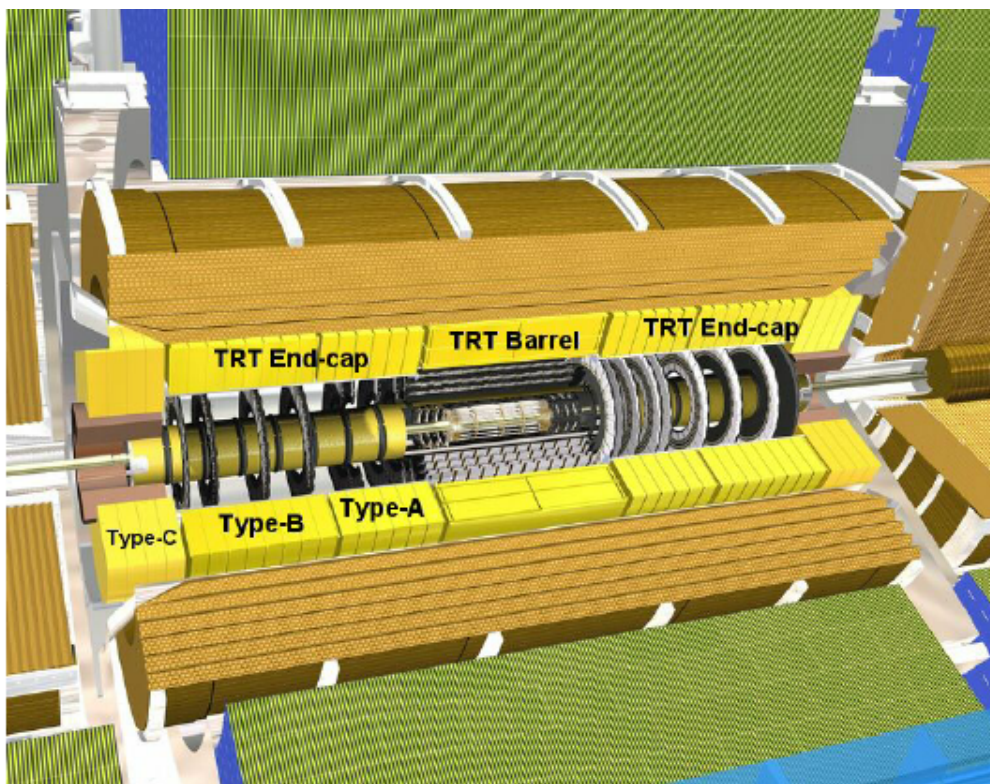


Figure 5.6: A schematic of the Transition Radiation Tracker



738 **Transition Radiation Tracker**

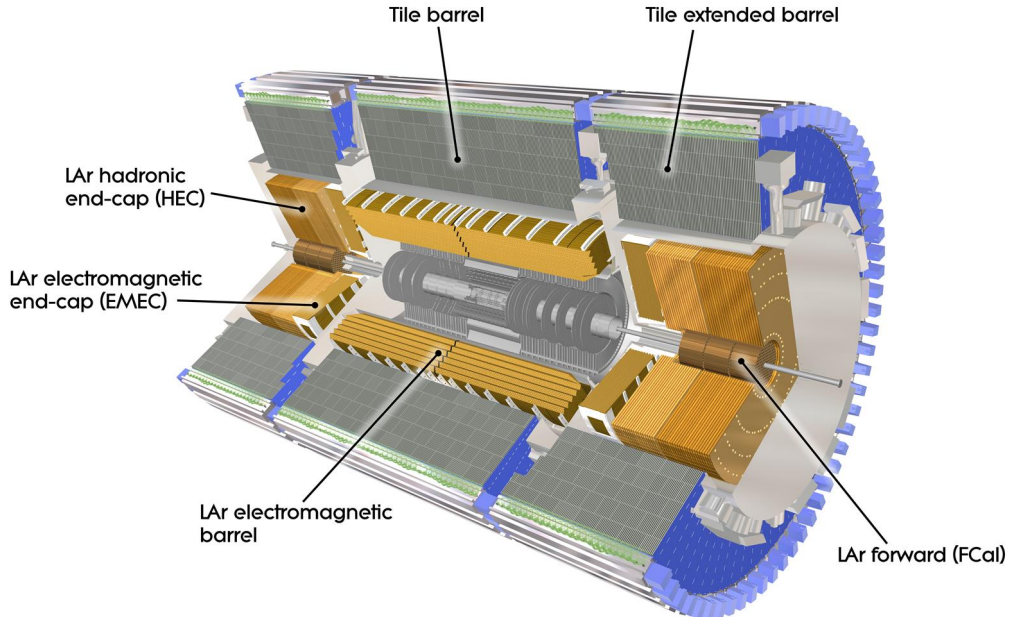
739 The Transition Radiation Tracker is the next detector radially outward from the SCT.
740 It contains straw drift tubes; these contain a tungsten gold-plated wire of $32 \mu\text{m}$
741 diameter held under high voltage (-1530 V) with the edge of the Kapton-aluminum
742 tube. They are filled with a gas mixture of primarily xenon that is ionized when
743 a charged particle passes through the tube. The ions are collected by the “drift”
744 due to the voltage inside the tubes, which is read out by the electronics. This gives
745 so-called “continuous tracking” throughout the tube, due to the large number of ions
746 produced.

747 The TRT is so-named due to the *transition radiation* (TR) it induces. Due to
748 the dielectric difference between the gas and tubes, TR is induced. This is important
749 for distinguishing electrons from their predominant background of minimum ionizing
750 particles. Generally, electrons have a much larger Lorentz factor than minimum
751 ionizing particles, which leads to additional TR. This can be used as an additional
752 handle for electron reconstruction.

753 **5.3 Calorimetry**

754 The calorimetry of the ATLAS detector also includes multiple subdetectors; these sub-
755 detectors allow precise measurements of the electrons, photons, and hadrons produced
756 by the ATLAS detector. Generically, calorimeters work by stopping particles in their
757 material, and measuring the energy deposition. This energy is deposited as a cascade
758 particles induce from interactions with the detector material known *showers*. ATLAS
759 uses *sampling* calorimeters; these alternate a dense absorbing material, which induces
760 showers, with an active layer which measures energy depositions by the induced
761 showers. Since some energy is deposited into the absorption layers as well, the energy
762 depositions must be properly calibrated for the detector.

Figure 5.7: The ATLAS calorimeter

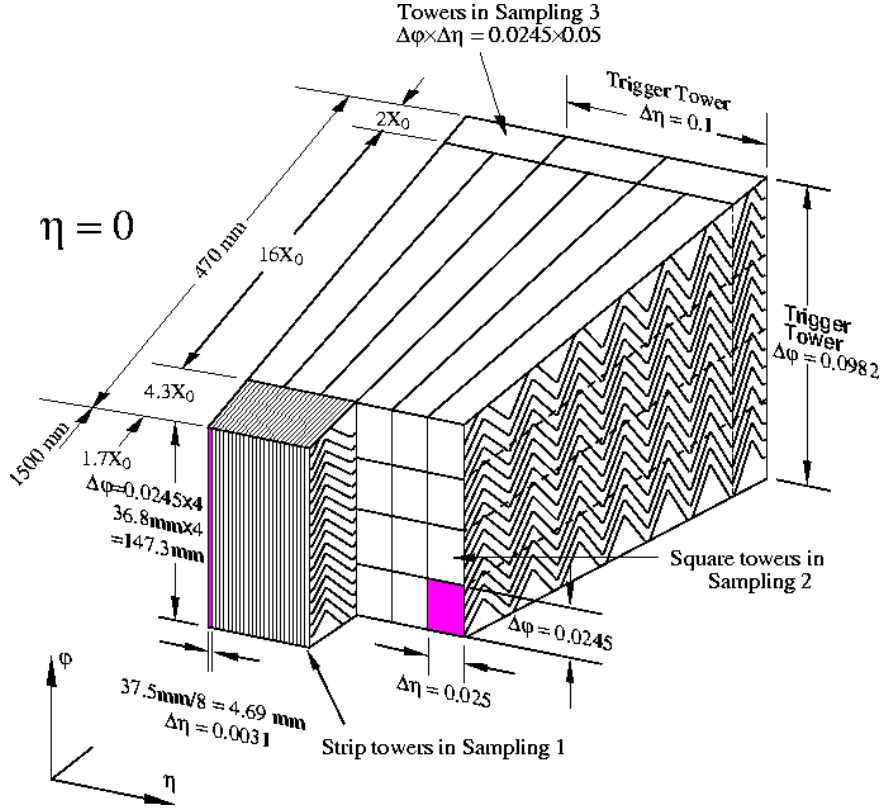


763 Electromagnetic objects (electrons and photons) and hadrons have much different
764 interaction properties, and thus we need different calorimeters to accurately measure
765 these different classes of objects; we can speak of the *electromagnetic* and *hadronic*
766 calorimeters. ATLAS contains four separate calorimeters : the liquid argon (LAr)
767 electromagnetic barrel calorimeter, the Tile barrel hadronic calorimeter, the LAr
768 endcap electromagnetic calorimeter, the LAr endcap hadronic calorimeter, and the
769 LAr Forward Calorimeter (FCal). Combined, these provide full coverage in ϕ up to
770 $|\eta| < 4.9$, and can be seen in Fig.5.7.

771 **Electromagnetic Calorimeters**

772 The electromagnetic calorimeters of the ATLAS detector consist of the barrel and
773 endcap LAr calorimeters. These are arranged into an ingenious “accordion” shape,
774 shown in 5.8, which allows full coverage in ϕ and exceptional coverage in η while
775 still allowing support structures for detector operation. The accordion is made of

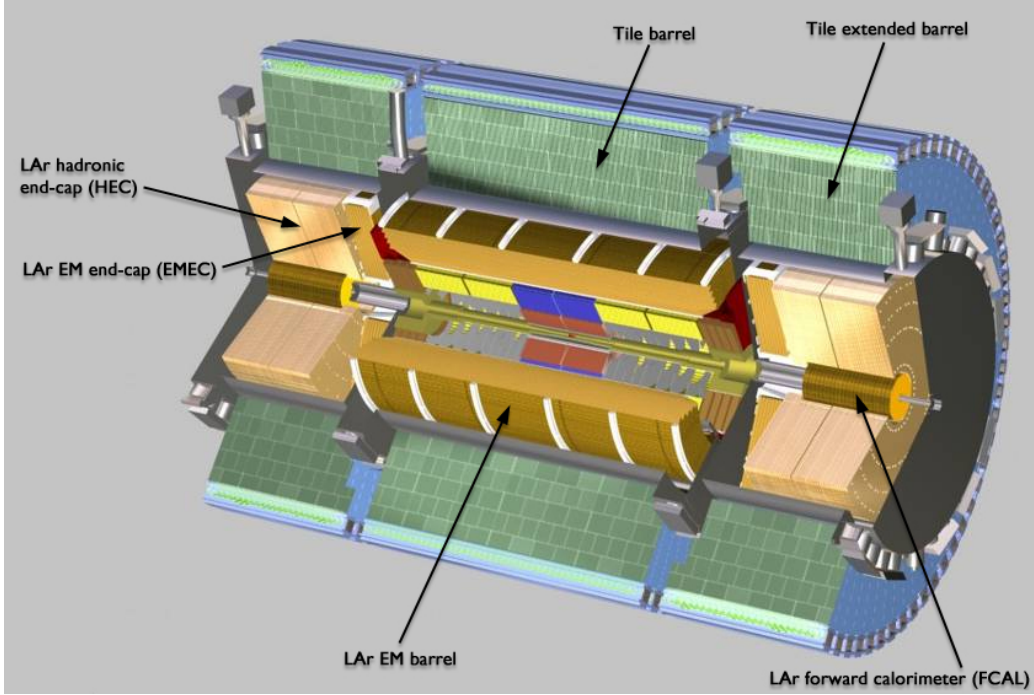
Figure 5.8: A schematic of a subsection of the barrel LAr electromagnetic calorimeter



776 layers with liquid argon (active detection material) and lead (absorber) to induce
 777 electromagnetic showers. The LAr EM calorimeters are each more than 20 radiation
 778 lengths deep, which provides the high stopping power necessary to properly measure
 779 the electromagnetic showers.

780 The barrel component of the LAr EM calorimeter extends from the center of the
 781 detector out to $|\eta| < 1.475$. The calorimeter has a presampler, which measures the
 782 energy of any EM shower induced before the calorimeter. This has segmentation of
 783 $\Delta\eta = 0.025, \Delta\phi = .01$. There are three “standard” layers in the barrel, which have
 784 decreasing segmentation into calorimeter *cells* as one travels radially outward from
 785 the interaction point. The first layer has segmentation of $\Delta\eta = 0.003, \Delta\phi = .1$, and
 786 is quite thin relative to the other layers at only 4 radiation lengths deep. It provides
 787 precise η and ϕ measurements for incoming EM objects. The second layer is the
 788 deepest at 16 radiation lengths, with a segmentation of $\Delta\eta = 0.025, \Delta\phi = 0.025$. It

Figure 5.9: A schematic of Tile hadronic calorimeter



is primarily responsible for stopping the incoming EM particles, which dictates its large relative thickness, and measures most of the energy of the incoming particles. The third layer is only 2 radiation lengths deep, with a rough segmentation of $\Delta\eta = 0.05$, $\Delta\phi = .025$. The deposition in this layer is primarily used to distinguish hadrons interacting electromagnetically and entering the hadronic calorimeter from the strictly EM objects which are stopped in the second layer.

The barrel EM calorimeter has a similar overall structure, but extends from $1.4 < |\eta| < 3.2$. The segmentation in η is better in the endcap than the barrel; the ϕ segmentation is the same. In total, the EM calorimeters contain about 190000 individual calorimeter cells.

Hadronic Calorimeters

The hadronic calorimetry of ATLAS sits directly outside the EM calorimetry. It contains three subdetectors : the barrel Tile calorimeter, the endcap LAr calorimeter,

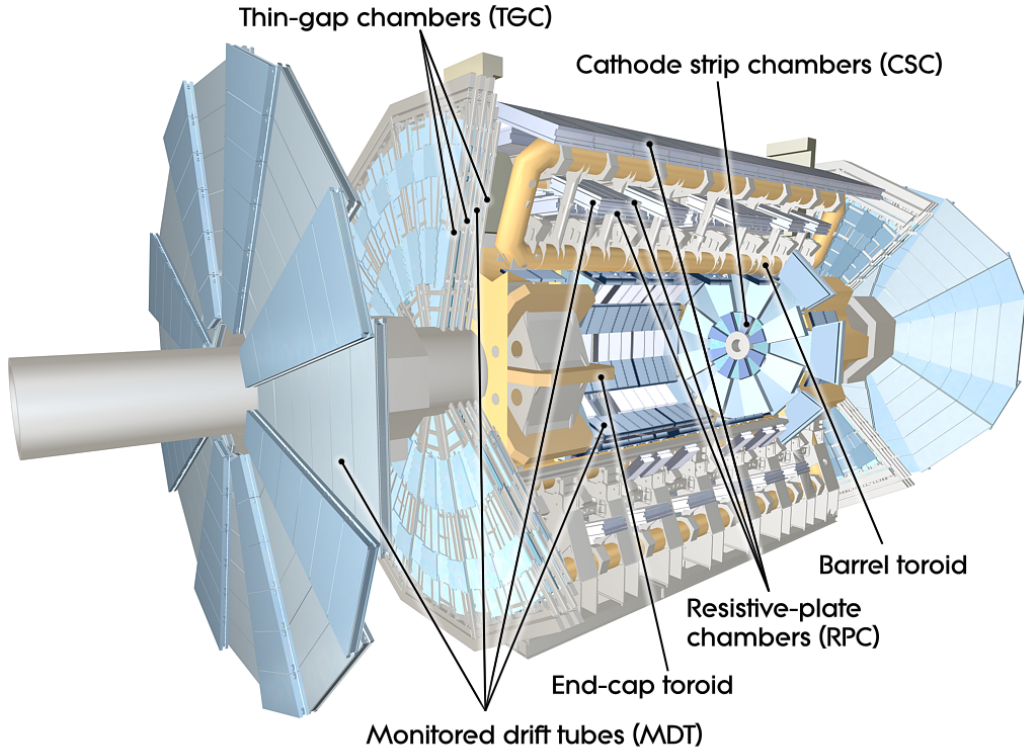
802 and the Forward LAr Calorimeter. Similar to the EM calorimeters, these are
803 sampling calorimeters that alternate steel (dense material) with an active layer
804 (plastic scintillator).

805 The barrel Tile calorimeter extends out to $|\eta| < 1.7$. There are again three layers,
806 which combined give about 10 interactions length of distance, which provides excellent
807 stopping power for hadrons. This is critical to avoid excess *punchthrough* to the muon
808 spectrometer beyond the hadronic calorimeters. The first layer has a depth of 1.5
809 interaction lengths. The second layer is again the thickest at a depth of 4.1 interaction
810 lengths; most of the energy of incoming particle is deposited here. Both the first and
811 second layer have segmentation of about $\Delta\eta = 0.1, \Delta\phi = 0.1$. Generally, one does not
812 need as fine of granularity in the hadronic calorimeter, since the energy depositions
813 in the hadronic calorimeters will be summed into the composite objects we know as
814 jets. The third layer has a thickness of 1.8 interaction lengths, with a segmentation of
815 $\Delta\eta = 0.2, \Delta\phi = 0.1$. The use of multiple layers allows one to understand the induced
816 hadronic shower as it propagates through the detector material.

817 The endcap LAr hadronic calorimeter covers the region $1.5 < |\eta| < 3.2$. It is
818 again a sampling calorimeter; the active material is LAr with a copper absorbed. It
819 does not use the accordion shape of the other calorimeters; it has a “standard” flat
820 shape perpendicular to the interaction point. The segmentation varies with η . For
821 $1.5 < |\eta| < 2.5$, the cells are $\Delta\eta = 0.1, \Delta\phi = 0.1$; in the region $2.5 < |\eta| < 3.2$, the
822 cells are $\Delta\eta = 0.2, \Delta\phi = 0.2$ in size.

823 The final calorimeter in ATLAS is the forward LAr calorimeter. Of those
824 subdetectors which are used for standard reconstruction techniques, the FCal sits
825 at the most extreme values of $3.1 < |\eta| < 4.9$. The FCal itself is made of three
826 subdetectors; FCal1 is actually an electromagnetic module, while FCal2 and FCal3
827 are hadronic. The absorber in FCal1 is copper, with a liquid argon active medium.
828 FCal2 and FCal3 also use a liquid argon active medium, with a tungsten absorber.

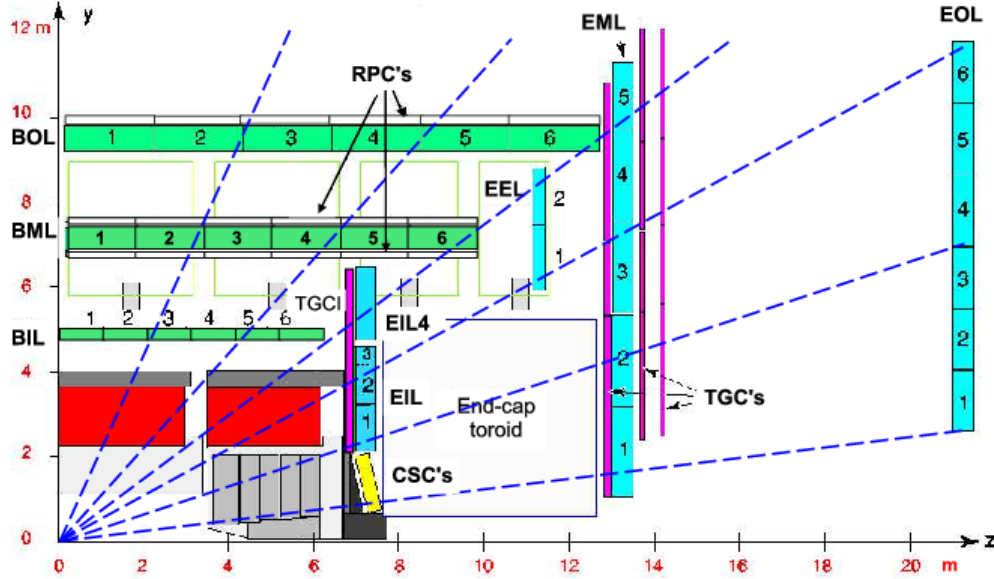
Figure 5.10: The ATLAS muon spectrometer



829 5.4 Muon Spectrometer

830 The muon spectrometer is the final major subdetector of the ATLAS detector.
831 The muon spectrometer sits outside the hadronic calorimetry, with pseudorapidity
832 coverage out to $|\eta| < 2.7$. The MS is a huge detector, with some detector elements
833 existing as far as 11 m in radius from the interaction point. This system is used
834 almost exclusively to measure the momenta of muons; these are the only measured
835 SM particles which consistently exit the hadronic calorimeters. These systems provide
836 a rough measurement, which is used in triggering (described in Ch.5.5), and a precise
837 measurement to be used in offline event reconstruction as described in Ch.???. The
838 MS produces tracks in a similar way to the ID; the hits in each subdetector are
839 recorded and then tracks are produced from these hits. Muon spectrometer tracks are
840 largely independent of the ID tracks due to the independent solenoidal and toroidal
841 magnet systems used in the ID and MS respectively. The MS consists of four separate

Figure 5.11: A schematic in z/η showing the location of the subdetectors of the muon spectrometer

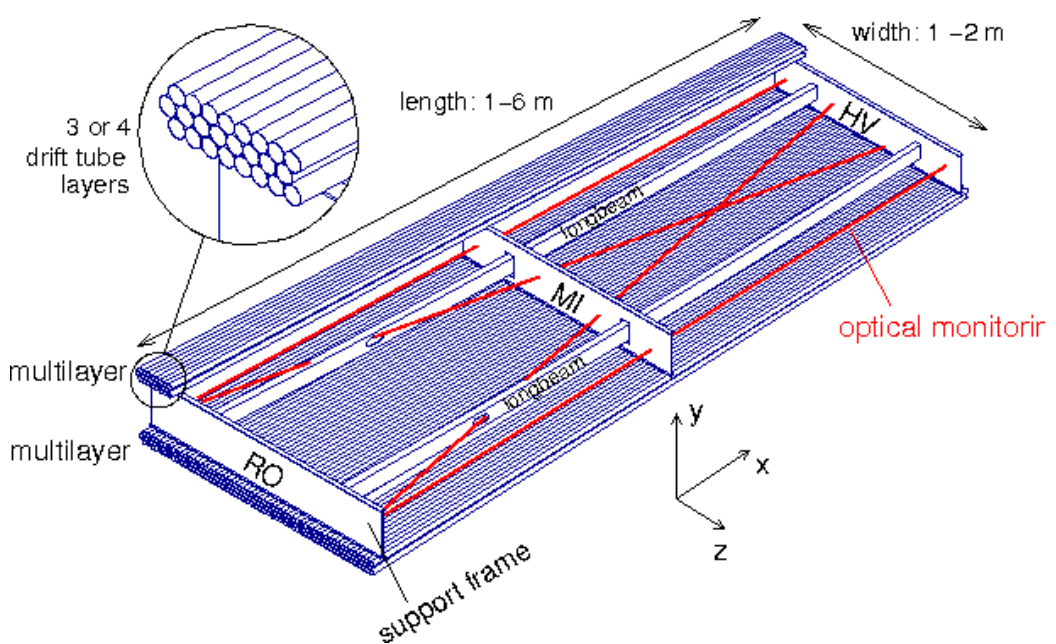


842 subdetectors: the barrel region is covered by the Resistive Plate Chambers (RPCs)
 843 and Monitored Drift Tubes (MDTs) while the endcaps are covered by MDTs, Thin
 844 Gap Chambers (TGCs), and Cathode Strip Chambers (CSCs).

845 Monitored Drift Tubes

846 The MDT system is the largest individual subdetector of the MS. MDTs provide
 847 precision measurements of muon momenta as well as fast measurements used for
 848 triggers. There are 1088 MDT chambers providing coverage out to pseudorapidity
 849 $|\eta| < 2.7$; each consists of an aluminum tube containing an argon- CO_2 gas mixture.
 850 In the center of each tube there $50\mu\text{m}$ diameter tungsten-rhenium wire at a voltage of
 851 3080 V. A muon entering the tube will induce ionization in the gas, which will “drift”
 852 towards the wire due to the voltage. One measures this ionization as a current in the
 853 wire; this current comes with a time measurement related to how long it takes the
 854 ionization to drift to the wire.

Figure 5.12: Schematic of a Muon Drift Tube chamber



855 These tubes are layered in a pattern shown in Fig.5.12. Combining the measure-
856 ments from the tubes in each layer gives good position resolution. The system consists
857 of three subsystems of these layers, at 5 m, 7m, and 9 m from the interaction point.
858 The innermost layer is directly outside the hadronic calorimeter. The combination of
859 these three measurements gives precise momenta measurements for muons.

860 Resistive Plate Chambers

861 The RPC system is alternated with the MDT system in the barrel; the first two layers
862 of RPC detectors surround the second MDT layer while the third is outside the final
863 MDT layer. The RPC system covers pseudorapidity $|\eta| < 1.05$. Each RPC consists
864 of two parallel plates at a distance of 2 mm surrounding a $\text{C}_2\text{H}_2\text{F}_4$ mixture. The
865 electric field between these plates is 4.9k kV/mm. Just as in the MDTs, an incoming
866 muon ionizes the gas, and the deposited ionization is collected by the detector (in this
867 case on the plates). It is quite fast, but with a relatively poor spatial resolution of
868 1 cm. Still, it can provide reasonable ϕ resolution due to its large distance from the
869 interaction point. This is most useful in triggering, where the timing requirements are
870 quite severe. The RPCs are also complement the MDTs by providing a measurement
871 of the non-bending coordinate.

872 Cathode Strip Chambers

873 The CSCs are used in place of MDTs in the first layer of the endcaps. This region, at
874 $2.0 < |\eta| < 2.7$, has higher particle multiplicity at the close distance to the interaction
875 point from low-energy photons and neutrons. The MDTs were not equip to deal with
876 the higher particle rate of this region, so the CSCs were designed to deal with this
877 deficiency.

878 Each CSC consists multiwire proportional chambers, oriented radially outward
879 from the interaction point. These chambers overlap partially in ϕ . The wires contain

Figure 5.13: Photo of the installation of Cathode Strip Chambers and Monitored Drift Tubes



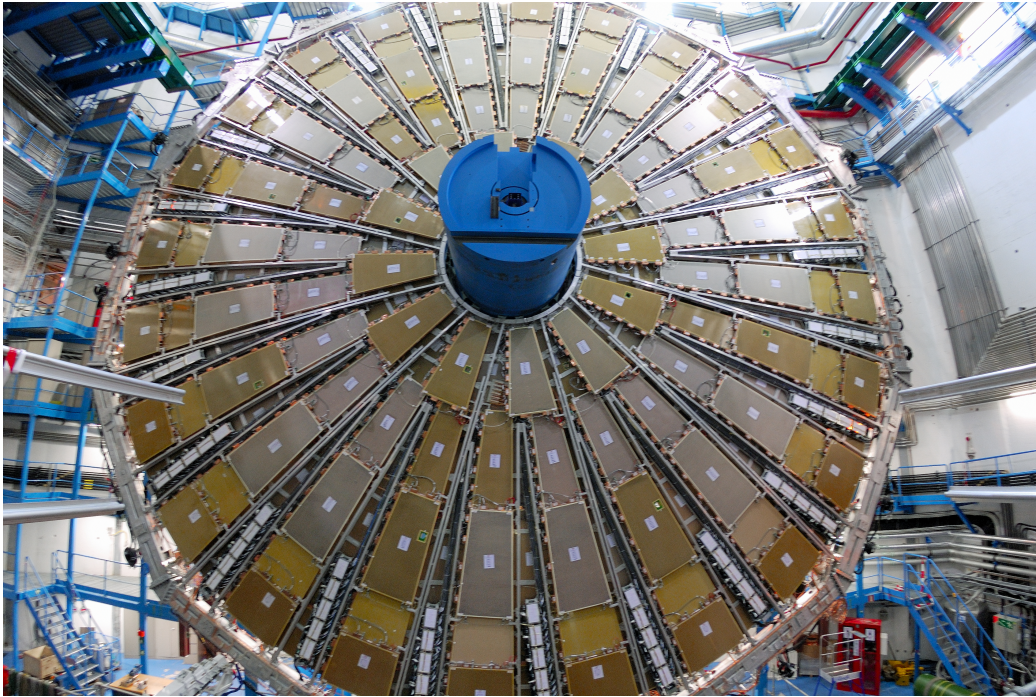
880 a gas mixture of argon and CO₂, which is ionized when muons enter. The detectors
881 operate with a voltage of 1900 V, with much lower drift times than the MDTs. They
882 provide less hits than MDTs, but their lower drift times lower uptime and reduce the
883 amount of detector overload.

884 The CSCs are arranged into four planes on the wheels of the muon spectrometer,
885 as seen in Fig.???. There are 32 CSCs in total, with 16 on each side of the detector
886 in η .

887 **Thin Gap Chambers**

888 The TGCs serve the purpose of the RPCs in the endcap at pseudorapidity of $1.05 <$
889 $|\eta| < 2.4$; they provide fast measurements used in triggering. The TGCs are also
890 multiwire proportional chambers a la the CSCs. The fast readouts necessary for
891 trigger are provided by a high electric field and a small wire-to-wire distance of 1.8
892 mm. These detectors provide both η and ϕ information, allowing the trigger to use
893 as much information as possible when selecting events.

Figure 5.14: Photo of a muon Big Wheel, consisting of Thin Gap Chambers



894 5.5 Trigger System

895 The data rate delivered by the LHC is staggering [89]. In the 2016 dataset, the
896 collision rate was 40 MHz, meaning a *bunch spacing* of 25 ns. In each of the event,
897 as we saw in Ch.??, there are many proton-proton collisions. Most of the collisions
898 are uninteresting, such as elastic scattering of protons, or even inelastic scattering
899 leading to low-energy dijet events. These types of events have been studied in detail
900 in previous experiments.

901 Even if one is genuinely interested in these events, it's *impossible* to save all of
902 the information available in each event. If all events were written "to tape" (as the
903 jargon goes), ATLAS would store terabytes of data per second. We are limited to only
904 about 1000 Hz readout by computing processing time and storage space. We thus
905 implement a *trigger* which provides fast inspection of events to drastically reduce
906 the data rate from the 40 MHz provided by the LHC to the 1000 Hz we can write to
907 tape for further analysis.

908 The ATLAS trigger system consists of a two-level trigger, known as the Level-
909 1 trigger (L1 trigger) and the High-Level Trigger (HLT)⁴. Trigger selections are
910 organized into *trigger chains*, where events passing a particular L1 trigger are passed
911 to a corresponding HLT trigger. For example, one would require a particular high- p_T
912 muon at L1, with additional quality requirements at HLT. One can also use HLT
913 triggers as prerequisites for each other, as is done in some triggers requiring both jets
914 and E_T^{miss} .

915 **Level-1 Trigger**

916 The L1 trigger is hardware-based, and provides the very fast rejection needed to
917 quickly select events of interest. The L1 trigger uses only what is known as *prompt*
918 data to quickly identify interesting events. Only the calorimeters and the triggering
919 detectors (RPCs and TGCs) of the MS are fast enough to be considered at L1,
920 since the tracking reconstruction algorithms used by the ID and the more precise
921 MS detectors are very slow. This allows quick identification of events with the
922 most interesting physical objects : large missing transverse momentum and high-
923 p_T electrons, muons, and jets.

924 L1 trigger processing is done locally. This means that events are selected without
925 considering the entire available event. Energy deposits over some threshold are
926 reconstructed as *regions of interest*. These RoIs are then compared using pattern
927 recognition hardware to “expected” patterns for the given RoIs. Events with RoIs
928 matching these expected patterns are then handed to the HLT through the Central
929 Trigger Processor. This step alone lowers the data rate down by about three orders
930 of magnitude.

⁴In Run1, ATLAS ran with a three-level trigger system. The L1 was essentially as today; the HLT consisted of two separate systems known as the L2 trigger and the Event Filter (EF). This was changed to the simpler system used today during the shutdown between Run1 and Run2.

931 **High-Level Trigger**

932 The HLT performs the next step, taking the incoming data rate from the L1 trigger
933 of ~ 75 kHz down to the ~ 1 kHz that can be written to tape. The HLT really
934 performs much like a simplified offline reconstruction, using many common quality
935 and analysis cuts to eliminate uninteresting events. This is done by using computing
936 farms located close to the detector, which process events in parallel. Individually, each
937 event which enters the computing farms takes about 4 seconds to reconstruct; the
938 HLT reconstruction time also has a long tail, which necessitates careful monitoring
939 of the HLT to ensure smooth operation.

940 HLT triggers are targetted to a particular physics process, such as a E_T^{miss} trigger,
941 single muon trigger, or multijet trigger. The collection of all triggers is known as
942 the trigger *menu*. Since many low-energy particles are produced in collisions, it is
943 necessary to set a *trigger threshold* on the object of interest; this is really just a fancy
944 naming for a trigger p_T cut. Due to the changing luminosity conditions of the LHC,
945 these thresholds change constantly, mostly by increasing thresholds with increasing
946 instantaneous luminosity. This allows an approximately constant number of events to be
947 written for further analysis. Triggers which have rates higher than those designated
948 by the menu are *prescaled*. This means writing only some fraction of the triggered
949 events. Of course, for physics analyses, one wishes to investigate all data events
950 passing some set of analysis cuts, so often one uses the “lowest threshold unprescaled
951 trigger”. *Turn-on curves* allow one to select the needed offline analysis cut to ensure
952 the trigger is fully efficient. An example turn-on curve for the E_T^{miss} triggers used in
953 the signal region of this analysis is shown in ??.

954 The full set of the lowest threshold unprescaled triggers considered here can be
955 found in Table 5.1. These are the lowest unprescaled triggers associated to the SUSY
956 signal models and Standard Model backgrounds considered in this thesis. More
957 information can be found in [89].

Table 5.1: High-Level Triggers used in this thesis. Descriptions of loose, medium, tight, and isolated can be found in [89]. The d_0 cut refers to a quality cut on the vertex position; this was removed from many triggers in 2016 to increase sensitivity to displaced vertex signals. For most triggers, the increased thresholds in 2016 compared to 2015 were designed to keep the rate approximately equal. The exception is the E_T^{miss} triggers; see 5.5.

Physics Object	Trigger	p_T (GeV)	Threshold	Level-1 Seed	Additional Requirements	Approximate Rate (Hz)
2015 Data						
E_T^{miss}	HLT_xe70	70		L1_XE50	-	60
	HLT_mu24_iloose_L1 M145			L1_MU15	isolated, loose	130
Muon	HLT_mu50	50		L1_MU15	-	30
Muon	HLT_e24_1hmedium_l1 B4se_L1EM20VH			L1_EM20VH	medium OR isolated, loose	140
Electron	HLT_e60_1hmedium	60		L1_EM20VH	medium	10
Electron	HLT_e120_1hloose	120		L1_EM20VH	loose	<10
Electron	HLT_g120_loose	120		L1_EM20VH	loose	20
2016 Data						
E_T^{miss}	HLT_xe100_mht_L1 XE500			L1_XE50	-	180
	HLT_mu24_ivarmedium 4			L1_MU20	medium	120
Muon	HLT_mu50	50		L1_MU20	-	40
Muon	HLT_e24_l1tight_no d4ivarloose			L1_EM22VHT	tight with no d_0 or loose	110
Electron	HLT_e60_1hmedium_no d0			L1_EM22VHT	medium with no d_0	10
Electron	HLT_e140_1hloose_no d0			L1_EM22VHT	loose with no d_0	<10
Electron	HLT_g140_loose	140		L1_EM22VHT	loose	20

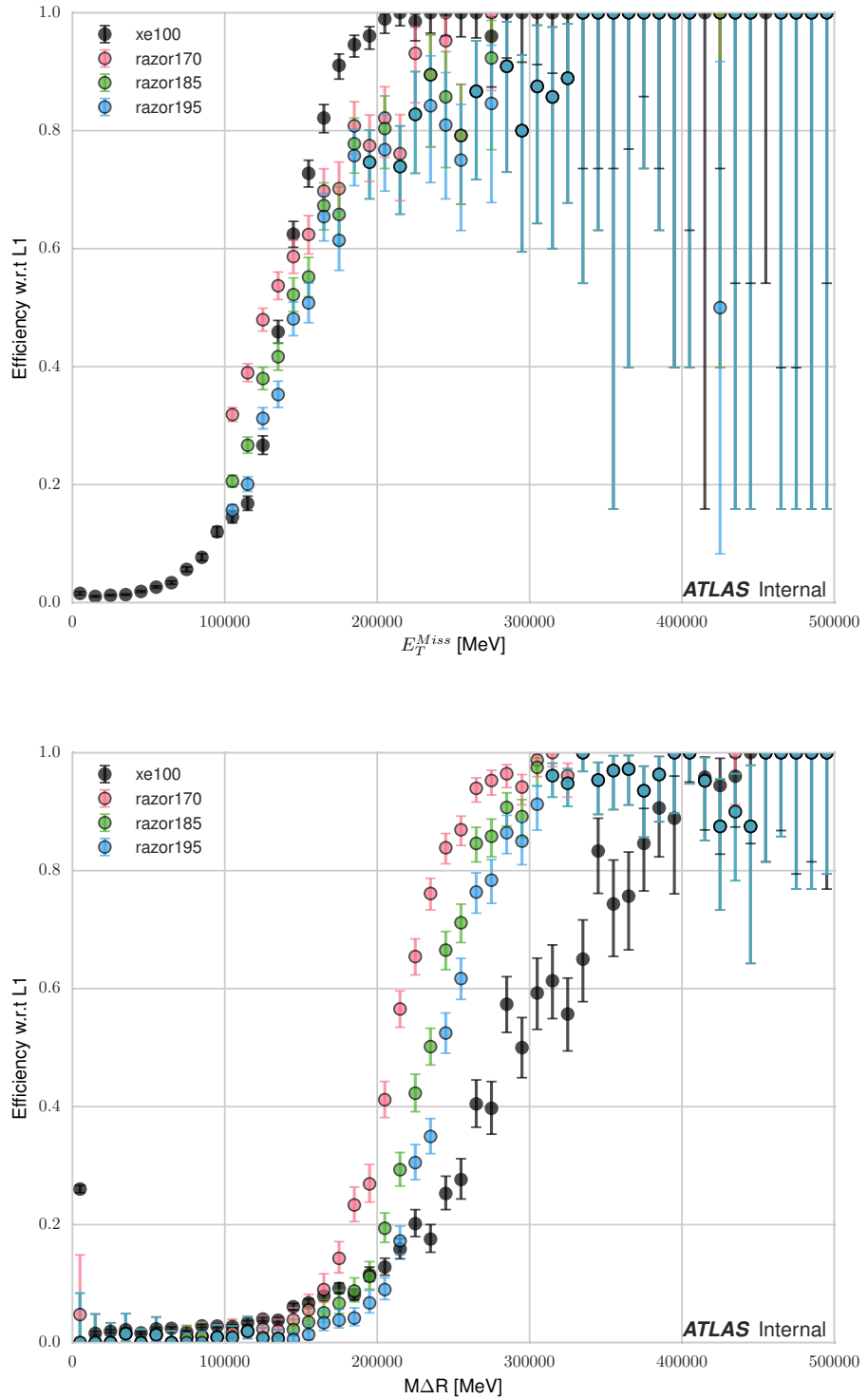
958 **Razor Triggers**

959 For the analysis presented in this thesis, the *razor triggers* were developed. These are
960 topological triggers, combining both jet and E_T^{miss} information to select interesting
961 events. In particular, they use the razor variable M_{Δ}^R which will be described in
962 Chapter ??.

963 Based on 2015 run conditions, these triggers would have allowed the use of a lower
964 offline E_T^{miss} cut with a similar rate to the nominal E_T^{miss} triggers. This can be seen
965 in the turn-on curves shown in Figure 5.15. The razor triggers are fully efficient at
966 nearly 100 GeV lower than the corresponding E_T^{miss} triggers in M_{Δ}^R .

967 There was a quite big change in the 2016 menu, which increased the rate given to
968 E_T^{miss} triggers drastically. This can be seen in the difference in rate shown between
969 E_T^{miss} triggers in 2015 and 2016 in Table 5.1. This allowed the E_T^{miss} triggers to
970 maintain a lower threshold throughout the dataset used in this thesis.

Figure 5.15: Turn-on curves for the razor triggers and nominal E_T^{miss} trigger. The razor triggers show a much sharper turn-on in M_{Δ}^R relative to the E_T^{miss} trigger. The converse is true for the E_T^{miss} triggers.



971

Chapter 6

972

Event Reconstruction

973 This chapter describes the reconstruction algorithms used within ATLAS. We will
974 make the distinction between the “primitive” objects which are reconstructed from
975 the detector signals from the “composite” physics objects we use in measurements
976 and searches for new physics.

cite fermilab
lectures

977 6.1 Primitive Object Reconstruction

978 The primitive objects reconstructed by ATLAS are *tracks* and (calorimeter) *clusters*.
979 These are reconstructed directly from tracking hits and calorimeter energy deposits
980 into cells. Tracks can be further divided into inner detector and muon spectrom-
981 eter tracks. Calorimeter clusters can be divided into sliding-window clusters and
982 topological clusters (topoclusters).

983 Inner Detector Tracks

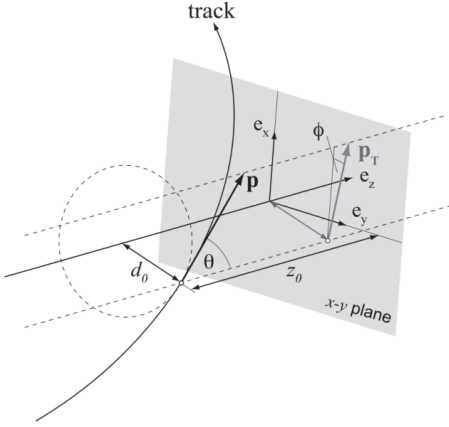
984

985 Inner detector tracks are reconstructed from hits in the inner detector. These hits
986 indicate that a charged particle has passed through the detector material. Due to the
987 2 T solenoid in the inner detector, the hits associated with any individual particle will
988 be curved; this allows one to measure the momentum of the particle. In any given
989 event, there is upwards of , making it impossible to do any sort of combinatorics to
990 reconstruct tracks¹. There are two algorithms used by ATLAS track reconstruction,

cite pa-
per/note

number

Figure 6.1: The parameters associated to a track.



991 known as *inside-out* and *outside-in*.

992 ATLAS first employs the inside-out algorithm. First, one assumes the track begins
 993 at the interaction point. Moving out from the interaction point, one creates track
 994 seeds. Track seeds are proto-tracks constructed from three hits; these hits can be
 995 distributed as three pixel hits, two pixel hits and one SCT hit, or three SCT hits.

site

996 One extrapolates the track and uses a [combinatorial Kalman filter](#), which adds the
 997 rest of the pixel and SCT hits to the seeds. This is done seed by seed, so it avoids
 998 the combinatorial complexity involved with checking all hits with all seeds. At this
 999 point, the algorithm applies an additional filter to avoid ambiguities from nearby
 1000 tracks. The TRT hits are then added to the seeds in the same procedure; in this way,
 1001 all hits are associated to a track.

1002 The next step is to figure out the correct kinematics of the track. This is
 1003 done by applying a fitting algorithm which outputs the best-fit track parameters
 1004 by minimizing the track distance from hits, weighted by each hit's resolution. These
 1005 parameters are $(d_0, z_0, \eta, \phi, q/p)$ where d_0 (z_0) is the transverse (longitudinal) impact
 1006 parameter and q/p is the charge over the track momenta. This set of parameters
 1007 uniquely defines the trajectory of the charged particle associated to the track; an
 1008 illustration of a track with these parameters is shown in Fig.6.1.

1009 The other track reconstruction algorithm is the outside-in algorithm. As the name
1010 implies, in this case, we start from the outside of the inner detector, in the TRT, and
1011 extend the tracks in. One begins by seeding from TRT hits, and extending the track
1012 back towards the center of the detector. The same fitting procedure is used as in
1013 the inside-out algorithm to find the optimal track parameters. This algorithm is
1014 particularly important for finding tracks which originate from interactions with the
1015 detector material, especially the SCT. For tracks from primary vertices, this often
1016 finds the same tracks as the inside-out algorithm, providing an important check on
1017 the consistency of the tracking procedure.

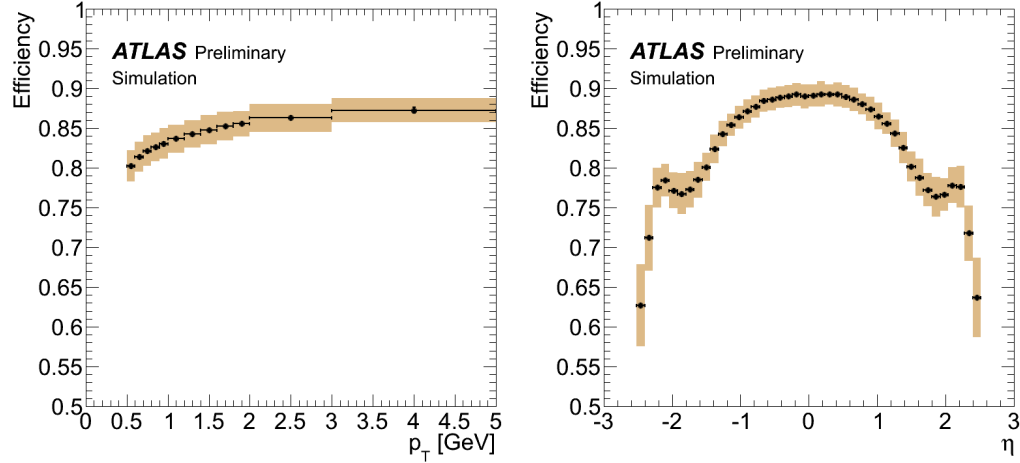
1018 In the high luminosity environment of the LHC, even the tracks reconstructed
1019 from precision detectors such as those of ATLAS inner detector can sometimes lead
1020 to fake tracks from simple combinatoric chance. Several quality checks are imposed
1021 after track fitting which reduce this background. Seven silicon (pixel + SCT) hits
1022 are required for all tracks. No more than two holes are allowed in the pixel detector;
1023 holes are expected measurements from the track that are missing in the pixel detector.
1024 Finally, tracks with poor fit quality, as measured by χ^2/ndf , are also rejected. Due
1025 to the high quality of the silicon measurements in the pixel detector and SCT, these
1026 requirements give good track reconstruction efficiency, as seen in Fig.6.2 for simulated
1027 events[[ATL-COM-PHYS-2012-1541](#)].

1028 Sliding-window clusters

1029 The sliding-window algorithm is a way to combine calorimeter cells into composite
1030 objects (clusters) to be used as inputs for other algorithms[[90](#)]. Sliding-window
1031 clusters are the primary inputs to electron and photon reconstruction, as described
1032 below. As described in Ch.??, the electromagnetic calorimeter has high granularity,
1033 with a cell size of $(\eta, \phi) = (.025, .025)$ in the coarsest second layer throughout most
1034 of the calorimeter. The “window” consists of 3 by 5 cells in the (η, ϕ) space; all

Figure 6.2: Track reconstruction efficiency as a function of track p_T and η . The efficiency is defined as the number of reconstructed tracks divided by the number of generate charged particles.

(a) Track reconstruction as a function of p_T . (b) Track reconstruction as a function of η .



1035 layers are added on this same 2D space. One translates this window over the space
 1036 and seeds a cluster whenever the energy sum of the cells is maximized. If the seed
 1037 energy is greater than 2.5 GeV, this seed is called a sliding-window cluster. This
 1038 choice was motivated to optimize the reconstruction efficiency of proto-electrons and
 1039 proto-photons while rejecting fakes from electronic noise and additional particles from
 1040 pileup vertices.

1041 Topological clusters

1042 Topoclusters are the output of the algorithm used within ATLAS to combine
 1043 hadronic and electromagnetic calorimeter cells in a way which extracts signal from
 1044 a background of significant electronic noise[91]. They are the primary input to the
 1045 algorithms which reconstruct jets.

1046 Topological clusters are reconstructed from calorimeter cells in the following way.
 1047 First, one maps all cells onto a single $\eta - \phi$ plane so one can speak of *neighboring*
 1048 cells. Two cells are considered neighboring if they are in the same layer and directly

1049 adjacent, or if they are in adjacent layers and overlap in $\eta - \phi$ space. The *significance*
1050 ξ_{cell} of a cell during a given event is

$$\xi_{\text{cell}} = \frac{E_{\text{cell}}}{\sigma_{\text{noise},\text{cell}}} \quad (6.1)$$

1051 where $\sigma_{\text{noise},\text{cell}}$ is measured for each cell in ATLAS and E_{cell} measures the current
1052 energy level of the cell. One thinks of this as the measurement of the energy *over*
1053 *threshold* for the cell.

1054 Topocluster *seeds* are defined as calorimeter cells which have a significance $\xi_{\text{cell}} >$
1055 4. These are the inputs to the algorithm; one iteratively tests all cells adjacent to these
1056 seeds for $\xi_{\text{cell}} > 2$. Each cells passing this selection is then added to the topocluster,
1057 and the procedure is repeated. When the algorithm reaches the point where there
1058 are no additional adjacent cells with $\xi_{\text{cell}} > 2$, every positive-energy cell adjacent to
1059 the current proto-cluster is added. This collection of cells is summed; the summed
1060 object is known as a topocluster. An example of this procedure for a simulation dijet
1061 event is shown in Fig.6.3.

1062 Muon Spectrometer Tracks

1063 Muon spectrometer tracks are fit using the same algorithms as the ID tracks, but
1064 different subdetectors. The tracks are seeded by hits in the MDTs or CSCs. After
1065 seeding in the MDTs and CSCs, the hits from all subsystems are refit as the final
1066 MS track. These tracks are used as inputs to the muon reconstruction, as we will see
1067 below.

Figure 6.3: Example of topoclustering on a simulated dijet event.

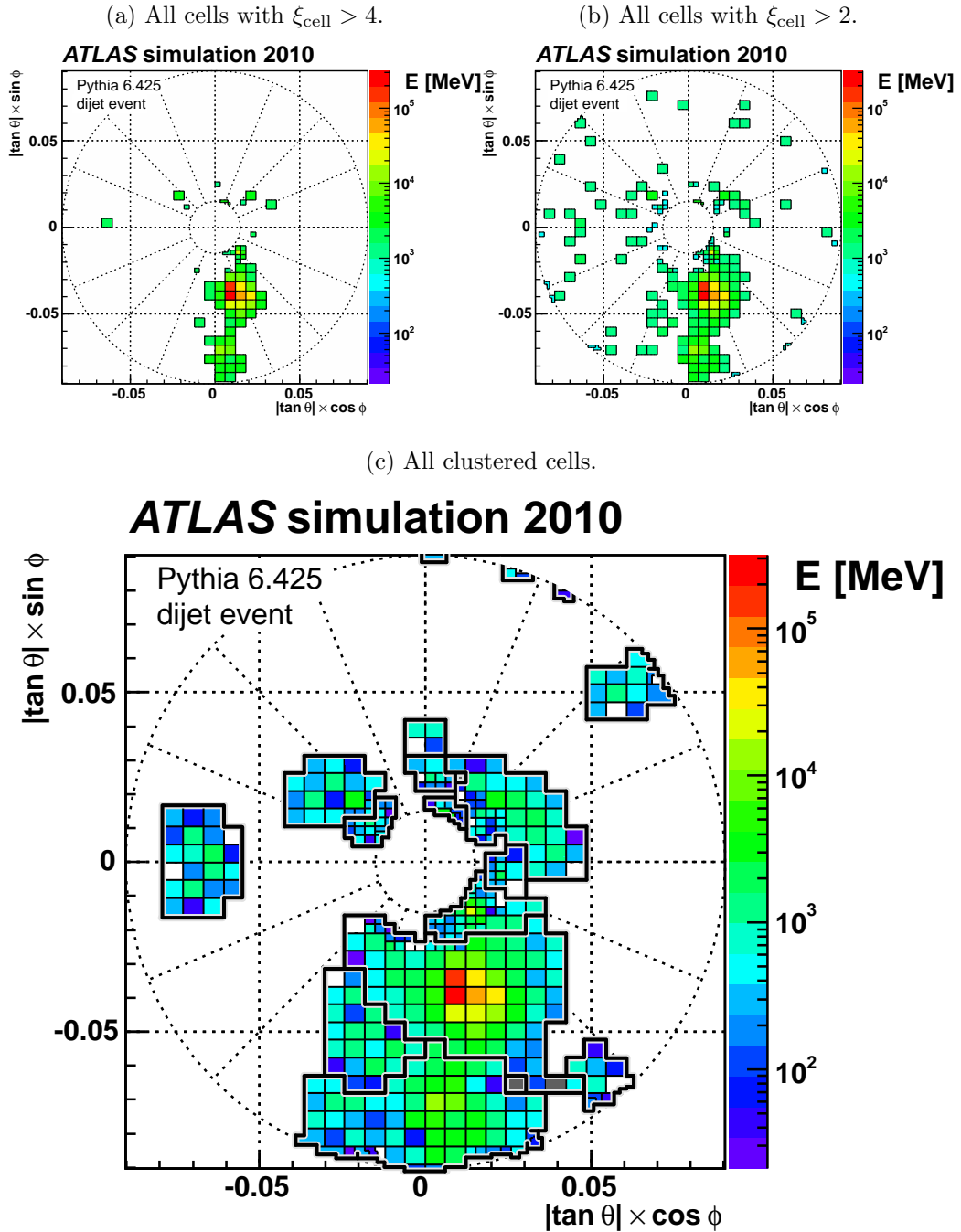
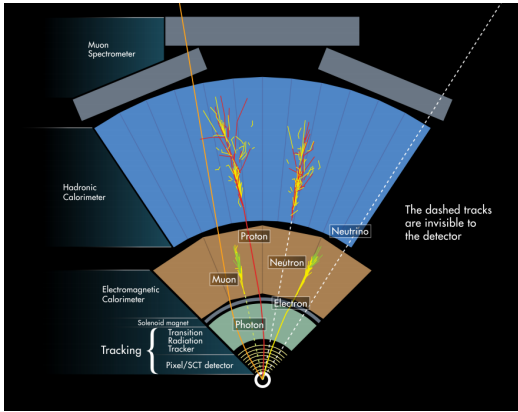


Figure 6.4: The interactions of particles with the ATLAS detector. Solid lines indicate the particle is interacting with the detector, while dashed lines are shown where the particle does not interact.



1068 **6.2 Physics Object Reconstruction and Quality**
 1069 **Identification**

1070 There are essentially six objects used in ATLAS searches for new physics: electrons,
 1071 photons, muons, τ -jets, jets, and E_T^{miss} . The reconstruction of these objects is
 1072 described here; in this thesis, τ lepton jets are not treated differently from other
 1073 hadronic jets. A very convenient summary plot is shown in Fig.6.4. This process
 1074 produces candidate objects, which are then identified by quality.

1075 One often wishes to understand “how certain” we are that a particular object
 1076 is truly the underlying physics object. In ATLAS, we often generically consider, in
 1077 order, *very loose*, *loose*, *medium*, and *tight* objects². These are ordered in terms of
 1078 decreasing object efficiency, or equivalently, decreasing numbers of fake objects. We
 1079 will also describe briefly the classification of objects into these categories.

1080 In this thesis, we present a search for new physics in a zero lepton final state; we
 1081 will provide additional details about jet and E_T^{miss} reconstruction.

² These are not all used for all objects, but it’s conceptually useful to think of these different categories.

1082 **Electrons and Photons**

1083 **Reconstruction**

1084 The reconstruction of electrons and photons (often for brevity called “electromagnetic
1085 objects”) is very similar [PERF-2013-03 , 92, 93]. This is because the reconstruction
1086 begins with the energy deposit in the calorimeter in the form of an electromagnetic
1087 shower. For any incoming e/γ , this induces many more electrons and photons in the
1088 shower; the measurement in the calorimeter is similar for these two objects.

1089 One thus begins the reconstruction of electromagnetic objects from the sliding-
1090 window clusters reconstructed from the EM calorimeter, as described in Sec.6.1.
1091 These $E > 2.5$ GeV clusters the the primary seed for electrons and photons. One
check delta1092
R defined 1093
somewhere1094
then looks for all ID tracks within $\Delta R < 0.3$. We “match” the track and cluster if
they are within $\Delta\phi < 0.2$ in the direction of track curvature, or $\Delta\phi < 0.05$ in the
direction opposite the track curvature. Those track-cluster seeds with tracks pointing
to the primary vertex are reconstructed as electrons.
1095

1096 For photons, we have two options to consider, known as *converted* and *unconverted*
1097 photons. Due to the high energy of the LHC collisions, typical photons have energy
1098 ~ 1 GeV; at this scale, photons interact almost exclusively via pair-production in the
DIAGRAM1099 presence of the detector material . If the track-cluster seed has a track which does
1100 not point at the primary vertex, we reconstruct this object as a converted photon.
1101 This happens since the photon travels a distance before decay into two electrons, and
1102 see the tracks coming from this secondary vertex. Those clusters which do not have
1103 any associated tracks are then reconstruced as an unconverted photon.

1104 The final step in electromagnetic object reconstruction is the final energy value
1105 assigned to these objects; this process is different between electrons and photons due
1106 to their differing signatures in the EM calorimeter. In the barrel, electrons energies
1107 are assigned as the sum of the 3 clusters in η and 7 clusters in ϕ to account for the

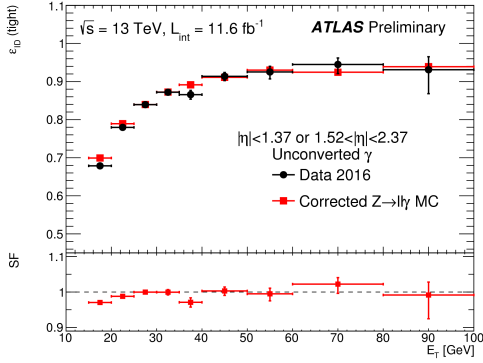
1108 electron curving in the ϕ direction. Barrel photons are assigned the energy sum of
1109 (3, 5) clusters in (η, ϕ) space. In the endcap, the effect of the magnetic field on the
1110 electrons is smaller, and there is a coarser granularity. Both objects sum the (5, 5)
1111 clusters for their final energy value.

1112 Quality Identification

1113 Electrons have a number of important backgrounds which can give fakes. Fake
1114 electrons come primarily from secondary vertices in hadron decays or misidentified
1115 hadronic jets. To reduce these backgrounds, quality requirements are imposed on
1116 electron candidates. Loose electrons have requirements imposed on the shower
1117 shapes in the electromagnetic calorimeter and on the quality of the associated ID
1118 track. There is also a requirement that there is a small energy deposition in the
1119 hadronic calorimeter behind the electron, to avoid jets being misidentified as electrons
1120 (low hadronic leakage). Medium and tight electrons have increasingly stronger
1121 requirements on these variables, and additional requirements on the isolation (as
1122 measured by ΔR) and matching of the ID track momentum and the calorimeter
1123 energy deposit.

1124 Photons are relatively straightforward to measure, since there are few background
1125 processes[**ATL-PHYS-PUB-2016-015**]. The primary one is pion decays to two
1126 photons, which can cause a jet to be misidentified as photon. Loose photons have
1127 requirements on the shower shape and hadronic leakage. Tight photons have tighter
1128 shower shape cuts, especially on the high granularity first layer of the EM calorimeter.
1129 The efficiency for unconverted tight photons as a function of p_T is shown in

Figure 6.5: Unconverted photon efficiency as measured in [ATL-PHYS-PUB-2016-015].



1130 Muons

1131 Reconstruction

1132 Muons are reconstructed using measurements from all levels of the ATLAS detec-
 1133 tor[94]. They leave a ID track, a small, characteristic deposition in the EM calorime-
 1134 ter, and then a track in the muon spectrometer. The primary reconstruction technique
 1135 produces a so-called *combined* muon. “Combined” means using a combination of the
 1136 ID and MS tracks to produce the final reconstructed muon kinematics. This is done
 1137 by refitting the hits associated to both tracks, and using this refit track for the muon
 1138 kinematics. This process produces the best measured muons, although several other
 1139 worse algorithms are used when the full detector information is missing. An example
 1140 is in the region $2.5 < |\eta| < 2.7$ outside the ID acceptance; in this region, MS tracks
 1141 are used without the corresponding ID tracks.

1142 Quality Identification

Several additional criteria are used to assure muon measurements are free of significant background contributions, especially from pion and kaon decays to muons. Muons produced via these decay processes are often characterized by a “kink”. Candidate muons with a poor fit quality, characterized by $\chi^2/\text{n.d.f.}$, are thus rejected.

Additionally, the absolute difference in momentum measurements between the ID and MS provide another handle, since the other decay products from hadron decays carry away some amount of the initial hadron momentum. This is measured by

$$\rho' = \frac{|p_T^{\text{ID}} - p_T^{\text{MS}}|}{p_T^{\text{Combined}}}. \quad (6.2)$$

Additionally, there is a requirement on the q/p significance, defined as

$$S_{q/p} = \frac{|(q/p)^{\text{ID}} - (q/p)^{\text{MS}}|}{\sqrt{\sigma_{\text{ID}}^2 + \sigma_{\text{MS}}^2}}. \quad (6.3)$$

1143 The $\sigma_{\text{ID},\text{MS}}$ in the denominator of Eq.6.3 are the uncertainties on the corresponding
 1144 quantity from the numerator. Finally, cuts are placed on the number of hits in the
 1145 various detector elements.

1146 Subsequently tighter cuts on these variables allow one to define the different muon
 1147 identification criteria. Loose muons have the highest reconstruction efficiency, but
 1148 the highest number of fake muons, since there are no requirements on the number
 1149 of subdetector hits and the loosest requirements on the suite of quality variables.
 1150 Medium muons consist of Loose muons with tighter cuts on the quality variables;
 1151 they also require more than three MDT hits in at least two MDT layers. These are
 1152 the default used by ATLAS analyses. Tight muons have stronger cuts than those of
 1153 the medium selection, and reducing the reconstruction efficiency. The reconstruction
 1154 efficiency as a function of p_T can be seen for Medium muons in Fig.6.6.

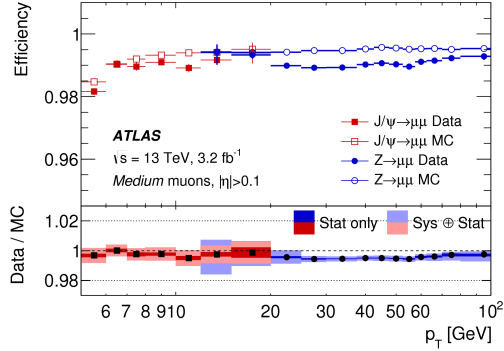
1155 Jets

1156

cite pa-
per/note

1157 Jets are composite objects corresponding to many physical particles. This is a
 1158 striking difference from the earlier particles. Fortunately, we normally (and in this
 1159 thesis) care about the original particle produced in primary collision. In the SM, this
 1160 corresponds to quarks and gluons; due to the hadronization process described in 2, free

Figure 6.6: Medium muon efficiency as measured in [94].



1161 quarks and gluons spontaneously hadronize and produce a hadronic shower, which
 1162 we call a jet. These showers can be measured by the EM and hadronic calorimeters,
 1163 and the charged portions can be measured in the ID. The first question is how to
 1164 combine these measurements into a composite object representing the underlying
 1165 physical parton. This is done via jet algorithms.

1166 Jet Algorithms

1167 It might seem straightforward to combine the underlying physical particles into a
 1168 jet. There are three important characteristics required for any jet reconstruction
 1169 algorithm to be used by ATLAS.

- 1170 • Collinear safety - if any particle with four-vector p is replaced by two particles
 1171 of p_1, p_2 with $p = p_1 + p_2$, the subsequent jet should not change
- 1172 • Radiative (infrared) safety - if any particle with four-vector p radiates a particle
 1173 of energy $\alpha \rightarrow 0$, the subsequent jet should not change
- 1174 • Fast - the jet algorithm should be “fast enough” to be useable by ATLAS
 1175 computing resources

1176 The first two requirements can be seen in terms of requirements on soft gluon emission.
 1177 Since partons emit arbitrarily soft gluons freely, one should expect the algorithms

1178 to not be affected by this emission. The final requirement is of course a practical
1179 limitation.

The algorithms in use by ATLAS (and CMS) which satisfies these requirements are collectively known as the k_T algorithms [95–97]. These algorithms iteratively combine the “closest” objects, defined using the following distance measures :

$$d_{ij} = \min(k_{T,i}^{2p}, k_{T,j}^{2p}) \frac{\Delta_{ij}^2}{R^2} \quad (6.4)$$
$$d_{iB} = k_{Ti}^{2p}$$

1180 In Eq.6.4, k_T , i is the transverse momentum of i -th jet *constituent*, Δ_{ij} is the angular
1181 distance between the constituents. Both R and p are adjustable parameters; R is
1182 known as the (jet) *cone size* and p regulates the power of the energy vs the geometrical
1183 scales. The algorithm sequence, for a given set of objects i with four-vector k :

- 1184 1. Find the minimum distance in the set of all d_{ij} and d_{iB} .
- 1185 2. If the distance is one of the d_{ij} , combine the input pair of object i, j and return
1186 to (1). If the distance is one of the d_{iB} , remove the object from the list, call it
1187 a jet, and return to (1).

1188 This process ends when all objects i have been added to a jet.

1189 Any choice of (p, R) has the requirements of collinear and radiative safety. In
1190 essence, the choice is then to optimize based on speed and the potential for new
1191 physics discoveries. In ATLAS, we make the choice of $p = -1$; this is also known as
1192 the *anti- k_T* algorithm. The choice of $R = 0.4$ is used for the distance parameter of
1193 the jets.

1194 The primary “nice” quality of this algorithm can be seen with the following
1195 example. Consider three inputs to an anti- k_T algorithm, all with $\eta = 0$:

- 1196 • Object 1 : $(p_T, \phi) = (30 \text{ GeV}, 0)$
- 1197 • Object 2 : $(p_T, \phi) = (20 \text{ GeV}, -0.2)$

1198 • Object 3 : $(p_T, \phi) = (10 \text{ GeV}, 0.2)$

1199 • Object 4 : $(p_T, \phi) = (1 \text{ GeV}, 0.5)$

1200 . In the case shown, it seems natural to first combine the “bigger” objects 1 and 2.
1201 These then pick up the extra small object 3, and object 4 is not included in the jet.
1202 This is exactly what is done by the anti- k_T algorithm. The (normal) k_T algorithm with
1203 $p = 1$ instead combines the smallest objects, 3 and 4, first. Object 1 and 2 combine
1204 to form their own jet, instead of these jets picking up object 3. This behavior is not
1205 ideal due to the effects of pileup.

1206 In ATLAS, jets are reconstructed using the calorimeter topoclusters using the
1207 anti- k_T algorithm with $R = 0.4$. The collection of all topoclusters reconstructed as in
1208 Sec.6.1, and used as the general object

1209 **Jet Reconstruction and Calibration**

1210 Jets are reconstructed from the

1211 **Jet Calibration**

1212 **B-jets**

1213 **Missing Transverse Momentum**

cite pa- 1214
per/notes

1215 **6.3 Maybe PFlow?**

1216

Chapter 7

1217

The Recursive Jigsaw Technique

1218 Here you can write some introductory remarks about your chapter. I like to give each
1219 sentence its own line.

1220 When you need a new paragraph, just skip an extra line.

1221 **7.1 Razor variables**

1222 By using the asterisk to start a new section, I keep the section from appearing in the
1223 table of contents. If you want your sections to be numbered and to appear in the
1224 table of contents, remove the asterisk.

1225 **7.2 SuperRazor variables**

1226 **7.3 The Recursive Jigsaw Technique**

1227 **7.4 Variables used in the search for zero lepton**

1228 **SUSY**

1229

Chapter 8

1230

Title of Chapter 1

1231

Chapter 9

1232

Title of Chapter 1

1233 Here you can write some introductory remarks about your chapter. I like to give each

1234 sentence its own line.

1235 When you need a new paragraph, just skip an extra line.

1236 **9.1 Object reconstruction**

1237 **Photons, Muons, and Electrons**

1238 **Jets**

1239 **Missing transverse momentum**

1240 Probably longer, show some plots from the PUB note that we worked on

₁₂₄₁ **9.2 Signal regions**

₁₂₄₂ **Gluino signal regions**

₁₂₄₃ **Squark signal regions**

₁₂₄₄ **Compressed signal regions**

₁₂₄₅ **9.3 Background estimation**

₁₂₄₆ **Z vv**

₁₂₄₇ **W ev**

₁₂₄₈ **ttbar**

Title of Chapter 1

1251 Here you can write some introductory remarks about your chapter. I like to give each
1252 sentence its own line.

1253 When you need a new paragraph, just skip an extra line.

1254 **10.1 Statistical Analysis**

1255 maybe to be moved to an appendix

1256 **10.2 Signal Region distributions**

1257 **10.3 Pull Plots**

1258 **10.4 Systematic Uncertainties**

1259 **10.5 Exclusion plots**

1260

Conclusion

1261 Here you can write some introductory remarks about your chapter. I like to give each
1262 sentence its own line.

1263 When you need a new paragraph, just skip an extra line.

1264 **10.6 New Section**

1265 By using the asterisk to start a new section, I keep the section from appearing in the
1266 table of contents. If you want your sections to be numbered and to appear in the
1267 table of contents, remove the asterisk.

Bibliography

- 1269 [1] O. Perdereau, *Planck 2015 cosmological results*,
1270 AIP Conf. Proc. **1743** (2016) p. 050014.
- 1271 [2] N. Aghanim et al.,
1272 *Planck 2016 intermediate results. LI. Features in the cosmic microwave*
1273 *background temperature power spectrum and shifts in cosmological parameters*
1274 (2016), arXiv: [1608.02487 \[astro-ph.CO\]](https://arxiv.org/abs/1608.02487).
- 1275 [3] J. S. Schwinger,
1276 *On Quantum electrodynamics and the magnetic moment of the electron*,
1277 Phys. Rev. **73** (1948) p. 416.
- 1278 [4] S. Laporta and E. Remiddi,
1279 *The Analytical value of the electron (g-2) at order alpha**3 in QED*,
1280 Phys. Lett. **B379** (1996) p. 283, arXiv: [hep-ph/9602417 \[hep-ph\]](https://arxiv.org/abs/hep-ph/9602417).
- 1281 [5] S. Schael et al., *Precision electroweak measurements on the Z resonance*,
1282 Phys. Rept. **427** (2006) p. 257, arXiv: [hep-ex/0509008 \[hep-ex\]](https://arxiv.org/abs/hep-ex/0509008).
- 1283 [6] S. L. Glashow, *Partial Symmetries of Weak Interactions*,
1284 Nucl. Phys. **22** (1961) p. 579.
- 1285 [7] S. Weinberg, *A Model of Leptons*, Phys. Rev. Lett. **19** (1967) p. 1264.
- 1286 [8] A. Salam, *Weak and Electromagnetic Interactions*,
1287 Conf. Proc. **C680519** (1968) p. 367.
- 1288 [9] M. Gell-Mann, *A Schematic Model of Baryons and Mesons*,
1289 Phys. Lett. **8** (1964) p. 214.
- 1290 [10] G. Zweig, “An SU(3) model for strong interaction symmetry and its breaking.
1291 Version 2,” *DEVELOPMENTS IN THE QUARK THEORY OF HADRONS*.
1292 VOL. 1. 1964 - 1978, ed. by D. Lichtenberg and S. P. Rosen, 1964 p. 22,
1293 URL: <http://inspirehep.net/record/4674/files/cern-th-412.pdf>.

- 1294 [11] S. Weinberg, *Implications of Dynamical Symmetry Breaking*,
 1295 Phys. Rev. **D13** (1976) p. 974.
- 1296 [12] S. Weinberg, *Implications of Dynamical Symmetry Breaking: An Addendum*,
 1297 Phys. Rev. **D19** (1979) p. 1277.
- 1298 [13] E. Gildener, *Gauge Symmetry Hierarchies*, Phys. Rev. **D14** (1976) p. 1667.
- 1299 [14] L. Susskind,
 1300 *Dynamics of Spontaneous Symmetry Breaking in the Weinberg-Salam Theory*,
 1301 Phys. Rev. **D20** (1979) p. 2619.
- 1302 [15] S. P. Martin, “A Supersymmetry Primer,” 1997,
 1303 eprint: [arXiv:hep-ph/9709356](https://arxiv.org/abs/hep-ph/9709356).
- 1304 [16] V. C. Rubin and W. K. Ford Jr., *Rotation of the Andromeda Nebula from a*
 1305 *Spectroscopic Survey of Emission Regions*, Astrophys. J. **159** (1970) p. 379.
- 1306 [17] M. S. Roberts and R. N. Whitehurst,
 1307 *“The rotation curve and geometry of M31 at large galactocentric distances*,
 1308 Astrophys. J. **201** (1970) p. 327.
- 1309 [18] V. C. Rubin, N. Thonnard, and W. K. Ford Jr.,
 1310 *Rotational properties of 21 SC galaxies with a large range of luminosities and*
 1311 *radii, from NGC 4605 /R = 4kpc/ to UGC 2885 /R = 122 kpc/*,
 1312 Astrophys. J. **238** (1980) p. 471.
- 1313 [19] V. C. Rubin et al., *Rotation velocities of 16 SA galaxies and a comparison of*
 1314 *Sa, Sb, and SC rotation properties*, Astrophys. J. **289** (1985) p. 81.
- 1315 [20] A. Bosma,
 1316 *21-cm line studies of spiral galaxies. 2. The distribution and kinematics of*
 1317 *neutral hydrogen in spiral galaxies of various morphological types.*,
 1318 Astron. J. **86** (1981) p. 1825.
- 1319 [21] M. Persic, P. Salucci, and F. Stel, *The Universal rotation curve of spiral*
 1320 *galaxies: 1. The Dark matter connection*,
 1321 Mon. Not. Roy. Astron. Soc. **281** (1996) p. 27,
 1322 arXiv: [astro-ph/9506004](https://arxiv.org/abs/astro-ph/9506004) [[astro-ph](#)].
- 1323 [22] M. Lisanti, “Lectures on Dark Matter Physics,” 2016,
 1324 eprint: [arXiv:1603.03797](https://arxiv.org/abs/1603.03797).
- 1325 [23] H. Miyazawa, *Baryon Number Changing Currents*,
 1326 Prog. Theor. Phys. **36** (1966) p. 1266.

- 1327 [24] J.-L. Gervais and B. Sakita, *Generalizations of dual models*,
 1328 Nucl. Phys. **B34** (1971) p. 477.
- 1329 [25] J.-L. Gervais and B. Sakita,
 1330 *Field Theory Interpretation of Supergauges in Dual Models*,
 1331 Nucl. Phys. **B34** (1971) p. 632.
- 1332 [26] Yu. A. Golfand and E. P. Likhtman, *Extension of the Algebra of Poincare
 1333 Group Generators and Violation of p Invariance*,
 1334 JETP Lett. **13** (1971) p. 323, [Pisma Zh. Eksp. Teor. Fiz. 13, 452 (1971)].
- 1335 [27] A. Neveu and J. H. Schwarz, *Factorizable dual model of pions*,
 1336 Nucl. Phys. **B31** (1971) p. 86.
- 1337 [28] A. Neveu and J. H. Schwarz, *Quark Model of Dual Pions*,
 1338 Phys. Rev. **D4** (1971) p. 1109.
- 1339 [29] D. V. Volkov and V. P. Akulov, *Is the Neutrino a Goldstone Particle?*
 1340 Phys. Lett. **B46** (1973) p. 109.
- 1341 [30] J. Wess and B. Zumino,
 1342 *A Lagrangian Model Invariant Under Supergauge Transformations*,
 1343 Phys. Lett. **B49** (1974) p. 52.
- 1344 [31] A. Salam and J. A. Strathdee, *Supersymmetry and Nonabelian Gauges*,
 1345 Phys. Lett. **B51** (1974) p. 353.
- 1346 [32] S. Ferrara, J. Wess, and B. Zumino, *Supergauge Multiplets and Superfields*,
 1347 Phys. Lett. **B51** (1974) p. 239.
- 1348 [33] J. Wess and B. Zumino, *Supergauge Transformations in Four-Dimensions*,
 1349 Nucl. Phys. **B70** (1974) p. 39.
- 1350 [34] J. D. Lykken, “Introduction to supersymmetry,” *Fields, strings and duality. Proceedings, Summer School, Theoretical Advanced Study Institute in Elementary Particle Physics, TASI’96, Boulder, USA, June 2-28, 1996*,
 1351 p. 85, arXiv: [hep-th/9612114 \[hep-th\]](https://arxiv.org/abs/hep-th/9612114),
 1352 URL: http://lss.fnal.gov/cgi-bin/find_paper.pl?pub-96-445-T.
- 1355 [35] A. Kobakhidze, “Intro to SUSY,” 2016, URL:
 1356 <https://indico.cern.ch/event/443176/page/5225-pre-susy-programme>.
- 1357 [36] G. R. Farrar and P. Fayet, *Phenomenology of the Production, Decay, and
 1358 Detection of New Hadronic States Associated with Supersymmetry*,
 1359 Phys. Lett. **B76** (1978) p. 575.

- 1360 [37] ATLAS Collaboration,
1361 *Search for the electroweak production of supersymmetric particles in*
1362 *$\sqrt{s} = 8 \text{ TeV}$ pp collisions with the ATLAS detector,*
1363 *Phys. Rev. D* **93** (2016) p. 052002, arXiv: [1509.07152 \[hep-ex\]](#).
- 1364 [38] ATLAS Collaboration, *Summary of the searches for squarks and gluinos using*
1365 *$\sqrt{s} = 8 \text{ TeV}$ pp collisions with the ATLAS experiment at the LHC,*
1366 *JHEP* **10** (2015) p. 054, arXiv: [1507.05525 \[hep-ex\]](#).
- 1367 [39] ATLAS Collaboration, *ATLAS Run 1 searches for direct pair production of*
1368 *third-generation squarks at the Large Hadron Collider,*
1369 *Eur. Phys. J. C* **75** (2015) p. 510, arXiv: [1506.08616 \[hep-ex\]](#).
- 1370 [40] CMS Collaboration,
1371 *Search for supersymmetry with razor variables in pp collisions at $\sqrt{s} = 7 \text{ TeV}$,*
1372 *Phys. Rev. D* **90** (2014) p. 112001, arXiv: [1405.3961 \[hep-ex\]](#).
- 1373 [41] CMS Collaboration, *Inclusive search for supersymmetry using razor variables*
1374 *in pp collisions at $\sqrt{s} = 7 \text{ TeV}$, Phys. Rev. Lett.* **111** (2013) p. 081802,
1375 arXiv: [1212.6961 \[hep-ex\]](#).
- 1376 [42] CMS Collaboration, *Search for Supersymmetry in pp Collisions at 7 TeV in*
1377 *Events with Jets and Missing Transverse Energy,*
1378 *Phys. Lett. B* **698** (2011) p. 196, arXiv: [1101.1628 \[hep-ex\]](#).
- 1379 [43] CMS Collaboration, *Search for Supersymmetry at the LHC in Events with*
1380 *Jets and Missing Transverse Energy, Phys. Rev. Lett.* **107** (2011) p. 221804,
1381 arXiv: [1109.2352 \[hep-ex\]](#).
- 1382 [44] CMS Collaboration, *Search for supersymmetry in hadronic final states using*
1383 *M_{T2} in pp collisions at $\sqrt{s} = 7 \text{ TeV}$, JHEP* **10** (2012) p. 018,
1384 arXiv: [1207.1798 \[hep-ex\]](#).
- 1385 [45] CMS Collaboration, *Searches for supersymmetry using the M_{T2} variable in*
1386 *hadronic events produced in pp collisions at 8 TeV, JHEP* **05** (2015) p. 078,
1387 arXiv: [1502.04358 \[hep-ex\]](#).
- 1388 [46] CMS Collaboration, *Search for new physics with the M_{T2} variable in all-jets*
1389 *final states produced in pp collisions at $\sqrt{s} = 13 \text{ TeV}$ (2016),*
1390 arXiv: [1603.04053 \[hep-ex\]](#).
- 1391 [47] ATLAS Collaboration, *Multi-channel search for squarks and gluinos in*
1392 *$\sqrt{s} = 7 \text{ TeV}$ pp collisions with the ATLAS detector at the LHC,*
1393 *Eur. Phys. J. C* **73** (2013) p. 2362, arXiv: [1212.6149 \[hep-ex\]](#).

- 1394 [48] Y. Grossman, “Introduction to the SM,” 2016, URL: <https://indico.fnal.gov/sessionDisplay.py?sessionId=3&confId=11505#20160811>.
- 1395
- 1396 [49] ()�.
- 1397 [50] P. W. Higgs, *Broken Symmetries and the Masses of Gauge Bosons*,
1398 *Phys. Rev. Lett.* **13** (1964) p. 508.
- 1399 [51] ATLAS Collaboration, *Observation of a new particle in the search for the*
1400 *Standard Model Higgs boson with the ATLAS detector at the LHC*,
1401 *Phys. Lett. B* **716** (2012) p. 1, arXiv: [1207.7214](https://arxiv.org/abs/1207.7214) [hep-ex].
- 1402 [52] CMS Collaboration, *Observation of a new boson at a mass of 125 GeV with*
1403 *the CMS experiment at the LHC*, *Phys. Lett. B* **716** (2012) p. 30,
1404 arXiv: [1207.7235](https://arxiv.org/abs/1207.7235) [hep-ex].
- 1405 [53] A. Chodos et al., *A New Extended Model of Hadrons*,
1406 *Phys. Rev. D* **9** (1974) p. 3471.
- 1407 [54] A. Chodos et al., *Baryon Structure in the Bag Theory*,
1408 *Phys. Rev. D* **10** (1974) p. 2599.
- 1409 [55] J. C. Collins, D. E. Soper, and G. F. Sterman,
1410 *Factorization of Hard Processes in QCD*,
1411 *Adv. Ser. Direct. High Energy Phys.* **5** (1989) p. 1,
1412 arXiv: [hep-ph/0409313](https://arxiv.org/abs/hep-ph/0409313) [hep-ph].
- 1413 [56] K. A. Olive et al., *Review of Particle Physics*,
1414 *Chin. Phys. C* **38** (2014) p. 090001.
- 1415 [57] N. Cabibbo, *Unitary Symmetry and Leptonic Decays*,
1416 *Phys. Rev. Lett.* **10** (1963) p. 531, [,648(1963)].
- 1417 [58] M. Kobayashi and T. Maskawa,
1418 *CP Violation in the Renormalizable Theory of Weak Interaction*,
1419 *Prog. Theor. Phys.* **49** (1973) p. 652.
- 1420 [59] W. F. L. Hollik, *Radiative Corrections in the Standard Model and their Role*
1421 *for Precision Tests of the Electroweak Theory*,
1422 *Fortsch. Phys.* **38** (1990) p. 165.
- 1423 [60] D. Yu. Bardin et al.,
1424 *ELECTROWEAK RADIATIVE CORRECTIONS TO DEEP INELASTIC*
1425 *SCATTERING AT HERA! CHARGED CURRENT SCATTERING*,
1426 *Z. Phys. C* **44** (1989) p. 149.

- 1427 [61] D. C. Kennedy et al., *Electroweak Cross-Sections and Asymmetries at the Z0*,
 1428 Nucl. Phys. **B321** (1989) p. 83.
- 1429 [62] A. Sirlin, *Radiative Corrections in the SU(2)-L x U(1) Theory: A Simple*
 1430 *Renormalization Framework*, Phys. Rev. **D22** (1980) p. 971.
- 1431 [63] S. Fanchiotti, B. A. Kniehl, and A. Sirlin,
 1432 *Incorporation of QCD effects in basic corrections of the electroweak theory*,
 1433 Phys. Rev. **D48** (1993) p. 307, arXiv: [hep-ph/9212285](https://arxiv.org/abs/hep-ph/9212285) [hep-ph].
- 1434 [64] C. Quigg, “Cosmic Neutrinos,” *Proceedings, 35th SLAC Summer Institute on*
 1435 *Particle Physics: Dark matter: From the cosmos to the Laboratory (SSI 2007):*
 1436 *Menlo Park, California, July 30- August 10, 2007*, 2008,
 1437 arXiv: [0802.0013](https://arxiv.org/abs/0802.0013) [hep-ph],
 1438 URL: http://lss.fnal.gov/cgi-bin/find_paper.pl?conf=07-417.
- 1439 [65] S. R. Coleman and J. Mandula, *All Possible Symmetries of the S Matrix*,
 1440 Phys. Rev. **159** (1967) p. 1251.
- 1441 [66] R. Haag, J. T. Lopuszanski, and M. Sohnius,
 1442 *All Possible Generators of Supersymmetries of the s Matrix*,
 1443 Nucl. Phys. **B88** (1975) p. 257.
- 1444 [67] A. Salam and J. A. Strathdee, *On Superfields and Fermi-Bose Symmetry*,
 1445 Phys. Rev. **D11** (1975) p. 1521.
- 1446 [68] S. Dimopoulos and H. Georgi, *Softly Broken Supersymmetry and SU(5)*,
 1447 Nucl. Phys. **B193** (1981) p. 150.
- 1448 [69] S. Dimopoulos, S. Raby, and F. Wilczek,
 1449 *Supersymmetry and the Scale of Unification*, Phys. Rev. **D24** (1981) p. 1681.
- 1450 [70] L. E. Ibanez and G. G. Ross,
 1451 *Low-Energy Predictions in Supersymmetric Grand Unified Theories*,
 1452 Phys. Lett. **B105** (1981) p. 439.
- 1453 [71] W. J. Marciano and G. Senjanovic,
 1454 *Predictions of Supersymmetric Grand Unified Theories*,
 1455 Phys. Rev. **D25** (1982) p. 3092.
- 1456 [72] L. Girardello and M. T. Grisaru, *Soft Breaking of Supersymmetry*,
 1457 Nucl. Phys. **B194** (1982) p. 65.

- 1458 [73] D. J. H. Chung et al.,
 1459 *The Soft supersymmetry breaking Lagrangian: Theory and applications*,
 1460 *Phys. Rept.* **407** (2005) p. 1, arXiv: [hep-ph/0312378 \[hep-ph\]](#).
- 1461 [74] J. Hisano et al., *Lepton flavor violation in the supersymmetric standard model*
 1462 *with seesaw induced neutrino masses*, *Phys. Lett.* **B357** (1995) p. 579,
 1463 arXiv: [hep-ph/9501407 \[hep-ph\]](#).
- 1464 [75] F. Gabbiani et al., *A Complete analysis of FCNC and CP constraints in*
 1465 *general SUSY extensions of the standard model*,
 1466 *Nucl. Phys.* **B477** (1996) p. 321, arXiv: [hep-ph/9604387 \[hep-ph\]](#).
- 1467 [76] F. Gabbiani and A. Masiero, *FCNC in Generalized Supersymmetric Theories*,
 1468 *Nucl. Phys.* **B322** (1989) p. 235.
- 1469 [77] J. S. Hagelin, S. Kelley, and T. Tanaka, *Supersymmetric flavor changing*
 1470 *neutral currents: Exact amplitudes and phenomenological analysis*,
 1471 *Nucl. Phys.* **B415** (1994) p. 293.
- 1472 [78] J. S. Hagelin, S. Kelley, and V. Ziegler, *Using gauge coupling unification and*
 1473 *proton decay to test minimal supersymmetric SU(5)*,
 1474 *Phys. Lett.* **B342** (1995) p. 145, arXiv: [hep-ph/9406366 \[hep-ph\]](#).
- 1475 [79] D. Choudhury et al.,
 1476 *Constraints on nonuniversal soft terms from flavor changing neutral currents*,
 1477 *Phys. Lett.* **B342** (1995) p. 180, arXiv: [hep-ph/9408275 \[hep-ph\]](#).
- 1478 [80] R. Barbieri and L. J. Hall, *Signals for supersymmetric unification*,
 1479 *Phys. Lett.* **B338** (1994) p. 212, arXiv: [hep-ph/9408406 \[hep-ph\]](#).
- 1480 [81] B. de Carlos, J. A. Casas, and J. M. Moreno,
 1481 *Constraints on supersymmetric theories from mu —> e gamma*,
 1482 *Phys. Rev.* **D53** (1996) p. 6398, arXiv: [hep-ph/9507377 \[hep-ph\]](#).
- 1483 [82] J. A. Casas and S. Dimopoulos,
 1484 *Stability bounds on flavor violating trilinear soft terms in the MSSM*,
 1485 *Phys. Lett.* **B387** (1996) p. 107, arXiv: [hep-ph/9606237 \[hep-ph\]](#).
- 1486 [83] C. Borschensky et al., *Squark and gluino production cross sections in pp*
 1487 *collisions at $\sqrt{s} = 13, 14, 33$ and 100 TeV*, *Eur. Phys. J.* **C74** (2014) p. 3174,
 1488 arXiv: [1407.5066 \[hep-ph\]](#).
- 1489 [84] M. Klasen, M. Pohl, and G. Sigl, *Indirect and direct search for dark matter*,
 1490 *Prog. Part. Nucl. Phys.* **85** (2015) p. 1, arXiv: [1507.03800 \[hep-ph\]](#).

- 1491 [85] L. Evans and P. Bryant, *LHC Machine*, JINST **3** (2008) S08001.
- 1492 [86] V. Shiltsev, “Accelerator Physics and Technology,” 2016,
 1493 URL: [https://indico.fnal.gov/sessionDisplay.py?sessionId=3&](https://indico.fnal.gov/sessionDisplay.py?sessionId=3&confId=11505#20160811)
 1494 [confId=11505#20160811](#).
- 1495 [87] *LEP design report*, Copies shelved as reports in LEP, PS and SPS libraries,
 1496 Geneva: CERN, 1984, URL: <https://cds.cern.ch/record/102083>.
- 1497 [88] ATLAS Collaboration,
 1498 *The ATLAS Experiment at the CERN Large Hadron Collider*,
 1499 JINST **3** (2008) S08003.
- 1500 [89] ATLAS Collaboration, *2015 start-up trigger menu and initial performance*
 1501 *assessment of the ATLAS trigger using Run-2 data*,
 1502 ATL-DAQ-PUB-2016-001, 2016,
 1503 URL: <https://cds.cern.ch/record/2136007/>.
- 1504 [90] ATLAS Collaboration,
 1505 *Electron reconstruction and identification efficiency measurements with the*
 1506 *ATLAS detector using the 2011 LHC proton–proton collision data*,
 1507 Eur. Phys. J. C **74** (2014) p. 2941, arXiv: [1404.2240 \[hep-ex\]](https://arxiv.org/abs/1404.2240).
- 1508 [91] ATLAS Collaboration, *Topological cell clustering in the ATLAS calorimeters*
 1509 *and its performance in LHC Run 1* (2016), arXiv: [1603.02934 \[hep-ex\]](https://arxiv.org/abs/1603.02934).
- 1510 [92] M. Aaboud et al., *Measurement of the photon identification efficiencies with*
 1511 *the ATLAS detector using LHC Run-1 data* (2016),
 1512 arXiv: [1606.01813 \[hep-ex\]](https://arxiv.org/abs/1606.01813).
- 1513 [93] ATLAS Collaboration, *Electron and photon energy calibration with the*
 1514 *ATLAS detector using LHC Run 1 data*, Eur. Phys. J. C **74** (2014) p. 3071,
 1515 arXiv: [1407.5063 \[hep-ex\]](https://arxiv.org/abs/1407.5063).
- 1516 [94] ATLAS Collaboration, *Muon reconstruction performance of the ATLAS*
 1517 *detector in proton–proton collision data at $\sqrt{s} = 13 \text{ TeV}$* (2016),
 1518 arXiv: [1603.05598 \[hep-ex\]](https://arxiv.org/abs/1603.05598).
- 1519 [95] S. D. Ellis and D. E. Soper,
 1520 *Successive combination jet algorithm for hadron collisions*,
 1521 Phys. Rev. D**48** (1993) p. 3160, arXiv: [hep-ph/9305266 \[hep-ph\]](https://arxiv.org/abs/hep-ph/9305266).
- 1522 [96] M. Cacciari and G. P. Salam, *Dispelling the N^3 myth for the k_t jet-finder*,
 1523 Phys. Lett. B**641** (2006) p. 57, arXiv: [hep-ph/0512210 \[hep-ph\]](https://arxiv.org/abs/hep-ph/0512210).

- 1524 [97] M. Cacciari, G. P. Salam, and G. Soyez,
1525 *The Anti- $k(t)$ jet clustering algorithm*, JHEP **04** (2008) p. 063,
1526 arXiv: [0802.1189 \[hep-ph\]](https://arxiv.org/abs/0802.1189).

1528 In this appendix, we provide a brief overview of the basic ingredients involved in
 1529 construction of the Standard Model Lagrangian : quantum field theory, symmetries,
 1530 and symmetry breaking.

1531 **Quantum Field Theory**

1532

1533 In this section, we provide a brief overview of the necessary concepts from
 1534 Quantum Field Theory (QFT).

cite Yuval's
lectures
and notes
somehow

1535 In modern physics, the laws of nature are described by the “action” S , with the
 1536 imposition of the principle of minimum action. The action is the integral over the cite
 1537 spacetime coordinates of the “Lagrangian density” \mathcal{L} , or Lagrangian for short. The
 1538 Lagrangian is a function of “fields”; general fields will be called $\phi(x^\mu)$, where the
 1539 indices μ run over the space-time coordinates. We can then write the action S as

$$S = \int d^4x \mathcal{L}[\phi_i(x^\mu), \partial_\mu \phi_i(x^\mu)] \quad (10.1)$$

1540 where we have an additional summation over i (of the different fields). Generally,
 1541 we impose the following constraints on the Lagrangian :

- 1542 1. Translational invariance - The Lagrangian is only a function of the fields ϕ and
 1543 their derivatives $\partial_\mu \phi$
- 1544 2. Locality - The Lagrangian is only a function of one point x_μ in spacetime.

1545 3. Reality condition - The Lagrangian is real to conserve probability.

1546 4. Lorentz invariance - The Lagrangian is invariant under the Poincarégroup of
1547 spacetime.

1548 5. Analyticity - The Lagrangian is an analytical function of the fields; this is to
1549 allow the use of perturbation theory.

1550 6. Invariance and Naturalness - The Lagrangian is invariant under some internal
1551 symmetry groups; in fact, the Lagrangian will have *all* terms allowed by the
1552 imposed symmetry groups.
maybe add 1552
in ref here

1553 7. Renormalizability - The Lagrangian will be renormalizable - in practice, this
1554 means there will not be terms with more than power 4 in the fields.

1555 The key item from the point of view of this thesis is that of “Invariance and
1556 Natural”. We impose a set of “symmetries” and then our Lagrangian is the most
1557 general which is allowed by those symmetries.

1558 Symmetries

1559 Symmetries can be seen as the fundamental guiding concept of modern physics.

cite? 1560 Symmetries are described by “groups”. To illustrate the importance of symmetries
1561 and their mathematical description, groups, we start here with two of the simplest
1562 and most useful examples : \mathbb{Z}_2 and $U(1)$.

1563 \mathbb{Z}_2 symmetry

1564 \mathbb{Z}_2 symmetry is the simplest example of a “discrete” symmetry. Consider the most
1565 general Lagrangian of a single real scalar field $\phi(x_\mu)$

$$\mathcal{L}_\phi = \frac{1}{2}\partial_\mu\phi\partial^\mu\phi - \frac{m^2}{2}\phi^2 - \frac{\mu}{2\sqrt{2}}\phi^3 - \lambda\phi^4 \quad (10.2)$$

Now we *impose* the symmetry

$$\mathcal{L}(\phi) = \mathcal{L}(-\phi) \quad (10.3)$$

1566 This has the effect of restricting the allowed terms of the Lagrangian. In particular,
 1567 we can see the term $\phi^3 \rightarrow -\phi^3$ under the symmetry transformation, and thus must
 1568 be disallowed by this symmetry. This means under the imposition of this particular
 1569 symmetry, our Lagrangian should be rewritten as

$$\mathcal{L}_\phi = \frac{1}{2}\partial_\mu\phi\partial^\mu\phi - \frac{m^2}{2}\phi^2 - \lambda\phi^4 \quad (10.4)$$

1570 The effect of this symmetry is that the total number of ϕ particles can only change
 1571 by even numbers, since the only interaction term $\lambda\phi^4$ is an even power of the field.
 1572 This symmetry is often imposed in supersymmetric theories, as we will see in Chapter
 1573 3.

1574 **$U(1)$ symmetry**

1575 $U(1)$ is the simplest example of a continuous (or *Lie*) group. Now consider a theory
 1576 with a single complex scalar field $\phi = \text{Re } \phi + i \text{Im } \phi$

$$\mathcal{L}_\phi = \delta_{i,j} \frac{1}{2}\partial_\mu\phi_i\partial^\mu\phi_j - \frac{m^2}{2}\phi_i\phi_j - \frac{\mu}{2\sqrt{2}}\phi_i\phi_j\phi_k\phi_l - \lambda\phi_i\phi_j\phi_k\phi_l \quad (10.5)$$

1577 where $i, j, k, l = \text{Re}, \text{Im}$. In this case, we impose the following $U(1)$ symmetry
 1578 : $\phi \rightarrow e^{i\theta}, \phi^* \rightarrow e^{-i\theta}$. We see immediately that this again disallows the third-order
 1579 terms, and we can write a theory of a complex scalar field with $U(1)$ symmetry as

$$\mathcal{L}_\phi = \partial_\mu\phi\partial^\mu\phi^* - \frac{m^2}{2}\phi\phi^* - \lambda(\phi\phi^*)^2 \quad (10.6)$$

1580 **Local symmetries**

1581 The two examples considered above are “global” symmetries in the sense that the
1582 symmetry transformation does not depend on the spacetime coordinate x_μ . We know
1583 to look at local symmetries; in this case, for example with a local $U(1)$ symmetry, the
1584 transformation has the form $\phi(x_\mu) \rightarrow e^{i\theta(x_\mu)}\phi(x_\mu)$. These symmetries are also known
1585 as “gauge” symmetries; all symmetries of the Standard Model are gauge symmetries.

There are wide-ranging consequences to the imposition of local symmetries. To begin, we note that the derivative terms of the Lagrangian 10.2 are *not* invariant under a local symmetry transformation

$$\partial_\mu \phi(x_\mu) \rightarrow \partial_\mu(e^{i\theta(x_\mu)}\phi(x_\mu)) = (1 + i\theta(x_\mu))e^{i\theta(x_\mu)}\phi(x_\mu) \quad (10.7)$$

GET THIS
RIGHT 1586

1587 This leads us to note that the kinetic terms of the Lagrangian are also not invariant
1588 under a gauge symmetry. This would lead to a model with no dynamics, which is
1589 clearly unsatisfactory.

1590 Let us take inspiration from the case of global symmetries. We need to define a
1591 so-called “covariant” derivative D^μ such that

$$D^\mu \phi \rightarrow e^{iq\theta(x^\mu)D^\mu}\phi \quad (10.8)$$

$$D^\mu \phi^* \rightarrow e^{-iq\theta(x^\mu)D^\mu}\phi^* \quad (10.9)$$

$$(10.10)$$

1592 Since ϕ and ϕ^* transforms with the opposite phase, this will lead the invariance
1593 of the Lagrangian under our local gauge transformation. This D^μ is of the following
1594 form

$$D^\mu = \partial_\mu - igqA^\mu \quad (10.11)$$

1595 where A^μ is a vector field we introduce with the transformation law

$$A^\mu \rightarrow A^\mu - \frac{1}{g} \partial_\mu \theta \quad (10.12)$$

1596 and g is the coupling constant associated to vector field. This vector field A^μ is
1597 also known as a “gauge” field.

1598 Since we need to add all allowed terms to the Lagrangian, we define

$$F^{\mu\nu} = A^\mu A^\nu - A^\nu A^\mu \quad (10.13)$$

1599 and then we must also add the kinetic term :

$$\mathcal{L}_{\text{gauge}} = -\frac{1}{4} F^{\mu\nu} F_{\mu\nu} \quad (10.14)$$

1600 The most general renormalizable Lagrangian with fermion and scalar fields can
1601 be written in the following form

$$\mathcal{L} = \mathcal{L}_{\text{kin}} + \mathcal{L}_\phi + \mathcal{L}_\psi + \mathcal{L}_{\text{Yukawa}} \quad (10.15)$$

1602 Symmetry breaking and the Higgs mechanism

1603 Here we view some examples of symmetry breaking. We investigate breaking of a
1604 global $U(1)$ symmetry and a local $U(1)$ symmetry. The SM will break the electroweak
1605 symmetry $SU(2)xU(1)$, and in Chapter 3 we will see how supersymmetry must also
1606 be broken.

1607 There are two ideas of symmetry breaking

- 1608 • Explicit symmetry breaking by a small parameter - in this case, we have a small
1609 parameter which breaks an “approximate” symmetry of our Lagrangian. An
1610 example would be the theory of the single scalar field 10.2, when $\mu \ll m^2$ and

1611 $\mu \ll \lambda$. In this case, we can often ignore the small term when considering
 1612 low-energy processes.

1613 • Spontaneous symmetry breaking (SSB) - spontaneous symmetry breaking
 1614 occurs when the Lagrangian is symmetric with respect to a given symmetry
 1615 transformation, but the ground state of the theory is *not* symmetric with respect
 1616 to that transformation. This can have some fascinating consequences, as we
 1617 will see in the following examples

1618 Symmetry breaking a

1619 **U(1) global symmetry breaking**

Consider the theory of a complex scalar field under the $U(1)$ symmetry, or the transformation

$$\phi \rightarrow e^{i\theta} \phi \quad (10.16)$$

The Lagrangian for this theory is

$$\mathcal{L} = \partial^\mu \phi^\dagger \partial_\mu \phi + \frac{\mu^2}{2} \phi^\dagger \phi + \frac{\lambda}{4} (\phi^\dagger \phi)^2 \quad (10.17)$$

Let us write this theory in terms of two scalar fields, h and ξ : $\phi = (h + i\xi)/\sqrt{2}$.

The Lagrangian can then be written as

$$\mathcal{L} = \partial^\mu h \partial_\mu h + \partial^\mu \xi d\mu \xi - \frac{\mu^2}{2} (h^2 + \xi^2) - \frac{\lambda}{4} (h^2 + \xi^2)^2 \quad (10.18)$$

First, note that the theory is only stable when $\lambda > 0$. To understand the effect of SSB, we now enforce that $\mu^2 < 0$, and define $v^2 = -\mu^2/\lambda$. We can then write the scalar potential of this theory as :

$$V(\phi) = \lambda(\phi^\dagger \phi - v^2/2)^2 \quad (10.19)$$

Minimizing this equation with respect to ϕ , we can see that the “vacuum expectation value” of the theory is

$$2 < \phi^\dagger \phi > = < h^2 + \xi^2 > = v^2 \quad (10.20)$$

1620 We now reach the “breaking” point of this procedure. In the (h, ξ) plane, the
 1621 minima form a circle of radius v . We are free to choose any of these minima to expand
 1622 our Lagrangian around; the physics is not affected by this choice. For convenience,
 1623 choose $\langle h \rangle = v, \langle \xi^2 \rangle = 0$.

Now, let us define $h' = h - v, \xi' = \xi$ with VEVs $\langle h' \rangle = 0, \langle \xi' \rangle = 0$. We can
 then write our spontaneously broken Lagrangian in the form

$$\mathcal{L} = \frac{1}{2}\partial_\mu h'\partial^\mu h' + \frac{1}{2}\partial_\mu \xi'\partial^\mu \xi' - \lambda v^2 h'^2 - \lambda v h'(h'^2 + \xi'^2) - \lambda(h'^2 + \xi'^2)^2 \quad (10.21)$$